Form and fate: The morphological landscape of zebrafish lateral line neuromast cells

Madeleine N. Hewitt

A dissertation

submitted in partial fulfillment of the

requirements for the degree of

Doctor of Philosophy

University of Washington

2023

Reading Committee:

David Raible, Chair

Celeste Berg

Cecilia Moens

Program Authorized to Offer Degree:

Molecular and Cellular Biology

University of Washington

Abstract

Form and fate: The morphological landscape of zebrafish lateral line neuromast cells

Madeleine N. Hewitt

Chair of the Supervisory Committee:

Professor David Raible

Department of Otolaryngology – Head and Neck Surgery

The shape of a cell both influences and is influenced by its fate. However, quantitative studies of cell shape in living, developing organisms have been limited in dimension and scope. To establish the utility and feasibility of cell shape analysis *in vivo,* cell shape analysis could first be applied to well-studied model systems that are amenable to high resolution live imaging. One such model is the lateral line, a sensory system in aquatic vertebrates that detects changes in water flow. Organs of the lateral line, called neuromasts, are composed of rosette-like clusters of mechanosensory hair cells surrounded by nonsensory support cells. Lateral line neuromasts have been studied by microscopic imaging for over a century, owing to their accessible location (just beneath the surface of the skin). Much is also known about the molecular regulation and cellular composition of zebrafish lateral line neuromasts. However, prior to my work, the morphologies of neuromast cells and nuclei had yet to be thoroughly described. In this work, I first introduce the utility of shape analysis in biology and review what was previously known

about hair cell regeneration in nonmammalian vertebrates. I then describe a new study in which I performed data-driven, three-dimensional shape analysis of zebrafish lateral line neuromast cells using spherical harmonics, principal components analysis, and unsupervised clustering. I find that hair cells have a discretely distinct shape from support cells and successfully train a classifier to identify hair cells from shape features. I also find that support cell subpopulations have identifiable shape phenotypes, although the distinctions between support cell subpopulations were more nuanced compared to the difference between hair cells and support cells as a whole. To show the effects of loss of a cell type on shape, I characterized cell shape *atoh1a* mutants, which lack hair cells; I find that *atoh1a* mutants lack the shape phenotype associated with hair cells but do not appear to exhibit a mutant-specific shape. I also describe the coding pipeline I developed to process and analyze my dataset. Finally, I reflect on the conclusions and potential future applications of my work, which lays a foundation for further studies of the relationships between cell shape, cell fate, and organ shape in sensory epithelia and beyond.

TABLE OF CONTENTS

LIST OF FIGURES

LIST OF TABLES

ACKNOWLEDGMENTS

Well, looks like we finally made it here. So many people have supported me over the years, it's hard to know where to begin. From the bottom of my heart, I thank everyone who has been a part of my arduous, sometimes painful, yet ultimately rewarding journey.

First, I'd like to thank several key people who motivated me to pursue science in my high school and undergraduate years. In particular, I was fortunate to know a lot of fantastic women educators and scientists growing up, including Drs. Mary Jane Patterson and Kathleen Matthews. I am grateful to them for their support and guidance that helped to set me along this path.

I would also like to thank my thesis advisor, Dr. David Raible. Dave is not only an excellent scientist, but also a great mentor who shows care and empathy towards his trainees. When I first proposed the cell shape analysis project to Dave, he was (rightfully) skeptical. However, once I convinced him, he became one of the project's biggest supporters. Dave's enthusiasm and optimism for the project helped to push me through some of its tougher challenges, which I am grateful for. Dave also gave constructive feedback that sharpened my presentation and writing skills, which helped me to win an F31 and ace my first job interview. It's hard to understate the importance of being able to communicate one's science to a variety of audiences, and I'm truly grateful I was able to learn this crucial skill as a member of Dave's lab.

I would be remiss not to acknowledge the members of Dave's lab for making it such a great environment to work in during my PhD. Lots of people have come and gone in the years I've been a part of it, but the atmosphere has always been supportive and fun. I would like to thank Marielle Beaulieu for being a fun fellow grad student to hang out (and occasionally commiserate) with. I would also like to thank Andrea McQuate, who joined the lab around the same time I did, for her advice and support. In addition, I'm grateful to Iván Cruz for organizing lab social events and generally being a chill, fun person to be around. I'd also like to thank my

bioimage club buddies, Francisco Barros-Becker and Tricia Wu, for being a great source of feedback and ideas even when I started getting really far into the weeds (whiteboard drawings of 3D rotations, anyone?).

Thank you to the members of my thesis committee, Drs. Celeste Berg, Clemens Cabernard, David Kimelman, Cecilia Moens, and Jeff Rasmussen. I am truly grateful to have had a wonderful group of people on my committee that supported both my scientific growth and general wellbeing. Pursuing a PhD during a global pandemic was not easy, and I feel incredibly fortunate to have a committee that recognized this unique challenge and provided words of encouragement at crucial times. Thanks to them, I was able to start – and eventually complete – this "blue sky" thesis project.

Sometimes, getting perspective outside of our usual scientific spheres can shape our projects in new and exciting ways. That was the case for me when Dr. Julie Theriot and her lab moved to the UW. Dr. Theriot's lab welcomed me into their weekly lab meeting and provided advice that helped me to get the cell shape project off the ground. Since then, her lab became something of a second scientific home for me during my PhD. I admire the intensely curious, creative, and careful way in which the Theriot lab approaches problems. Learning from them helped me to make my project the best it could be.

Learning to program in Python was one of the greatest achievements of my PhD. I would like to thank Dr. Bing Brunton and Eliza Barkan for teaching the introductory data science class I took, which set a solid foundation for me to continue learning on my own. I would also like to thank the Allen Institute for Cell Science for making their code public, which was a major part of my analysis pipeline. In addition, I am grateful to the bioimage analysis community and open source contributors for making an abundance of awesome, freely available tools that accelerate scientific progress – my thesis would not have been possible without their work.

I have been fortunate to have many amazing friends during graduate school. Without a doubt, I would not have been able to finish my PhD without their emotional support. With friends, I've enjoyed many a party, meal, coffee, game night, bar hangout, heart-to-heart, venting session, and more; these are (and will remain, I'm certain) some of my fondest memories of my time in graduate school. Though it wasn't always easy and required some creativity, I'm grateful I was able to stay connected to so many great people despite the isolation brought about by the pandemic. I want to give special thanks to Ami Yamamoto, Vanessa Montoya, Brad Krajina, Jeet Patel, and Rachel Lim for being there for me even during my most fragile, insecure moments. I'd also like to thank my various Dungeons & Dragons groups for being a much needed creative outlet and source of fun throughout my PhD. Additionally, I'd like to thank the Friendsgiving crew, especially Florie D'Orazi, Brian Turner, Steph Seeman, and Sweta Agrawal, who've given me helpful advice and generally been a great group of people to hang out with.

I would also like to thank my family for their love and support during my PhD. During difficult times, it helped to know they'd always be in my corner. In particular, I'd like to thank my parents, Marie Davern, Jason Hewitt, and Anne Hewitt for always supporting my personal and professional endeavors. I can't thank them enough for providing the solid foundation I needed in life to be able to accomplish something as difficult as getting my PhD. I'd also like to thank my siblings for always making my home in Texas a fun place to come back to – I hope I can also support them in their future plans as well.

Finally, I'd like to give heartfelt thanks to my partner, ET Thomas. Having a partner who understands the ups and downs of graduate school firsthand has been so, so helpful. ET has been there for me during both my brightest and darkest moments. With their ever-present thoughtful, encouraging, and goofy nature, they have looked out for me in so many ways, both small and large. Their support has been crucial, especially during this final push to finish my

PhD. Thank you so much for all that you've done for me – and it has been a lot, whether you realize it or not.

Madeleine N. Hewitt

Seattle, 2023

CHAPTER 1: INTRODUCTION

Hair cells are the mechanosensory receptors in the inner ear responsible for our sensation of hearing and balance. They are surrounded by non-sensory glia-like cells known as support cells. Hair cells are susceptible to damage and death from a variety of environmental insults, including exposure to noise and ototoxic drugs. Unfortunately, in adult mammals, hair cell death is largely irreversible and can cause loss of hearing and vestibular function. Hearing loss is a common issue that affects over one-fifth of Americans aged 12 years or older (Goman and Lin 2016). Since loss of hearing and vestibular function negatively impacts quality of life for many people, procedures to prevent or restore loss of hair cells are of great interest to clinicians and researchers.

In contrast to mammals, nonmammalian vertebrates such as birds, amphibians, and fishes can robustly regenerate hair cells throughout life, restoring their sensory function. Hair cells in nonmammalian vertebrates are in many ways analogous to their mammalian counterparts in their development, function, and molecular regulation. In addition, hair cells in these organisms are often more accessible to study than those of adult mammals, enabling experimental manipulations and imaging studies that would otherwise be difficult.

Particularly accessible are the hair cells and support cells of the lateral line, a sensory system in fishes and other aquatic vertebrates that detects changes in water flow. Organs of the lateral line, known as neuromasts, are located beneath the skin in stereotyped locations (Figure 1.1A). In larval zebrafish, the lateral line includes the posterior lateral line (pLL) located on the trunk and the anterior lateral line (aLL) located on the head. During embryonic development, the pLL forms from a migratory collective of cells known as a primordium, which travels along the midline of the trunk and deposits neuromasts in its wake (Metcalfe 1985). Meanwhile, the aLL forms from a combination of migratory primordia and other mechanisms, such as budding

(Iwasaki et al. 2020). The lateral line continues to expand postembryonically (Ledent 2002; Nuñez et al. 2009).

The organization of cells in the neuromast resembles that of cloves in a bulb of garlic. Each neuromast is composed of a rosette-like cluster of flask-shaped hair cells surrounded by support cells (Figure 1.1B). Some support cells lie beneath hair cells; these centrally-located support cells have tall and thin apical projections that interdigitate between hair cells. Moving from the center of the neuromast to the periphery, one encounters several support cells with concave shapes, until one reaches the most peripheral support cell population (also known as mantle cells) which form a ring around the outside of the neuromast. The neuromast is thus organized radially and composed of cells with different shapes.

Studies of the lateral line and nonmammalian inner ear organs have provided – and continue to provide – a wealth of information about hair cell death, development, and regeneration (reviewed in Chapter 2). For example, these studies have revealed that some support cells act as hair cell progenitors in nonmammalian sensory epithelia. These studies may lead to the development of treatments to prevent and treat loss of hearing and vestibular function in humans. By studying the mechanisms of hair cell regeneration in nonmammals and elucidating what makes nonmammals different from their mammalian counterparts, it may one day be possible to induce hair cell regeneration in adult mammals.

To attain this goal, it is necessary to understand the cells that take part in regeneration and how they are regulated. At the time of writing, much of the field has focused on characterizing cells through the lens of gene expression. With the advent of technologies such as single cell RNA-sequencing (scRNA-seq), methods to characterize and classify cells based on transcriptional signatures have become increasingly sophisticated and commonplace. Several scRNA-seq studies of sensory epithelia have been performed (Lush et al. 2019; Shi et al. 2023),

providing the field with an abundance of information about the molecular characteristics of hair cells and support cells.

Although gene expression has garnered much recent attention, there is also a long history in biology of gaining insights by analyzing the shapes (morphologies) of individual cells and organs. In 1917, D'Arcy Thompson published his work *On Growth and Form,* which posited that biological forms emerge from the actions of physical forces (Thompson 1917). Thompson also demonstrated how differences between biological shapes could be modeled as geometric transformations. His work laid the foundation for future applications of mathematical and physical principles to biology, including morphometrics.

Since then, morphometric analyses have been invoked to understand how biological shapes change over developmental and evolutionary time in numerous contexts. Morphological comparisons of anatomical structures across species can provide insight into evolutionary relationships and selective pressures. For example, analysis of beak shape has revealed factors driving and constraining beak shape diversity in birds (Campàs et al. 2010; Fritz et al. 2014; Olsen 2017) and uncovered genes that regulate beak morphology (Abzhanov et al. 2004; Mallarino et al. 2012). Studies have also applied 3D shape analysis over time to understand principles of tissue and organ morphogenesis in the chick forebrain (Morishita et al. 2017) and mouse limb (Dalmasso et al. 2022). Morphometric analysis is therefore a powerful method to quantify the evolution of different forms at time scales both large and small. Additionally, the findings of these studies can be combined with genetic perturbations to elucidate the developmental mechanisms underlying differences in shape.

In addition to analyzing anatomical structures and whole organs, it is also possible to quantify the shapes of individual cells. The shape of a cell emerges from a myriad of internal and external cues, including biochemical signaling and mechanical forces (Chan et al. 2017). On this basis, cell shape has been used as a readout for cell state in a variety of contexts. Most studies of

cell shape have used cells in culture, which are easier to image and manipulate physically. A common technique to study cell shape in culture is to use micropatterned substrates or adhesive "islands" of predetermined shapes and sizes. Cells spread to conform to the shape of these islands, allowing researchers to test the effects of different shapes on cell behavior. These studies have shown that cell shape influences cell fate and behavior, including the propensity of cells to divide or die (Chen et al. 1997), as well as differentiate (Watt et al. 1988; Kilian et al. 2010). Studies of cell shape in culture have also elucidated the molecular and physical underpinnings of cell motility and migration (Keren et al. 2008; Barnhart et al. 2011). Notably, the cell migration field has employed sophisticated 2D shape representations capable of capturing information that may be missed when using geometric features (Pincus and Theriot 2007).

It is also possible (though more challenging) to quantify cell shape in intact tissues and organs. This approach can shed light on the relationships between individual cell shapes and larger scale processes at the tissue or organ level. For example, a single cell morphometrics study revealed the typical cell shape phenotypes and trajectories during amphioxus notochord development (Andrews et al. 2021). Another study morphologically profiled human cancer xenografts in zebrafish and found that cancer cell shape varied with cell type, microenvironment, and position within a cell cluster (Segal et al. 2022). Of particular relevance to my own thesis work is the study of Hartmann et al. (2020) which applied a morphometrics-based approach to quantify the shapes of cells in the zebrafish posterior lateral line primordium. Analyzing the shapes of single cells within their native cellular communities is important because mechanical feedback and cell shape change regulate cell fate and morphogenesis during many developmental processes (Chan et al. 2017). However, the complexity of 3D cell shapes and tissue architecture present additional challenges for *in vivo* cell shape analysis, and many questions remain about the mechanisms underlying cell shape-fate relationships.

With the advent of high resolution light microscopy techniques, better 3D segmentation techniques (enabled by machine learning), and recent applications of high-dimensional 3D shape representations to cell shape, I saw an opportunity to apply these methods to understand the relationship between cell shape and fate using the zebrafish lateral line as a model. In many ways, the zebrafish lateral line is an ideal candidate to test the feasibility of cell shape analysis in a living, developing animal. First, zebrafish are genetically tractable organisms with a fully sequenced genome and many genetic reagents available, including mutants and transgenic lines (Bradford et al. 2022). Second, the transparency of larval zebrafish combined with the superficial location and small size of neuromasts enables high resolution light microscopy studies of entire neuromast organs in living, intact animals. Third, neuromasts are known to have cell subpopulations with distinct spatial locations, gene expression patterns, and behaviors during regeneration (Lush et al. 2019; Thomas and Raible 2019). Each of these cell subpopulations represents a cell identity whose shape features can be characterized. Should my endeavor to analyze zebrafish neuromast cell shape succeed, I envision that similar methods could be applied to many other contexts, including sensory epithelia in other organisms. Such studies could add another lens through which to quantitatively characterize and compare cell populations within and between species, potentially helping to unravel the mystery of how regeneration is regulated and why it occurs in some species but not others.

In this work, I performed unbiased, data-driven analysis of 3D cell and nuclear shape in zebrafish neuromasts to elucidate connections between neuromast cell shape and identity. In Chapter 2, I review what is known about nonmammalian models of hair cell regeneration. In Chapter 3, I present the results of my work using spherical harmonics and principal components analysis (PCA) to characterize and classify the shapes of neuromast cells. In Chapter 4, I summarize the code I wrote to perform image segmentation and data analysis. In Chapter 5, I discuss the results and future directions of my work.

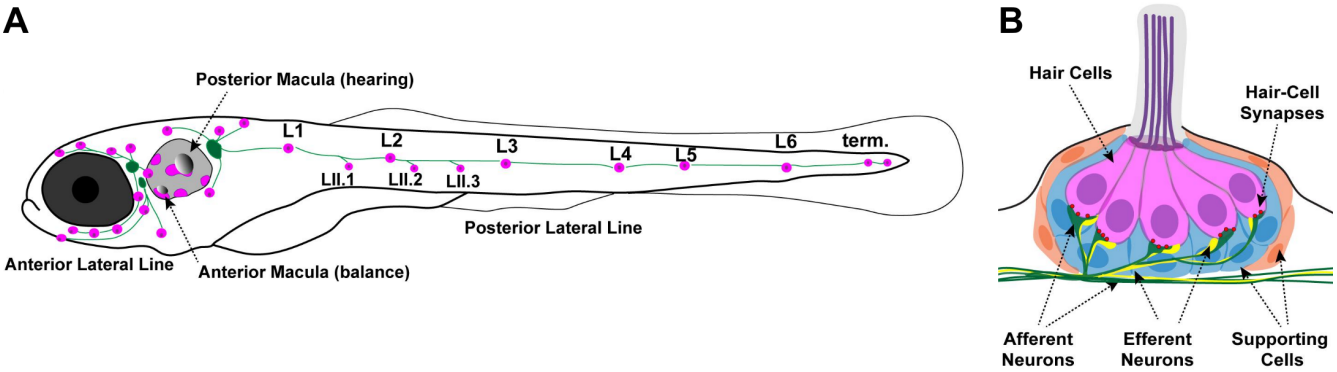

Figure 1.1: Locations and cellular structure of zebrafish lateral line neuromasts
Adapted from Figure 1 in Kindt and Sheets 2018 licensed under Creative Commons (CC BY 4.0).

(A) Schematic of the lateral line on a larval zebrafish. Locations of hair cells in lateral line neuromasts and the inner ear are labeled in magenta. The locations of the lateral line ganglia that provide afferent innervation to the anterior and posterior lateral line neuromasts are shown in green.

(B) Schematic of a neuromast viewed in cross-section. Hair cells (magenta) form a rosette-like structure in the center of the neuromast. Support cells (blue) lie underneath and adjacent to hair cells, surrounding them on all sides. Peripheral support cells (orange) are located in a ring around the outside of the neuromast. Hair cells are innervated by afferent (yellow) and efferent (green) neurons.

CHAPTER 2: NONMAMMALIAN HAIR CELL REGENERATION: CELLULAR MECHANISMS OF MORPHOLOGICAL AND FUNCTIONAL RECOVERY

The contents of this chapter have been published in the following book chapter:

Hewitt MN, Raible DW, Stone JS (2023) Nonmammalian Hair Cell Regeneration: Cellular Mechanisms of Morphological and Functional Recovery. In: Warchol ME, Stone JS, Coffin AB, et al. (eds) Hair Cell Regeneration. Springer International Publishing, Cham, pp 11–40

The following authors contributed to the contents of this chapter:

Madeleine N. Hewitt: Writing – original draft, writing – review & editing, visualization

David W. Raible: Writing – original draft, writing – review & editing

Jennifer S. Stone: Writing – original draft, writing – review & editing, visualization

Reproduced with permission from Springer Nature.

2.0 Abstract

This chapter provides an overview of hair cell regeneration in nonmammalian vertebrates. First, we review the early foundational research on hair cell replacement. Then, we discuss research in the past 15 years that underlies our current understanding of the mechanistic basis of hair cell regeneration, including the identity, properties, and epithelial locations of supporting cells, the progenitors to new hair cells. We also describe some of the new approaches used to study hair cell regeneration, and we discuss molecules that have been found to either

block or drive supporting cells to generate new hair cells after damage. This chapter focuses on chickens and zebrafish, which are the most commonly used animal models for this type of research.

2.1 Introduction

Studies conducted in the 1980s revealed that nonmammalian vertebrates have a remarkable ability to regenerate the sensory hair cells of the inner ear. Subsequent work has unveiled some of the cellular and molecular mechanisms that underlie this process and lead to restoration of hearing and balance function after hair cell injury. These studies advanced our fundamental understanding of how regeneration can occur in a highly specialized tissue. They also provided important clues as to why hair cell regeneration fails to occur in the auditory organ of mammals and why it is highly limited in the mammalian vestibular organs. This chapter reviews advances in our understanding of hair cell regeneration in nonmammalian vertebrates. The focus is on studies published since 2008, when the last version of the Springer Handbook of Auditory Research (SHAR) books on regeneration was released (Oesterle and Stone 2008). Because most of these studies in the past 14 years have examined chickens (Gallus gallus) and zebrafish (Danio rerio), our chapter focuses on those organisms. However, much of this work builds upon studies of postembryonic hair cell production in other nonmammals, such as sharks and goldfish (Corwin 1981; Presson et al. 1996). To learn about studies on nonmammalian hair cell regeneration prior to 2008, we recommend the following reviews: (Bermingham-McDonogh and Rubel 2003; Stone and Cotanche 2007; Breuskin et al. 2008; Ma and Raible 2009; Brignull et al. 2009; Cotanche and Kaiser 2010; Warchol 2011; Rubel et al. 2013; Ryals et al. 2013; Kelley and Stone 2017). Mammalian regeneration is discussed in Forge and Taylor, Chap. 4, and McGovern and Groves, Chap. 5.

2.2 Nonmammalian Hair Cell Regeneration: An Overview

In the late 1980s, several key studies sparked the exploration of hair cell regeneration as a way to restore function following hair cell injury and death. Initial papers presented morphological evidence that hair cells are replaced after damage to the chicken basilar papilla (BP; the avian hearing organ and analogue of the mammalian cochlea). These studies were conducted with early post-hatch chicks, in which the morphology and function of the auditory organ is largely mature (e.g., Tilney et al. 1992; Jones et al. 2006b). Cruz et al. (1987) used the aminoglycoside ototoxin gentamicin to induce hair cell death in the BP of hatchling chicks. Although a hair cell lesion was evident several days after gentamicin treatment, the authors noted an unexpected recovery of hair cell numbers after 3–4 weeks.

Another study used noise injury to induce hair cell lesions in the chick BP (Cotanche 1987). Imaging with scanning electron microscopy demonstrated the emergence over time of tiny bundles of stereocilia – the hearing organelle in hair cells – that resembled those of embryonic hair cells. This finding further suggested that some hair cells can be replaced after damage (Cotanche 1987).

Next, two studies (Corwin and Cotanche 1988; Ryals and Rubel 1988) published definitive evidence that these hair cells were regenerated and were the result of renewed cell proliferation. These studies focused on regeneration after noise trauma in both young chicks and senescent quail (*Coturnix coturnix japonica*). Radioactive (tritiated) thymidine, which becomes incorporated into newly replicated DNA, was administered to birds for several days after noise damage. Detection of this marker in the nuclei of replacement hair cells revealed that they had been regenerated by cell division and did not simply recover from damage or migrate from nearby uninjured areas. Importantly, the study of Ryals and Rubel also demonstrated that even old birds could replace hair cells after damage.

Subsequent studies sought to identify hair cell progenitors, which are the cell type that divides and generates new hair cells after hair cell damage in birds (reviewed in Stone and Cotanche 2007). Markers such as bromodeoxyuridine [BrdU], tritiated thymidine, and DNA-binding agents were delivered into birds after hair cell damage, and organs were examined shortly thereafter to catch cells as they underwent DNA synthesis and mitosis. These studies demonstrated that, within 24 hours after damage, supporting cells reentered the cell cycle and divided, and daughter cells became hair cells, demonstrating that supporting cells are the hair cell progenitors. These studies showed that new supporting cells were also formed after hair cell loss, indicating that hair cell progenitors are replenished during regeneration.

Following the discovery of hair cell regeneration in birds, researchers turned to other animals to examine the capacities for hair cell replacement in maturity. They determined that, following hair cell damage induced by laser-mediated ablation or ototoxic drugs, hair cells are also regenerated in amphibians (Balak et al. 1990; Baird et al. 1993), fishes (Song et al. 1995), and reptiles (Avallone et al. 2003). Studies with thymidine analogs or visual monitoring of live sensory epithelia showed that, like birds, supporting cells in these animals divide and form new hair cells shortly after hair cells degenerate and/or are lost from the sensory epithelia (e.g., Jones and Corwin 1993; Baird et al. 1996; Lanford et al. 1996).

Later studies broadened our understanding of nonmammalian hair cell regeneration by showing that supporting cells can form new hair cells using mechanisms other than mitotic division. This conclusion was based on the findings that (1) hair cells were replaced after damage when supporting cell division was blocked by drugs (AraC or aphidicolin) and (2) some regenerated hair cells lacked a cell division marker even when it was provided for long periods of time after damage. These studies were conducted in frog saccules (Baird et al. 2000) and chick BPs (Adler and Raphael 1996; Roberson et al. 2004; Shang et al. 2010). Thus, while supporting cells can generate new hair cells by undergoing cell division, they can also undergo *direct*

transdifferentiation, in which a highly specialized cell phenotypically converts into another cell without an intervening mitosis (Figure 2.1). This process had been documented in invertebrates but was considered to be quite unusual in vertebrates (reviewed in Morest and Cotanche 2004).

Some of the earliest work on postembyronic hair cell production in fish was conducted in sharks and goldfish (e.g., Corwin 1981; Presson et al. 1996). Later, many researchers adopted the zebrafish larval model, in large part for its experimental advantages over other species, such as small body size and widespread use for genetic studies. Research on hair cell regeneration in the zebrafish lateral line began with the demonstration that hair cells that are eliminated by exposure to ototoxic compounds are completely replaced after several days of recovery (Williams and Holder 2000; Harris et al. 2003). Regenerating hair cells are also properly reinnervated by directionally sensitive neurons (Nagiel et al. 2008; Faucherre et al. 2009). The lateral line system grows in complexity as the animal matures, adding new neuromasts from budding of existing sensory organs and from de novo generation from latent precursors (Nuñez et al. 2009; Iwasaki et al. 2020). Like in amphibians, lateral line neuromasts regenerate after tail amputation in zebrafish (Dufourcq et al. 2006). Postembryonic hair cell addition has also been observed in the inner ear of amphibians (Lewis and Li 1973) and aquatic vertebrates (Corwin 1981; Popper and Hoxter 1984). It is therefore perhaps not surprising that zebrafish neuromasts maintain the ability to produce new hair cells throughout life (Cruz et al. 2015; Pinto-Teixeira et al. 2015).

In contrast to birds and amphibians, direct transdifferentiation does not appear to be a major mechanism of hair cell regeneration in the fish lateral line. One study (Hernández et al. 2007) reported BrdU-negative hair cells during regeneration, which would suggest that some hair cells were not produced via cell division. However, other studies found that most hair cells produced during regeneration harbored a marker of DNA synthesis and therefore arose from cell division (Ma et al. 2008; Wibowo et al. 2011). In addition, treatment with the cell cycle

inhibitors aphidicolin, flubendazole, or nocodazole blocked hair cell regeneration in the zebrafish lateral line (Wibowo et al. 2011; Mackenzie and Raible 2012). Time-lapse studies of regenerating neuromasts have also indicated that new hair cells arise from symmetrically dividing precursors (Wibowo et al. 2011; Romero-Carvajal et al. 2015). While it is possible that direct transdifferentiation sometimes occurs in lateral line neuromasts of fish, supporting cell mitosis appears to be the primary mode of hair cell regeneration.

Compared to the lateral line, fewer studies have examined hair cell regeneration in the zebrafish inner ear. Zebrafish inner ear hair cells can be damaged and killed by exposure to noise trauma (Schuck and Smith 2009; Breitzler et al. 2020). Following noise-induced hair cell loss, hair cell numbers visibly recover within 7 days, and functional recovery occurs within 2 weeks (Breitzler et al. 2020). Hair cell regeneration in the fish inner ear is therefore rapid and robust. Hair cell regeneration in the fish inner ear is therefore rapid and robust. However, it remains unclear whether hair cells in the fish inner ear are regenerated through direct transdifferentiation, proliferation, or both. Mature supporting cells in the inner ears of the goldfish *Carrassius auratus* maintain the ability to enter the cell cycle postembroynically, which suggests that they may be able to act as mitotic precursors for hair cells during regeneration (Presson et al. 1996). One study suggested that direct transdifferentiation may contribute to hair cell regeneration in the larval zebrafish inner ear (Millimaki et al. 2010). However, hair cell regeneration was assayed at a stage when developmental hair cell addition was still occurring. When hair cells are damaged by noise stimulation in adult zebrafish, regeneration is accompanied by cell proliferation (Schuck and Smith 2009). Supporting cell division was also observed when hair cells were laser ablated in the zebrafish lateral crista (Rubbini et al. 2015). Whether this increased proliferation functions to produce regenerated hair cells or replenish the supporting cell population is not clear.

The full process of hair cell regeneration in birds, defined as the creation and maturation of new hair cells, reinnervation, and functional recovery, takes about1 month in the auditory organ and more than 6 months in vestibular organs (reviewed in Bermingham-McDonogh and Rubel 2003; Oesterle and Stone 2008; Rubel et al. 2013). A major limitation on the speed of vestibular regeneration is the maturation of afferent innervation and formation of calyx afferents that envelope type I hair cells, which can require about 6 months (Haque et al. 2009). In zebrafish neuromasts, hair cell regeneration is more rapid and is completed within days rather than months. Within 72 h of nearly complete hair cell death, larval zebrafish neuromasts can regenerate a full complement of hair cells with mature features (Harris et al. 2003; Ma et al. 2008). Ribbon synapse maturation and reinnervation likewise occurs within 72 h post-injury (Faucherre et al. 2009; Suli et al. 2016). In older larvae, onset of regeneration is likewise rapid, but complete functional recovery requires at least 5 days (Hardy et al. 2021).

Studies on songbirds in the 1990s demonstrated that hair cell regeneration restores sensory function, bringing hearing sensitivity back to near-normal levels (e.g., Marean et al. 1993; Dooling et al. 1997), enabling perception of specific bird song (Woolley et al. 2001; Woolley and Rubel 2002; Ryals et al. 2013), and restoring the ability to sense head motions (Carey et al. 1996; Goode et al. 1999; Matsui et al. 2003; Dickman and Lim 2004). Similarly, studies demonstrate that regeneration of hair cells in fish lateral line also restores behaviors related to its functions, including escape responses, rheotaxis, and schooling (McHenry et al. 2009; Suli et al. 2012; Mekdara et al. 2018).

In birds, amphibia, and fishes, hair cells in vestibular, auditory, and lateral line sensory organs undergo turnover; that is, hair cells have a finite lifespan, at which point they die and are replaced at a relatively low rate (reviewed in Brignull et al. 2009; see Coffin et al. 2012; Cruz et al. 2015). This process is distinct but related to hair cell regeneration, which occurs after hair cells are damaged by an external stimulus (ototoxins, noise, or laser ablation). It is also distinct

from the peripherally contained addition of hair cells in fish and amphibian vestibular organs, which grow in size throughout life (e.g., Corwin 1981, 1985). Importantly, no new hair cells appear to be added to auditory organs in mature birds (Jørgensen and Mathiesen 1988; Oesterle and Rubel 1993).

2.3 Supporting Cell Populations and Their Functions During Regeneration

As discussed in Sect. 2.2, supporting cells serve as progenitors for replacement hair cells. Supporting cells reside alongside hair cells. They serve multiple functions, including maintaining the three-dimensional structure and the ionic balance of the sensory epithelium, generating overlying extracellular matrix materials (tectorial membrane, otoconial membrane, and cupula), and wrapping afferent and efferent neurites of the sensory nerves (reviewed in Wan et al. 2013). The finding that supporting cells are the source of new hair cells after damage in nonmammalian vertebrates introduced a new function for them and raised several questions: Where are the hair cell progenitors located, how are they regulated, and how are they maintained? Are all supporting cells in a given sensory epithelium functionally identical, or do distinct populations exist? In the past 10 years, a considerable amount of work addressing these questions has been conducted in the lateral line of zebrafish and in the auditory and vestibular organs of the chick inner ear.

At first glance, supporting cells in nonmammalian lateral line and inner ear organs do not seem to be as specialized or diverse as their counterparts in the mammalian cochlea. For instance, although supporting cells in chick inner ear organs vary in shape depending on their locations in the epithelium, differences are subtle compared to the mammalian cochlea. Likewise, early studies of neuromasts only identified the most peripheral cells (also known as mantle cells) as representing a distinct population of supporting cells; the rest were simply grouped together as “internal” supporting cells (Jones and Corwin 1993).New technologies have

enabled more detailed interrogation of the diversity of cell types and lineage relationships in sensory epithelia, and through this work, it has become increasingly apparent that supporting cells in nonmammals are more diverse in function and behavior than previously recognized. This part of our chapter will review insights on supporting cell identities, locations, and functions in zebrafish neuromasts (Sects. 2.3.1 and 2.3.2) and chick inner ear epithelia (Sect. 2.3.3).

2.3.1 Identities and Locations of Hair Cell Progenitors in Fish

As discussed in Sect. 2.2, hair cell regeneration in lateral line neuromasts occurs primarily via proliferating precursors. A study using markers of DNA synthesis and mitosis following neomycin-induced hair cell death found that proliferation of internal supporting cells peaked around 15–18 h posttreatment (Ma et al. 2008). A later study used transgenic lines that labeled hair cells and supporting cells and identified hair cell progenitors located near the dorsal-ventral (DV) compartments of anteroposteriorly polarized neuromasts (Wibowo et al. 2011; Figure 2.2). These hair cell progenitors expressed high levels of the hair cell fate specification gene *atoh1a* (described in Sect. 2.5.1) and always divided just once, giving rise to two hair cells. These findings implied that DV-localized supporting cells are distinct from other internal supporting cells and have specialized functions during regeneration.

The finding that new hair cells arise from symmetrically dividing progenitor cells rather than an asymmetrically dividing stem cell population raised the question of whether hair cell progenitors would eventually be depleted. However, mature neuromasts retain the capacity to regenerate hair cells after repeated rounds of hair cell death and regeneration (Cruz et al. 2015; Pinto-Teixeira et al. 2015). Time-lapse imaging of regenerating neuromasts has shown that supporting cells can also divide symmetrically to produce more supporting cells (Romero-Carvajal et al. 2015). These supporting cell-producing divisions also occurred in DV

compartments of the neuromast but were less centrally located than hair cell-producing divisions. Moreover, supporting cells produced by proliferation during a first round of hair cell regeneration can divide to form new hair cells after a second round of damage (Thomas and Raible 2019). Thus, after depletion by symmetric division and differentiation of progeny into new hair cells, precursors are replaced.

These studies suggest that progenitor behavior within the neuromast depends on spatial location. Thomas and Raible (2019) used CRISPR-Cas9 technology (Sect. 2.4.2) to knock in fluorescent reporters into genes that were previously shown to have distinct and polarized expression patterns within neuromasts. Three genes generated distinct spatial expression patterns: *sfrp1a* drove expression in peripheral supporting cells, *sost* in DV supporting cells, and *tnfsf10l3* in a ring of supporting cells near the periphery (but primarily anteroposterior [AP] supporting cells). Using lineage tracing, the authors tested the ability of each supporting cell population to give rise to hair cells after neomycin-induced hair cell death. DV supporting cells gave rise to the majority of regenerated hair cells (~60%), with lesser contributions from AP supporting cells (~20%) and peripheral supporting cells (~4%). It was further shown that specifically ablating DV cells reduced hair cell regeneration, suggesting that other supporting cells did not compensate for their loss. In addition, AP cells, peripheral cells, and more centrally localized DV cells could all regenerate DV cells.

Single cell RNA sequencing (scRNA-Seq) has further supported the existence of multiple supporting cell subtypes (Lush et al. 2019). Sequencing at the single cell level allows for identification of rare cell types and developmental transitions that might be missed by population RNA sequencing (Sect. 2.4.1). Using this technique, the authors isolated over 1500 neuromast cells from 5-day-old zebrafish and identified seven distinct cell types: mantle cells, central supporting cells, AP-pole supporting cells, DV-pole amplifying supporting cells, differentiating hair cell progenitors, and young hair cells, and mature hair cells. Such data

should provide a useful starting point for identifying factors that regulate supporting cell identity and hair cell differentiation. Although this study examined neuromasts under homeostatic conditions, future studies may perform similar RNA-Seq experiments in regenerating neuromasts to see how gene expression profiles and developmental trajectories shift during hair cell regeneration.

2.3.2 The Role of Peripheral Supporting Cells in Fish

Studies of amphibians, such as the axolotl salamanders *Ambystoma punctatum* and *Ambystoma mexicanum*, have shown that existing lateral line neuromasts can give rise to entirely new neuromasts during the process of tail-tip regeneration (Stone 1937; Jones and Corwin 1993). Similar phenomena occur in zebrafish (Dufourcq et al. 2006). The source of new neuromasts are the peripheral supporting cells of an existing neuromast close to the amputation site, which divide and form a placode that migrates along the regenerating tail. Similarly, during the growth of the adult lateral line system in zebrafish, new neuromasts bud from the periphery of existing neuromasts (Wada et al. 2010; Iwasaki et al. 2020). In both of these cases, peripheral supporting cells divide and give rise to migrating clusters of cells resembling the lateral line primordia that deposit neuromasts during development. Based on these results, peripheral supporting cells are thought to be capable of producing all cell lineages within the neuromast.

Understanding conditions that provoke peripheral supporting cells to divide and produce other cell types within neuromasts has proven difficult. In the absence of damage, peripheral supporting cells divide rarely, and when they do, they are usually observed only to produce other peripheral supporting cells (Romero-Carvajal et al. 2015).When hair cells are killed using neomycin, peripheral supporting cells maintain relatively low levels of proliferation and do not usually give rise to new hair cells (Romero-Carvajal et al. 2015; Thomas and Raible 2019). In another fish species, medaka (*Oryzias latipes*), long-term lineage tracing showed that

peripheral supporting cells can give rise to clones containing peripheral supporting cells, internal supporting cells, and hair cells (Seleit et al. 2017). Thus, peripheral supporting cells might continuously produce internal supporting cells at a very low rate during homeostasis, perhaps explaining why this phenomenon has not been seen in studies that only tracked cell divisions over several days.

Given these data, some have proposed that peripheral supporting cells are a latent stem cell population that only responds to severe injuries. As described previously in this section, tail-tip amputation (which ablates entire neuromasts) induces peripheral supporting cell division, but hair cell ablation alone does not. Several studies have attempted to address whether larger scale injuries within the neuromast induce peripheral supporting cell division. In one study, the authors laser ablated 40% to 95% of neuromast cells in medaka, leaving behind a few peripheral supporting cells (Seleit et al. 2017). As few as four peripheral supporting cells could regenerate the neuromast and all cell types within it. In a similar study using laser ablation of neuromast cells in zebrafish, a mixture of two to three peripheral supporting cells and two to seven internal supporting cells was enough to regenerate the neuromast to 70% of its normal size at 7 days post-injury (Viader-Llargués et al. 2018). Time-lapse imaging of regenerating neuromasts revealed that internal supporting cells also produced all three major cell types of the neuromast, but peripheral supporting cells only appeared to produce other peripheral supporting cells.

What could explain the differences in peripheral supporting cell behavior observed in these studies? One possibility is that peripheral supporting cells behave differently in medaka compared to zebrafish. Another possibility is that peripheral supporting cells only contribute substantially to regenerating other cell types when damage includes internal supporting cells as well as hair cells. Supporting this idea, peripheral supporting cells gave rise to DV-localized supporting cells when DV cells were ablated (Thomas and Raible 2019). One caveat is that different markers for peripheral supporting cells were used in all three of these studies, so it is

possible that these studies are not investigating the exact same cell subtypes. More research is needed to resolve these discrepancies and conclusively define their role within the neuromast.

It also remains unknown what signals regulate peripheral supporting cell identity. One possibility is that neuromast border cells (nBCs) provide signals to peripheral supporting cells (Seleit et al. 2017). nBCs are specialized epithelial cells surrounding the neuromast that are induced to form as neuromasts develop. They constitute an independent epithelial lineage and can regenerate themselves after damage. The existence of nBCs seems to be conserved across fish species. As cells that surround the neuromast and directly contact peripheral supporting cells, nBCs are a good candidate for cells that might form a niche to maintain peripheral supporting cell identity.

2.3.3 Supporting Cell Diversity in Birds

Relative to zebrafish, fewer studies have explored supporting cell heterogeneity in birds. In the chick BP, there are differences in supporting cell shape across the radial width of the epithelium: While nuclei of supporting cells in the neural half of the epithelium reside close to the basal lamina, those in the abneural half reside almost halfway between the basal lamina and the lumen (e.g., Scheibinger et al. 2018). Another sign of supporting cell heterogeneity in birds is their regionalized expression of certain genes under normal conditions and after damage. Janesick et al. (2021) used scRNA-seq to determine that, while supporting cells throughout the uninjured BP express many common genes, some genes are transcribed at very different levels in supporting cells located in different zones in the BP (neural versus abneural). Similarly, in the undamaged chick utricle (a vestibular organ), transcripts for some Notch pathway genes are abundant in supporting cells in the striola (a specialized region near the center of the epithelium) but are scarce outside of this region (Warchol et al. 2017). Following gentamicin treatment, the chick BP upregulated expression of Notch pathway genes *Ser1* and *Hes5*, and a

Notch pathway modulator *Lfng* (Daudet et al. 2009). The increased expression of these genes was observed only in supporting cells in the neural region, despite global hair cell loss. It is unclear if these restricted patterns of gene expression reflect functionally significant differences in supporting cell populations.

The behaviors of supporting cells also vary across the zones of the damaged BP. The majority of supporting cell divisions following gentamicin damage occurred in the neural (superior) portion of the sensory epithelium (Cafaro et al. 2007). Consistent with this, most regenerated hair cells in the neural half of the BP were derived via supporting cell mitosis, while most cells in the abneural half appeared to have been formed by direct transdifferentiation (Cafaro et al. 2007). It is not clear why these two paths toward a new hair exist, whether supporting cells are predetermined for one path or the other, of if a given supporting cell is simply influenced by its microenvironment to divide or directly transdifferentiate. These are interesting areas for further study, as is the question of the molecular mechanisms that guide a supporting cell toward the hair cell fate using either path.

There is evidence that stemlike cells reside among supporting cells in avian inner ear epithelia (reviewed in Stone and Cotanche 2007; Kelley and Stone 2017). For instance, cell divisions in the chick BP and utricle can yield cells with asymmetric fate outcomes (one hair cell and one supporting cell; Roberson et al. 1992; Stone and Rubel 2000; Scheibinger et al. 2018). Furthermore, the quail BP regenerates hair cells after repeated rounds of hair cell damage (Niemiec et al. 1994). These findings strongly suggest that bipotential cells (i.e., cells that can form at least two cell types) exist, and these cells can replenish hair cell progenitors. For a more detailed consideration of inner ear stem cells, see Janesick, Heller, and Hashino, Chap. 6.

2.4 Approaches to Define New Molecular Regulators Using Nonmammals

When supporting cells regenerate hair cells after injury, they leave their normal "resting" state and either divide or change phenotype. The specific molecular events that initiate these processes are not fully known. They could be associated with disruption of signals that healthy hair cells normally send to supporting cells via direct cell-cell contacts or diffusible substances. Alternatively, supporting cell transdifferentiation may be triggered by shifts in other aspects of the epithelial microenvironment during or after damage. Afferent and efferent nerves, which course through the epithelium, appear dispensable for avian hair cell regeneration because new hair cell-like cells still form in sensory organs that were dissected away from other cells in the nervous system and grown in vitro (e.g., Matsui et al. 2000) and in cultures of dissociated supporting cells (e.g., Stone et al. 1996). It is also unlikely that immune cells such as macrophages are necessary for hair cell regeneration in avian auditory organs because depletion of macrophages in the BP does not affect numbers of hair cells that get replaced (Warchol et al. 2012). Similarly, although macrophages respond to hair cell damage in the zebrafish lateral line, they are not required for regeneration (Warchol et al. 2021). Although innervation is not necessary for the initial development of zebrafish lateral line hair cells (Grant et al. 2005; Suli et al. 2016), changes in innervation result in reduced hair cell regeneration (Hardy et al. 2021).

It is of great interest to identify the molecules and molecular pathways that direct hair cell regeneration in nonmammals because such knowledge may lead to methods for promoting a similar form of regeneration in the ears of mammals. Scientists have taken advantage of new genomic methods to identify candidate regulators, which include transcriptional profiling, mutagenesis studies, and small-molecule testing. Each of these approaches is unique and described separately below.

2.4.1 Transcriptional Profiling

Identification of proteins that are key regulators of cellular processes such as cell

death, division, differentiation/maturation, and innervation during hair cell regeneration is an important focus of research. Because cells tend to “upregulate” or “downregulate” synthesis of proteins as they become needed or dispensable, one approach toward identifying such potential regulators is to determine which proteins are generated during important phases of regeneration (e.g., as hair cells are dying, supporting cells are dividing, or hair cells are differentiating and synapses are forming). Direct identification of proteins and their patterns of expression can be accomplished with proteomics and immunolabeling. However, proteomics requires large amounts of biological material, which is difficult to obtain with inner ear epithelia, and most immunolabeling approaches require knowledge a priori of proteins of interest. Instead, determination of the types and numbers of mRNA transcripts that are present at key times after damage is often used as a proxy. Although every transcript will not necessarily yield a functional protein, transcriptional profiling is very effective for identifying potential protein candidates for further study.

The first studies to apply transcriptional profiling to study nonmammalian hair cell regeneration were conducted in utricles and cochlea of chickens (Hawkins et al. 2003, 2007; Frucht et al. 2010). A similar approach by Frucht et al. (2010) used microarrays to identify changes in gene expression associated with activation of adenylyl cyclase (AC), which promotes mitotic hair cell regeneration in the chick BP. These groups identified numerous transcripts whose numbers changed significantly in sensory epithelial cells after drug damage or AC activation, and they validated changes in transcripts using reverse quantitative polymerase chain reaction or RNA in situ hybridization. Furthermore, Frucht et al. (2010, 2011) predicted through analysis in silico that microRNA 181a controls the levels of transcripts whose expression changed in association with AC activation, implicating microRNA 181a as a regulator of supporting cell proliferation, and they obtained evidence to support that hypothesis. Additional microarray analysis of cells from the sensory epithelium of the chick utricle indicates that an

RNA-binding protein called MSI1 may play a role in avian hair cell regeneration (Wakasaki et al. 2017). Microarrays have also been used to profile gene expression in the regenerating inner ear (Schuck et al. 2011) and lateral line (Behra et al. 2012; Steiner et al. 2014) of zebrafish.

Other studies performed transcriptional profiling using RNA sequencing (RNA-Seq), a technique that significantly expands the number of transcripts that can be examined. Using this approach, Ku et al. (2014) identified FGF20 as a negative regulator of supporting cell proliferation in the chick utricle. A subsequent microarray analysis showed that FGFs and their receptors are also dynamically regulated at the transcriptional level in the BP following hair cell damage (Lee et al. 2016) and that the transcription factor CMYC is another potent regulator of supporting cell division during avian hair cell regeneration. Further studies showed dynamic expression of genes in the Notch, FGF, Wnt, and BMP pathways after hair cell damage (Jiang et al. 2018; Matsunaga et al. 2020). Finally, RNA-Seq approaches have also been used to compare supporting cell types in adult zebrafish and mouse ears (Giffen et al. 2019) and to study regeneration in the adult zebrafish ear (Liang et al. 2012) and the larval lateral line (Jiang et al. 2014), revealing potential roles for Stat, Wnt and Notch signaling.

A more refined transcriptional profiling method, single cell RNA sequencing (scRNA-Seq), has subsequently emerged as a method to analyze gene expression of individual cells. The method yields expression data that would otherwise be lost with whole tissue extraction of mRNA. This method has been used to profile zebrafish lateral line cells (Lush et al. 2019), which has identified distinct cell phenotypes and also suggested roles for Fgf signaling in hair cell regeneration. Another study used scRNA-Seq to explore properties of quiescent supporting cells in the undamaged chick BP (Janesick et al. 2021). We expect that this powerful method will play an increasingly important role in regeneration research.

2.4.2 Genetic and Molecular Screening

Another powerful approach toward identifying regulators of cellular processes underlying hair cell regeneration is genetic screening. During a forward genetic screen, researchers induce random mutations to identify genes that affect hair cell regeneration. Forward screens are common in organisms that breed rapidly, such as the fruit fly *Drosophila melanogaster*. Although fruit flies have hearing organs (called Johnston's organs) and investigators have begun to use them as a model to study hair cell genetics (e.g., Li et al. 2016, 2018), we do not know if they regenerate auditory receptors after damage. Given their speed of reproduction, zebrafish have been used in forward genetic screens to study hair cell development. For instance, a novel gene, *phoenix*, was identified by Behra and colleagues as part of an insertional mutagenesis screen in zebrafish (Behra et al. 2009). Mutants developed normal neuromasts but, in contrast to wild-type fish, hair cells failed to regenerate after damage induced by copper and neomycin because supporting cells did not divide. The mutation is lethal, indicating that *phoenix* has other functions besides regeneration. So far, there have been few reports of screens designed to identify genes that are specific regulators of hair cell regeneration.

Targeting individual genes for inactivation is often called reverse genetics, as the gene identity is known before the loss of function phenotype. In this approach, genes of interest are often identified by transcriptional profiling and inactivated using antisense oligonucleotides or RNA interference (RNAi). Transcription factor pathways including PAX and AP1 were identified by an RNAi screen of genes involved in regeneration of avian sensory epithelia (Alvarado et al. 2011). Rapid advances in genomic engineering using CRISPR and other approaches have made the reverse genetic approach feasible for assessing large numbers of targeted mutations by phenotypic screening. This approach can avoid some of the off-target effects of targeted interference with antisense oligonucleotides or RNAi. Pei and colleagues have used this approach to screen a set of mutations in genes that are differentially expressed in the adult zebrafish inner ear by transcriptional profiling (Pei et al. 2016, 2018). Systemic screening of 254

genes identified seven genes that, when mutated, affected hair cell regeneration. Disruption of these genes also altered other types of regeneration including fin and liver, suggesting that a common set of genes may play general roles in these regenerative processes.

As an alternative to genetic screens, small-molecule screening provides a way to assess different potential regulatory pathways. Witte, Montcouquiol, and colleagues screened a panel of 13 signaling pathway inhibitors to identify those that altered proliferation in chick (Witte et al. 2001) and mouse (Montcouquiol and Corwin 2001) utricle cultures. In parallel, these studies found that blocking PI3K and mTOR pathways reduced proliferation of supporting cells. Similar studies have been performed using zebrafish to identify drugs that alter hair cell regeneration in the lateral line (Namdaran et al. 2012). Screening a 1680 compound library of drugs with known biological activity revealed that glucocorticoids enhanced hair cell addition, while drugs that blocked mitosis inhibited regeneration. Although drug screens can be effective in identifying potential signaling pathways involved in biological processes, drug action can be the result of off-target effects rather than effects on the pathway the drug was developed for. If the target is unknown, it can be very challenging to determine the mechanistic cause of drug action.

In conclusion, the application of the genetic approaches has, and will continue to, expand and accelerate our understanding of how nonmammalian hair cell regeneration is regulated. These approaches will also provide important clues as to how hair cell replacement may be stimulated in the hearing organ, and augmented in the vestibular organs, of mammals. Although considerable progress has been made over the past 10 years using these genetic tools, considerably more work is needed to identify the set of genes that are necessary to drive full morphological and functional recovery.

2.5 Molecular Regulation of Supporting Cells

In this section, we review current knowledge of the signals that control hair cell regeneration in nonmammalian vertebrates. These insights were obtained using the tools described in Sect. 2.4, as well as "best guess analysis" based on published data from other systems or developing hair cell epithelia. For additional reviews, we point readers to Stone and Cotanche 2007; Oesterle and Stone 2008; Warchol 2011; Kelley and Stone 2017.

2.5.1 Transcription Factors Regulate Hair Cell Regeneration in Nonmammals

Transcription factors are proteins that regulate gene expression and act in context-dependent manners (i.e., in specific times and specific cell types) to maintain a cell's status or to effect a change in status. Much is known about how transcription factors control the formation of hair cells during embryogenesis (discussed in McGovern and Groves, Chap. 5). Because hair cell regeneration may, in many ways, recapitulate development, a number of studies have explored how developmentally relevant transcription factors could influence hair cell replacement later in life. Two examples of these factors are ATOH1 and SOX2.

ATOH1 is a transcription factor in the basic helix-loop-helix family that appears necessary for acquisition of a hair cell phenotype in all vertebrates (e.g., Bermingham et al. 1999; Millimaki et al. 2007). Moreover, misexpression of *Atoh1* (forced expression at an abnormal time, place, or level) induces cells in the developing mammalian inner ear to acquire the hair cell fate (e.g., Zheng et al. 2000; Liu et al. 2012). In mature sensory organs lacking hair cell damage, there is little expression of *ATOH1/atoh1a/atoh1b* in hair cells or supporting cells (e.g., Cafaro et al. 2007; Ma et al. 2008, Figure 2.3), although small levels of expression are always present in organs that undergo hair cell turnover (e.g., chick utricle and zebrafish neuromasts). Following damage, however, *ATOH1/atoh1a/atoh1b* expression at mRNA and protein levels becomes highly upregulated in supporting cells (Cafaro et al. 2007; Ma et al. 2008). As described in these studies and others, increased expression of *Atoh1* is one of the

earliest pro-regenerative responses in nonmammalian supporting cells. *Atoh1* becomes elevated in at least some dividing supporting cells, as well as in supporting cells that undergo direct transdifferentiation and in differentiating hair cells. Its expression returns to baseline levels once regenerated hair cells have matured.

In the chick BP, misexpression of *ATOH1* causes overproduction of hair cells and stimulates supporting cell division (Lewis et al. 2012). Because of Atoh1's powerful roles in hair cell development and nonmammalian hair cell regeneration, several studies have examined whether *Atoh1* misexpression also induces hair cell regeneration in the ears of mammals. Results of those studies are discussed in Forge and Taylor, Chap. 4, and McGovern and Groves, Chap. 5.

In contrast to *ATOH1*, some transcription factors are broadly expressed in supporting cells under normal conditions (i.e., in mature undamaged epithelia). Two examples are the SRY box transcription factor *SOX2* (Neves et al. 2007; Oesterle et al. 2008) and the basic-loop-helix transcription factor *ID2/3* (Lewis et al. 2012), both of which are required for hair cell development (Kiernan et al. 2005; Jones et al. 2006a; Kamaid et al. 2010). Following damage to the chick BP, expression of both SOX2 and *ID2/3* is downregulated in supporting cells in spatial and temporal concert with the increased expression of *ATOH1*, as supporting cells directly transdifferentiate into hair cells (Cafaro et al. 2007; Lewis et al. 2018). This reduced expression of supporting cell-specific transcription factors presumably occurs as supporting cells downregulate expression of genes that maintain the supporting cell fate and upregulate genes that promote either hair cell fate or cell division. Further study will be necessary in order to understand the specific roles of ID and SOX transcription factors during avian hair cell regeneration.

Studies of zebrafish have revealed that mutations in *sox2* and the closely related family member *sox3* affect the initial formation of the otic placode as well as subsequent development

of hair cells and innervating neurons (Gou et al. 2018a; 2018b). Both transcription factors cooperate during the establishment of the placode but appear to play distinct roles in the differentiation of sensorineural structures: Sox2 promotes hair cell differentiation, while Sox3 promotes neuronal differentiation. *Sox2* is also expressed in the migrating lateral line primordium and in supporting cells in mature neuromasts (Hernández et al. 2007). Following hair cell death, *sox2*-expressing supporting cells divide and downregulate *sox2* as they differentiate into hair cells (Hernández et al. 2007). Because some later divisions also produce more supporting cells, the *sox2*-expressing population is usually not depleted during hair cell regeneration.

More severe injuries in zebrafish can deplete the *sox2*-expressing population. For example, when fish are first treated with Notch inhibitor to force hair cell overproduction (see Sect. 2.5.2.1) and then treated with neomycin to ablate hair cells, the number of *sox2*-positive supporting cells is reduced (Romero-Carvajal et al. 2015; Ye et al. 2020). However, *sox2*-expressing supporting cells were shown to regenerate from surviving *atoh1a* + supporting cells through *yap1*-mediated upregulation of the RNA-binding protein *lin28a* (Ye et al. 2020). *Lin28a* inhibits the microRNA *let7,* which activates Wnt signaling and promotes progenitor renewal. This suggests that some *atoh1a* + supporting cells within neuromasts can respond to severe injury by upregulating *sox2* and dividing to renew the *sox2*-positive population.

2.5.2 Cell-Cell Signaling Molecules That Regulate Hair Cell Regeneration in Birds and Fish

Cellular behaviors are influenced by signaling molecules that enable cells to communicate with each other. The vast majority of molecules known to control hair cell regeneration are proteins, but signaling agents can also be ions, lipids, or other molecules. Signaling molecules can act at close range upon adjacent cells, or they can diffuse or be

transported to cells at a distance. In this section, we discuss signaling pathways known to regulate nonmammalian hair cell regeneration, as summarized in Figure 2.3.

2.5.2.1 Notch Signaling

Probably the best studied signals that control nonmammalian hair cell regeneration are those that act through the Notch receptor. Notch receptors are bound by Delta/Serrate/Jagged ligands that are usually found on the membranes of adjacent cells. When such ligands bind Notch, they cause its intracellular domain (NICD) to be proteolytically cleaved by gamma secretase. NICD then translocates to the nucleus, where it acts as a transcriptional activator. NICD promotes expression of Hes/Hey/Her transcriptional repressors that reduce expression of Atoh1 and Notch ligands (Zheng et al. 2000), thereby preventing the cell from adopting the hair cell fate. Because Notch-ligand interactions require cell-cell contacts, cells not adjacent to the ligand-expressing cell are permitted to become hair cells. As a result, Notch signaling establishes a pattern of alternating hair cells and supporting cells and ensures the formation of the normal mosaic structure of the sensory epithelium (reviewed in Kelley 2003; Chitnis et al. 2012; Kelley and Stone 2017). Disruption of Notch signaling during embryogenesis leads to production of excess hair cells, inappropriate organ size, and improper cellular patterning. These changes occur because Notch inhibition increases proliferation of supporting cells and causes inappropriate cell fate determination: cells are diverted from becoming supporting cells and instead acquire the hair cell fate (e.g., Haddon et al. 1998; Itoh and Chitnis 2001).

In mature sensory epithelia, Notch pathway components continue to be expressed under homeostatic conditions. *NOTCH1* is expressed by supporting cells in the chick BP (Stone and Rubel 1999), while several Notch receptors are expressed by supporting cells in zebrafish neuromasts (*notch1a/b*, *notch3*) (Romero-Carvajal et al. 2015). Jagged family ligands (*SERRATE1* in chick, *jagged2b* in zebrafish) are expressed in supporting cells (Stone and Rubel

1999; Romero-Carvajal et al. 2015). Although the function of Jagged ligands in mature sensory epithelia has not been well explored, it is required in mice for maintenance of Hensen's cells, which are laterally positioned supporting cells in the organ of Corti (Chrysostomou et al. 2020). Delta ligands are expressed in hair cell precursors and in regenerated hair cells that have yet to fully differentiate (Stone and Rubel 1999; Ma et al. 2008; Jiang et al. 2014). Pharmaceutical inhibition of Notch after hair cell damage caused hair cell overproduction in lateral line neuromasts (Ma et al. 2008; Romero-Carvajal et al. 2015) as well as in chick BPs (Daudet et al. 2009; Jiang et al. 2018) and utricles (Warchol et al. 2017) grown in culture. The increase in hair cell numbers occurs at the expense of supporting cells. Thus, regenerated hair cells express Delta, which signals to Notch in surrounding supporting cells and prevents them from adopting a hair cell fate. This mechanism ensures that the proper ratio of hair cells to supporting cells is reestablished after damage.

Given the developmental role of Notch in inhibiting hair cell production and the finding that Notch is expressed postnatally, it was first postulated that Notch signaling might, under homeostatic conditions, maintain supporting cell quiescence and prevent them from transdifferentiating into hair cells. However, while Notch inhibition led to increased hair cell production after neomycin-induced hair cell loss, it had no effect on hair cell number in undamaged neuromasts (Ma et al. 2008; Wibowo et al. 2011). Similarly, Notch inhibition in the regenerating chick BP led to an overproduction of replacement hair cells (Daudet et al. 2009). Notably, such overproduction only occurred in regions where significant hair cell damage occurred but not in undamaged regions of the BP. Notch inhibition therefore appears to be insufficient to trigger hair cell production in both the BP and lateral line neuromasts under homeostatic conditions.

In the regenerating chick BP, supernumerary hair cells that were produced in response to blocking Notch activity were generated by both cell division and direct transdifferentiation,

indicating that either supporting cells or postmitotic precursor cells could be coaxed to form hair cells in the absence of Notch (Daudet et al. 2009). However, Notch inhibition did not result in increased supporting cell division, so a subset of supporting cells transdifferentiated into hair cells and were not replenished.

A radically different response to Notch inhibition was observed in the chick utricle. Inhibiting of Notch in undamaged utricles led to a dramatic increase in supporting cell division without significant hair cell loss (Warchol et al. 2017). Thus, the homeostatic chick utricle seems to have fewer intrinsic brakes on supporting cell division than the BP. This finding is not surprising because there is significant turnover of hair cells throughout chick utricles under normal conditions (Kil et al. 1997), and the process of turnover would be hampered if cell division were suppressed under homeostatic conditions. The mechanisms that block cell proliferation and new hair cell production in regions with normal hair cell densities have not been identified, but they are most likely derived from the hair cells themselves. Furthermore, the reasons why zebrafish neuromasts and chick utricles respond differently to Notch inhibition under apparently homeostatic conditions are not known.

The distinct responses that each hair cell epithelium exhibits in response to Notch inhibition demonstrate clearly that molecular regulation of supporting cell division is unique in each context. Furthermore, these findings reveal that other inhibitory mechanisms beside Notch signaling prevent supporting cells from dividing and/or transdifferentiating into new hair cells. This finding has important implications for the development of therapies for promoting hair cell regeneration in mammals. Indeed, the potent inhibitory role of Notch that occurs during development in vertebrates and during regeneration in nonmammalian vertebrates had prompted the exploration of whether Notch signaling might block hair cell regeneration in mature mammals. A number of studies have found that inhibition of Notch activity promotes

regeneration in the damaged mouse utricle but not the cochlea. These studies are discussed in detail in Forge and Taylor, Chap. 4, and in McGovern and Groves, Chap. 5.

In addition to its role in regulating supporting cell proliferation and hair cell differentiation, Notch signaling also appears to play an important role in regulating hair cell maturation, controlling the cell polarity that determines their directional sensitivity to mechanical stimulation. The transcription factor Emx2 plays a central role in this process (Jiang et al. 2017; Ji et al. 2018). Emx2 is expressed in about half of all hair cells in the developing mouse utricle. Those Emx2-positive hair cells all display the same polarity, while Emx2-negative hair cells have the opposite polarity. Emx2 was shown to be both necessary and sufficient for determining hair cell polarity across multiple species and sensory epithelia. Studies suggest Notch signaling acts to determine which hair cells express Emx2 (Jacobo et al. 2019; Kozak et al. 2020). To what extent these different functions of Notch signaling – regulating supporting cell proliferation, cell fate choice, and differentiation of hair cell polarity – are controlled by distinct Notch receptors and ligands is unknown. In addition, understanding how Notch signals result in different outcomes in different contexts will require further research.

2.5.2.2 Wnt Signaling

Wnt has emerged as an important regulator of hair cell regeneration in birds and fish. Wnt ligands regulate cell division and differentiation in a variety of cell types in the body. Expression of *WNT*s, their receptors (*FZD*s), their effectors (e.g., ß-catenin), and their modulators (e.g., *DKK*s, *SFRP*s) is altered in supporting cells following hair cell damage in the chick utricle (Alvarado et al. 2011; Ku et al. 2014). Knockdown of *WNT4* in cell cultures of avian utricular supporting cells inhibits their proliferation (Alvarado et al. 2011), while activation of the WNT effector ß-catenin in the chick BP promotes supporting cell division (Jiang et al. 2018). Similar findings have been reported in studies of zebrafish lateral line neuromasts, in which

activation of Wnt signaling increases supporting cell proliferation during development and regeneration, leading to increased hair cell numbers (Head et al. 2013; Jacques et al. 2014). Unlike Notch, Wnt does not appear to affect fate decisions of dividing supporting cells because both hair cell and supporting cell numbers increase in response to Wnt activation (Jacques et al. 2014; Romero-Carvajal et al. 2015). Wnt pathway genes are not expressed during homeostasis in mature neuromasts, and during regeneration, proliferation begins prior to significant upregulation of Wnt (Jiang et al. 2014). This suggests that signals other than Wnt are responsible for the initial phase of regeneration in the lateral line.

Studies of the zebrafish lateral line have further elucidated the interplay between Notch and Wnt signaling during homeostasis and regeneration. Components of both Notch and Wnt signaling have polarized expression patterns within neuromasts (Jiang et al. 2014; Romero-Carvajal et al. 2015). Notch normally inhibits Wnt signaling during homeostasis by promoting expression of the Wnt inhibitor *dkk2* (Romero-Carvajal et al. 2015). Following hair cell death, Notch is transiently downregulated, and subsequently, Wnt is upregulated (Jiang et al. 2014; Romero-Carvajal et al. 2015). Treatment with a gamma secretase inhibitor disrupts the polarity of supporting cell divisions during homeostasis and regeneration, causing divisions to be found throughout the neuromast instead of localized to the DV compartment (Romero-Carvajal et al. 2015). It is possible that Notch signaling more strongly suppresses proliferation outside the DV region, perhaps by inhibiting Wnt, which may explain why DV cells contribute more to hair cell regeneration (Wibowo et al. 2011; Thomas and Raible 2019).

2.5.2.3 Other Signaling Pathways

Work in the past 10 years revealed at least three tyrosine kinase receptors to be important regulators of hair cell regeneration in chick epithelia. Both epidermal growth factor (EGF) and vascular endothelial growth factor (VEGF) are required for supporting cell division in

the aminoglycoside-treated chick BP. EGF and VEGF ligands bind to their corresponding receptors, known as the EGF receptor (EGFR) and the VEGF receptor (VEGFR), to initiate downstream signaling. Inhibition of EGFR in cultured chick cochlear ducts significantly reduced supporting cell division (White et al. 2012) as did VEGFR antagonists (Wan et al. 2020). As anticipated, treatment of cultures with recombinant VEGF caused higher numbers of hair cells to be regenerated (Wan et al. 2020). *VEGFA* is expressed highly in normal hair cells, while *VEGFRs* are expressed in supporting cells. Wan et al. (2020) suggest that release of VEGFA from damaged hair cells may promote supporting cell division. This model is consistent with classical observations that supporting cell division is initiated following visible injury to auditory hair cells (reviewed in Stone and Cotanche 2007).

Fibroblast growth factor (FGF) signaling appears to antagonize hair cell regeneration in the chick ear (Ku et al. 2014; Jiang et al. 2018). In chick utricles, transcripts encoding *FGF20* and its cognate receptor *FGFR3* decreased after hair cell death. Addition of FGF20 to cultured chick utricles curtailed the supporting cell division that follows hair cell loss (Ku et al. 2014), while inhibition of FGFR activity in damaged chick BPs increased numbers of both dividing supporting cells and regenerated hair cells (Jiang et al. 2018).

The function of Fgf signaling in regeneration of hair cells in zebrafish neuromasts is less clear. *Fgf3* is expressed in the central region of the neuromast, while *fgf* receptors are expressed in supporting cells outside the central region (Lee et al. 2016). Fgf pathway components, including *fgf3,* are transiently downregulated following hair cell death in neuromasts (Jiang et al. 2014; Lee et al. 2016; Lush et al. 2019). Lee et al. (2016) found that Fgf inhibition reduced hair cell regeneration and interpreted the loss of *fgf3* transcripts following hair cell death to mean it was expressed in hair cells. However, a later study in which a transgenic knock-in line was created to label *fgf3*-expressing cells found that *fgf3* is expressed in central supporting cells rather than hair cells (Lush et al. 2019). Furthermore, loss of Fgf activity caused increased

supporting cell proliferation and hair cell production during homeostasis and regeneration (Lush et al. 2019). More work is needed to conclusively define the role of Fgf signaling in zebrafish neuromasts.

Retinoic acid (RA) signaling plays many roles during development (reviewed in Rhinn and Dollé 2012). RA is a small-molecule synthesized from retinol (also known as vitamin A) by dehydrogenase enzymes. RA binds to retinoic acid receptors (RARs) that bind directly to genomic RA response elements (RAREs). RA binding changes the activity of RARs from transcriptional corepressors to coactivators. In zebrafish, RA pathway components were transiently upregulated in both the neuromasts and the cristae of the inner ear following hair cell death (Rubbini et al. 2015). Using a dominant negative RAR (dnRAR), the authors found that inhibiting RA signaling reduced supporting cell proliferation and delayed hair cell regeneration. Expression of dnRAR suppressed downregulation of the cyclin-dependent kinase inhibitor *p27^{kip}*, which inhibits reentry into the cell cycle. RA signaling was also required for normal downregulation of *sox2* expression following hair cell loss. These data support a model whereby hair cell loss leads to RA-mediated inhibition of *p27^{kip}* and *sox2* in supporting cells, thereby allowing them to reenter the cell cycle.

It is not known which cells normally act as a source of RA in neuromasts. The gene *aldh1a2*, which encodes a dehydrogenase involved in RA biosynthesis, is expressed in peripheral supporting cells of zebrafish neuromasts (Pittlik and Begemann 2012). A similar expression pattern has been observed in axolotls (Monaghan and Maden 2012). Thus, it is possible that peripheral supporting cells act as a source of RA during hair cell regeneration, although this has yet to be explicitly tested.

Bone morphogenetic proteins (BMPs) bind to receptors with serine-threonine kinase activity and regulate a variety of developmental processes (reviewed in Wang et al. 2014). In the chick BP, *BMP4* is highly expressed in hair cells, and its receptors are expressed in supporting

cells (Jiang et al. 2018; Lewis et al. 2018). During hair cell loss, *BMP4* transcripts decrease substantially, and expression of a BMP4-regulated gene – the transcriptional cofactor, *ID2/3* – is also reduced. When exogenous BMP4 was added to cultured BPs after streptomycin-induced hair cell death, there was significantly less supporting cell division and very few hair cells were regenerated. Furthermore, there was little upregulation of *ATOH1*, which is required for hair cell differentiation. In contrast, inhibition of BMP4 signaling after hair cell loss increased numbers of regenerated hair cells. These findings indicate that BMP4 is a potent inhibitor of supporting cell regenerative responses, suggesting that steady-state BMP4 signaling by hair cells might prevent supporting cells from forming new hair cells in the absence of damage.

Several other signaling pathways have been implicated in regulation of nonmammalian hair cell regeneration including growth hormone (Sun et al. 2011) and the Hippo pathway (Rudolf et al. 2020 see Rudolf and Corwin, Chap. 3). Growth hormone also regulates hair cell addition in fish inner ear organs (Sun et al. 2011). Finally, it is important to acknowledge that some signaling pathways work together to exert additive effects upon hair cell regeneration (e.g., Bai et al. 2021).

2.5.3 Epigenetic Mechanisms Controlling Nonmammalian Hair Cell Regeneration

As discussed above, the process of hair cell regeneration involves changes in gene expression. Gene expression is regulated by the interaction of transcription factors with the promoter and enhancer regions associated with particular genes, and this process is critically dependent on the local structure of chromatin. Chromatin can exist in either “open” or “condensed” configurations, and its structure is determined by enzymatic modification of both histones and DNA. Chromatin remodeling occurs when histones are enzymatically modified (e.g., acetylated or methylated) at specific amino acids, altering chromatin accessibility and the likelihood that a gene or set of genes will be transcribed into mRNA. DNA methylation is

another mechanism that alters gene transcription. Together, these types of modifications are called *epigenetic*, as they alter gene expression without altering the gene sequence encoded in DNA. Such epigenetic regulation is likely to play an influential role in how, when, and to what extent hair cells are regenerated in all vertebrates.

At this point, there has been little work done on epigenetic regulation of hair cell regeneration, except with respect to chromatin remodeling (see below). In contrast, there is a rapidly growing body of work on epigenetic control of hair cell development (see Yizhar-Barnea et al. 2018; reviewed in Doetzlhofer and Avraham 2017). One key result is that epigenetic modification of *Atoh1* regulatory elements is correlated temporally with the loss of regeneration potential in the mammalian cochlea during the early postnatal period (Stojanova et al. 2016). This work and other epigenetic studies pertaining to mammalian hair cell development and regeneration are discussed in Forge and Taylor, Chap. 4, as well as McGovern and Groves, Chap. 5.

Changes in chromatin structure can occur via either acetylation or methylation of histones or DNA. Several studies have examined how histone acetylation affects hair cell regeneration in chicks and fish. Slattery et al. (2009) showed that treatment with several inhibitors of histone deacetylases (HDACs) resulted in decreased proliferation of supporting cells but did not affect hair cell replacement. A similar study examined the effects of the HDAC inhibitors on regeneration of lateral line hair cells in larval zebrafish and observed reduced supporting cell division and fewer regenerated hair cells (He et al. 2014). Since histone acetylation is typically associated with “open” chromatin, these results suggest that the expression of certain genes needs to be repressed (via deacetylation of histones) in order for regeneration to occur. He et al. (2016) further found that an inhibitor of histone methylation, lysine-specific demethylase 1 (Lsd1), may also be a significant regulator of hair cell regeneration in zebrafish neuromasts. Blockade of Lsd1 using a pharmaceutical agent reduced supporting cell

division after neomycin treatment (He et al. 2016) and also reduced cell division in developing neuromasts (He et al. 2013). Together, the results of these three studies imply that epigenetic changes may be necessary for the induction of regeneration in nonmammals. However, all studies employed pharmacological inhibitors that may have "off-target" effects. Additional studies are needed to identify regeneration-relevant genes that are impacted by epigenetic modifications.

2.6 Conclusion

Nonmammalian vertebrates have a natural capacity to regenerate hair cells in their lateral line, hearing, and vestibular sensory organs. Chickens and zebrafish have been the most common nonmammalian animal subjects for scientists to build an understanding of the cellular and molecular mechanisms that stimulate supporting cells to form new hair cells after damage. It is anticipated that studies in these species will continue to point us in the direction of therapies that can promote hair cell regeneration in mammals and result in improved hearing and balance function following hair cell loss.

Acknowledgments

The authors thank Mark Warchol, Allison Coffin, and Art Popper for comments on this manuscript.

Compliance with Ethics Requirements

Madeleine N. Hewitt declares that she has no conflict of interest.

David W. Raible declares that he has no conflict of interest.

Jennifer S. Stone declares that she has no conflict of interest.

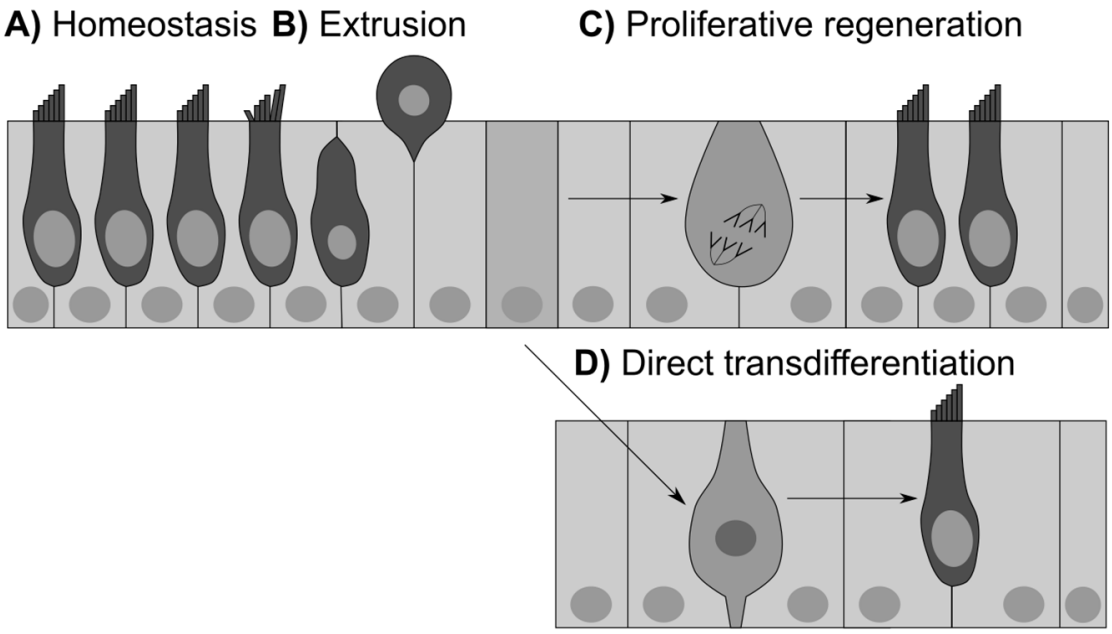

Figure 2.1: Known mechanisms of hair cell regeneration in nonmammals.

(A) In the absence of damage, hair cells and supporting cells are regularly arranged within the sensory epithelium. Hair cells have regular, staircase-shaped stereocilia, and supporting cells interdigitate between hair cells.

(B) When hair cells are damaged, the stereocilia can become splayed and disorganized, the supporting cells may facilitate extrusion of the apical region of the hair cell (including the stereocilia), and the damaged hair cells may be apically extruded or undergo intra-epithelial degeneration. Following hair cell loss, some supporting cells generate new hair cells, either through proliferation or direct transdifferentiation.

(C) During proliferative regeneration, which occurs in lateral line neuromasts and chick inner ear organs, one supporting cell divides symmetrically to form two new hair cells or supporting cells, or asymmetrically to form a hair cell and a supporting cell; two new hair cells are shown in this example.

(C) During direct transdifferentiation, which occurs in the avian vestibular system, a single supporting cell directly converts to a hair cell fate. (Figure © 2022 Madeleine Hewitt, all rights reserved)

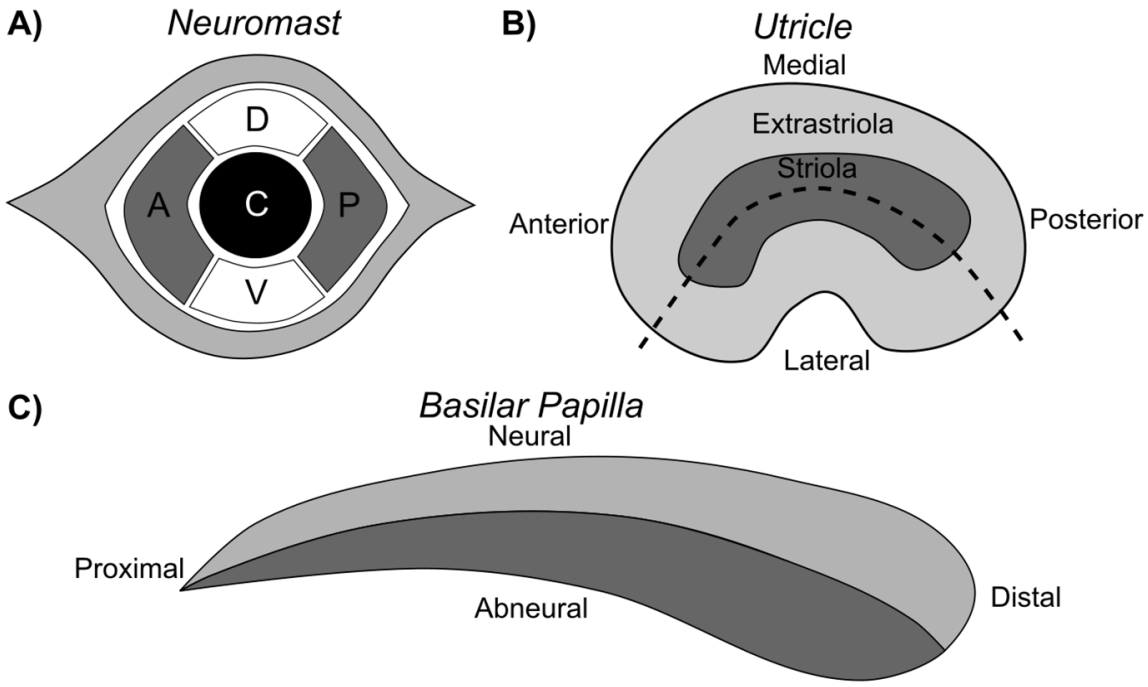

Figure 2.2 Anatomical locations and axes for the three sensory epithelia described in this chapter: the neuromast, utricle, and basilar papilla (not to scale).

(A) The neuromast is divided into the central region (c), dorsal and ventral (DV) compartments, and anterior and posterior (AP) compartments. Peripheral supporting cells forms a ring around the neuromast (light gray).

(B) The utricle is divided into the striola (dark gray, center) and the extrastriolar regions, with the line of polarity reversal (LPR, dashed line) dividing the center.

(C) The basilar papilla is defined by the proximal-distal (sometimes also called basal-apical) and the neural-abneural axes. The neural-abneural axis is so named because only hair cells on the neural side receive afferent innervation. (Figure © 2022 Madeleine Hewitt, all rights reserved)

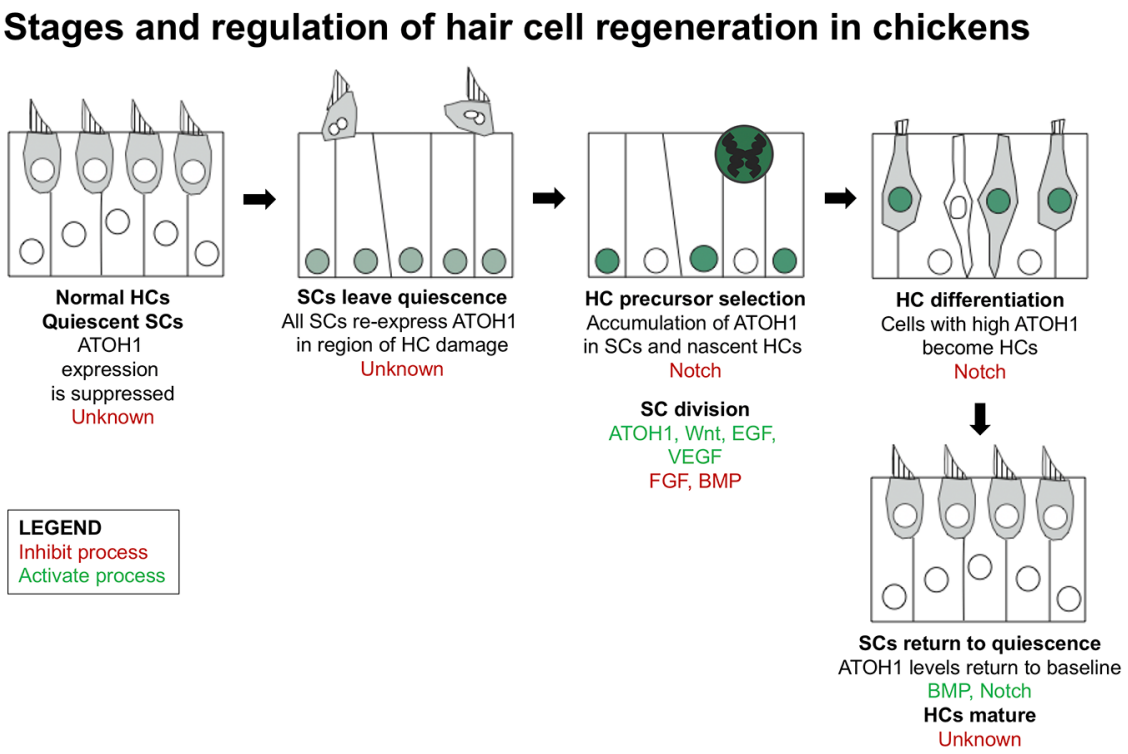

Figure 2.3 Different stages of hair cell regeneration in chickens and description of the molecules known to either inhibit (red text) or activate (green text) each stage. (Figure © 2022 Jennifer Stone,all rights reserved)

CHAPTER 3: DATA-DRIVEN 3D SHAPE ANALYSIS REVEALS CELL SHAPE-FATE RELATIONSHIPS IN ZEBRAFISH LATERAL LINE NEUROMASTS

The contents of this chapter will be submitted for publication with the following authors:

Madeleine N. Hewitt: Conceptualization, methodology, software, formal analysis, investigation, resources, data curation, writing – original draft, writing – review & editing, visualization, funding acquisition

Iván A. Cruz: Resources

David W. Raible: Conceptualization, formal analysis, writing – original draft, writing – review & editing, supervision, project administration, funding acquisition

3.0 Abstract

Cell shape is a powerful readout of cell state, fate, and function. With the advent of sophisticated microscopes, image segmentation algorithms, and numerical shape representations, it is becoming more feasible to study cell shape in developing tissues. However, few studies have analyzed cell shape in three dimensions in living, intact organisms. Here, we took advantage of the favorable imaging qualities of zebrafish lateral line neuromasts to generate a dataset of high resolution images with labeled cells and nuclei. Using a custom Python-based workflow, we performed semi-automated, 3D cell and nucleus segmentation. We then used spherical harmonics and principal components analysis to distill neuromast cell and nuclear shape variation into several intepretable, biologically meaningful parameters. We found that neuromast cell and nuclear shapes vary with cell location and identity. The distinction between hair cells and support cells was discrete and accounted for much of the variation in neuromast cell and nucleus shape, which allowed us to train classifiers to predict hair cell

identity from cell and nucleus shape features. Using markers for support cell subpopulations, we found that support cell subtypes also had different shapes from each other; however, shape features did not distinguish as sharply between support cell subtypes, suggesting that support cells vary continuously in shape. To investigate the effects of genetic perturbation that results in loss of a cell type on neuromast cell shape, we examined *atoh1a* mutants that lack hair cells. We found that neuromasts from *atoh1a* mutants lacked the cell shape phenotype associated with hair cells, but did not exhibit a mutant-specific cell shape. Our results demonstrate the utility of using 3D cell shape features to characterize, compare, and classify cells in a living, developing organism.

3.1 Introduction

The shape of a cell emerges from a complex interplay between fate, function, and external forces (Chan et al. 2017). Quantifying cell shape during development has provided mechanistic insight into morphogenetic processes, such as germ-band extension in *Drosophila* (Butler et al. 2009; Sun et al. 2017). Modifying cell shape in culture can influence cell division and death (Chen et al. 1997), as well as differentiation (Watt et al. 1988; Kilian et al. 2010). However, most studies of cell shape *in vivo* have used descriptive features (such as volume and sphericity), which may not capture subtle or multifactorial variations in shape between cell types, especially in tissues with complex, 3D organization. More complete 2D shape representations have been used to study cell motility and migration in culture (Pincus and Theriot 2007; Keren et al. 2008), but these methods cannot be easily generalized to 3D shapes. To fully appreciate the diversity of cell shape states during development and understand the relationship between cell shape and fate, robust 3D cell shape analysis methods must be applied to living, developing organisms.

Recently, several 3D cell shape representations have shown promising results. One approach uses spherical harmonics, which are a set of periodic functions defined on the surface of a sphere that form an orthonormal basis, a mathematical property that allows coordinates to be efficiently described by independent vectors. In this approach, the surface of each cell is mapped to a sphere, and the spherical harmonics transform is used to generate a list of coefficients that describe the cell's shape (Ruan and Murphy 2019). Principal components analysis (PCA) can then be applied to reduce dimensionality and facilitate interpretation of cell shape variation within and between cell populations. This method was recently used to understand variation in cell and nuclear shape of induced pluripotent stem cells in culture (Viana et al. 2023). Spherical harmonics have also been used to describe organ shape trajectories in murine limb and heart development (Dalmasso et al. 2022), and have been used to describe 3D shapes in medical imaging (Gerig et al. 2001). A strength of this method is that it maintains enough information to accurately reconstruct 3D cell shapes, enabling sophisticated, data-driven analysis of cell shape. Such a method, which eschews the limitations of choosing descriptive features or relying on 2D projections, could provide deeper insights into the relationships between cell shape, fate specification, and developmental trajectories. Here we test the idea that we can use these coefficients to cluster and classify cell types.

The lateral line system of zebrafish is an ideal model for studying cell shape in a living, developing animal. The lateral line is a sensory system that detects changes in water flow. Organs of the lateral line, known as neuromasts, are small, tightly packed epithelial rosettes with apical-basal polarity, radially organized cell types, and mirror symmetry (López-Schier and Hudspeth 2006; Pinto-Teixeira et al. 2015). Mechanosensory hair cells are located in the center of the neuromast and surrounded by nonsensory, glia-like support cells. Support cells can be further divided into subpopulations based on their locations, gene expression patterns, and propensity to act as progenitors during regeneration (Lush et al. 2019; Thomas and Raible

2019). Known support cell subpopulations include peripheral cells (also known as mantle cells), dorsoventral cells, and anteroposterior cells, which can be identified in live animals using established knock-in lines (Thomas and Raible 2019). In addition, the superficial location and optical transparency of zebrafish larvae facilitate high resolution live imaging of neuromasts. Together with the aforementioned knock-in lines, this model system enables interrogation of the relationship between cell shape, location, and fate in neuromasts.

In this study, we developed a workflow to segment neuromast cells and nuclei and analyze their 3D shapes using spherical harmonics and PCA. We were able to model cell and nucleus shape using just 8 cell shape and 4 nucleus shape principal components (PCs). We found that hair cells were clearly distinct from support cells in our shape space, while support cells appeared to vary continuously in shape. Unsupervised clustering in cell shape PC space revealed that markers for support cell subpopulations were enriched within certain clusters, suggesting these cell types have distinct cell shape features. Analysis of mutants in *atoh1a*, encoding a conserved transcription factor necessary for hair cell differentiation (Bermingham et al. 1999; Millimaki et al. 2007), revealed the loss of the hair cell shape phenotype and expansion of other cell shape phenotypes. We also successfully built classifiers to predict hair cell identity from cell and nucleus shape features. Our work demonstrates that cell shape parameters can be used to characterize and classify cell types in neuromasts, laying the foundation for future studies of form, fate, and function in sensory epithelia.

3.2 Results

3.2.1 A Semi-automated Workflow Accurately Segments Zebrafish Lateral Line Cells and Nuclei

Neuromasts are small, epithelial organs with tightly packed, apically constricted cells; this structure presents challenges for imaging and segmentation (Figure 3.1A). For all experiments, we used the zebrafish *Tg(cldnb:LY-EGFP)* transgenic line that labels neuromast cell membranes (Haas and Gilmour 2006). In addition, some zebrafish contained a knock-in allele that labeled a cell population of interest. We used fish heterozygous for *sost*^{w215Tg} or *sfrp1a*^{w217Tg} (henceforth referred to as *sost:NLS-Eos* and *sfrp1a:NLS-Eos*), which express NLS-Eos in dorsoventral support cells and peripheral support cells, respectively, and have no effect on neuromast development (Thomas and Raible 2019). Some zebrafish also contained one or two copies of *atoh1a*^{w271Tg} , a targeted insertion of mRuby into the *atoh1a* locus that when homozygous results in loss of *atoh1a* function and loss of hair cells. For the rest of this paper, we refer to this knock-in line as *atoh1a:mRuby* and indicate whether heterozygous or mutant animals are being described. Additional analyses of these lines are described in later sections. For numbers of neuromasts and cells from each line, refer to Table 1. All fish were stained with the far-red nuclear dye DRAQ5 (Smith et al. 1999). To achieve sufficient spatial resolution, we used a confocal microscope equipped with AiryScan (Huff 2015). Fish were imaged live at 5 days post fertilization (dpf), at which point neuromasts are functionally mature. Minimal cell death was observed during imaging; any neuromasts exhibiting significant amounts of cell death were excluded from further analysis.

Due to the tight packing of neuromast cells and variations in GFP signal intensity, classical thresholding-based segmentation approaches did not yield accurate results for cells or nuclei in our images. To improve the accuracy of segmentation, we trained machine learning models to detect cell boundaries from the membrane GFP signal and nuclei masks from the DRAQ5 signal using the Allen Cell and Structure Segmenter (Chen et al. 2018). We then used the model results as the foundation for watershed-based instance segmentation. In essence, the watershed transform treats the image as a topographical map and identifies “catchment basins”

as separate objects (Beucher and Lantuéjoul 1979). We first applied a distance transform watershed algorithm to segment every nucleus. Labeled nuclei were then used as seeds for marker-based watershed of membrane boundary predictions. The accuracy of segmentation was further improved through proofreading and manual correction. This semi-automated workflow produced good quality segmentations for most cells (Figure 3.1A). After segmentation, each field of view was manually inspected, and some cells were excluded for quality control (e.g. due to having poor signal or extending beyond the edge of the field of view). 164 cells were manually excluded in this way. In total, 3274 cells from 49 different neuromasts across 6 different imaging sessions were segmented.

3.2.2 Spherical Harmonics Accurately Represent Most Neuromast Cell Shapes

To quantitatively compare cell shapes, a list of numerical shape features must be extracted from each segmented cell in our dataset. In other words, the shape of each cell must be encoded as a vector. To approach this problem in an unbiased, data-driven fashion and maximize the amount of 3D shape information extracted from each cell, we used a method based on spherical harmonics expansion (SHE) (Ruan and Murphy 2019; Viana et al. 2023). In this method, the shape of the cell is mapped to the surface of a sphere, and the spherical harmonics transform is applied. The result is a vector of coefficients that describe the shape of the cell (organized into a cell-by-SHE-coefficients table), on which the inverse transform can be applied to create a reconstruction of the cell (Figure 3.1D).

One challenging aspect of this approach is that it is sensitive to the cell orientation – i.e., two cells with essentially the same shape that are rotated relative to each other will have different values of SHE coefficients. If differences in shape (rather than rotation) are of interest, then the cells must first be aligned to minimize rotational variation. We identified three sources of rotational variation in our dataset: (1) the radial symmetry of neuromast cells around the

apical-basal axis of the rosette, (2) differential tilt of the cell along the radial axis as cells come together at the apical end of the rosette, and (3) the fact that some samples were slightly tilted during image acquisition such that the imaging z-axis was slightly off-parallel to the neuromast apical-basal axis. To correct for (1), cells were rotated around the imaging z-axis such that vectors pointing from the cell centroids to the neuromast centroid were aligned to the x-axis (and thus to each other). To correct for (2) and (3), two additional rotations were applied. The first aligned the long axis of the cell in the xz-plane to the z-axis. The second aligned the long axis of the cell in the yz-plane to the z-axis, with one caveat: if the rotation required would be more than 45 degrees, the long axis in the yz-plane was aligned to the y-axis instead. This adjustment in rotation angle accounts for the fact that some cells in the dataset were longer along the y-axis than the z-axis, and we wished to preserve their apical-basal orientation. An example of a cell aligned by this procedure is shown in Figure 3.1B,C.

Following alignment, we applied SHE to our dataset, generating 2178 spherical harmonics coefficients for each cell (Figure 3.1D). As a measure of reconstruction fidelity, we used the directed Hausdorff distance, a metric often used in image processing that is reflective of the largest error between the original and its reconstruction (Huttenlocher et al. 1993). We found a bimodal distribution of error, with 84% of cells accurately reconstructed (Supplemental Figure 3.9A). Cells that were not accurately reconstructed tended to be located midway between the center and periphery of the neuromast (Supplemental Figure 3.9B) and had shapes that rendered them unsuitable for spherical harmonics expansion, such as high concavity (Supplemental Figure 3.9C). Cells with high reconstruction error (421 cells, representing 16% of the original dataset) were excluded from further cell shape analysis. To further understand the types of shapes that were excluded, we measured additional properties of excluded cells. Compared to other cells, excluded cells tended to have greater cell surface area and height (Supplemental Figure 3.9D, top). Nuclei of excluded cells had similar dimensions to those of

retained cells (Supplemental Figure 3.9D, bottom). In sum, some tall, curved cells located in a ring around the middle of the neuromast were not reconstructed well by spherical harmonics, and the shapes of these cells were not used in our subsequent analysis.

3.2.3 Principal Components Analysis Reveals Variations in Cell Shape Between Neuromast Cell Types

To identify, visualize, and interpret the main axes of shape variation in the dataset, we applied principal components analysis (PCA) to the cell-by-SHE-coefficients matrix. The 2178 SHE coefficients were reduced to 8 principal components (PCs) representing approximately 70% of the total variance in cell shape (Supplemental Figure 3.10). A key advantage of this approach is that from any point in this 8-dimensional shape space, it is possible to calculate the corresponding SHE coefficients and create 3D representations of real or theoretical cells. Reconstructing cells in this way would not be possible if using a list of geometric features to describe cell shape.

Neuromasts contain several cell types with qualitatively different shapes. For example, lateral line hair cells have a round, flask-like morphology, while many support cells are concave in shape or have thin apical projections. We wondered whether these different morphologies would be reflected in our shape space, and if so, whether variation in shape between cell types would be continuous (indicating smooth transitions between different shapes) or discrete (suggesting some populations have features that set them more clearly apart from other cells). To visualize shape variation, each PC was first individually z-scored (i.e. the values of each PC were divided by that PC's standard deviation) to generate "shape modes." We used the point corresponding to the origin in shape space (where the value of all 8 cell shape modes is 0) to create a visual representation of the mean cell shape in the dataset. We then varied the value of one shape mode while keeping the values of the other shape modes constant to generate visual

representations of each shape mode (Figure 3.2A). To compare the relationship between cell shape and position across neuromasts, we calculated the relative location of each cell using its radial distance and angular position (Figure 3.2B). A small number of interpretable parameters therefore captured the majority of cell shape variation, enabling quantitative comparisons of cell shapes within the dataset.

We hypothesized that hair cells, which can be identified by eye based on shape, would be quantitatively distinct from other cells using our shape analysis method. To test this hypothesis, we manually annotated hair cells in our dataset using the presence of apical stereocilia, which are visible in the *Tg(cldnb:LY-EGFP)* transgenic line. We found that cell shape mode 1 (CSM1, representing 27% of total variance) appeared to represent "hair cell-ness." Positive CSM1 scores corresponded with greater cell volume and width (Supplemental Figure 3.11B), as well as a more convex, flask-like shape (Figure 3.2C). Cells with positive CSM1 scores also tended to be closer to the neuromast center (Figure 3.2D, Supplemental Figure 3.11D), consistent with the characteristic location of hair cells. This result suggests that much of cell shape variation in neuromasts is due to differences between hair cells and support cells.

In contrast to CSM1, cell shape mode 2 (CSM2, representing 16% of total variance) did not distinguish between hair cells and support cells; rather it appeared to distinguish among support cell types. Cells with increasing CSM2 scores were progressively taller and less deep (Figure 3.2E, Supplemental Figure 3.11B). CSM2 was also negatively associated with being located toward the neuromast periphery, particularly for support cells (Figure 3.2F, Supplemental Figure 3.11D). Hair cells tended to have average CSM2 scores, clustered around zero, and showed a narrower distribution than support cells (Supplemental Figure 3.11C). Taken together, the relationships between cell type and cell position likely explain the "bullseye" pattern observed when CSM2 scores are plotted by relative cell location: support cells have higher CSM2 scores as they become more central, while hair cells (which are also centrally

located) have CSM2 scores close to zero (Figure 3.2F).These observations suggest that CSM2 represents shape variation between support cells in a way that is distinct from the variation between support cells and hair cells.

To facilitate interpretation of shape modes and further query the relationships between shape modes and cell type, we compared shape modes to geometric features and location parameters (Supplemental Figure 3.11). We correlated CSM1 and CSM2 to cell width, depth, height, volume, surface area and cell distance from the neuromast center (Supplemental Figure 3.11B,D). We found a positive correlation between CSM1 and cell volume and cell width, and a negative correlation with distance from the center of the neuromast. For CSM2, there was a positive correlation with cell height and a negative correlation with cell depth and distance from center. Hair cells consistently segregated with CSM1 but not CSM2 (Supplemental Figure 3.11C,D). Beyond CSM1 and CSM2, other shape modes appeared to represent more subtle ways in which neuromast cell shape varied (Supplemental Figure 3.10).

3.2.4 Nuclear Shape Variation Is Captured by SHE and PCA

We also performed SHE and PCA on nucleus shape. Nuclei were aligned to account for position within the neuromast using a series of rotations similar to (but independent of) that used to align cells (see Methods for details). Because nuclei had a much lower reconstruction error compared to cells (Supplemental Figure 3.9A), we elected not to exclude any nuclei from analysis and maintained the original dataset of 3274 cells to see whether additional insights about these cells could be gained from nuclear shape analysis. Nuclear SHE coefficients were reduced to 4 principal components (PCs) representing approximately 76% of the total variance in nuclear shape (Supplemental Figure 3.12). As for cell shape analysis, nuclear shape PCs were z-scored to describe them as nuclear shape modes.

Nucleus shape mode 1 (NSM1, representing 40% of total variance, Figure 3.3A) and nucleus shape mode 2 (NSM2, representing 18% of total variance, Figure 3.3C) captured distinct aspects of variation in nuclear shape. Increasing NSM1 scores were associated with a shift from short, wide shapes to a tall, crescent-like morphology (Figure 3.3A). Meanwhile, NSM2 appeared to describe a progression from tall and cylindrical to flattened, rectangular shapes (Figure 3.3C). Nucleus shape modes 3 and 4 are summarized in Supplemental Figure 3.12. Comparing to other nuclear shape parameters (Supplemental Figure 3.13), we found NSM1 was negatively correlated with nucleus width and positively correlated with nucleus height (Supplemental Figure 3.13B,D). NSM2 was positively correlated with nucleus depth and negatively correlated with nucleus volume (Supplemental Figure 3.13B,D).

We next asked to what degree nuclear shape modes distinguished among hair cells and support cells. We found that NSM1 had a bimodal distribution (Supplemental Figure 3.13C) and was correlated with distance from the neuromast center (Figure 3.3B, Supplemental Figure 3.13D). Like CSM1, NSM1 also appeared to distinguish between hair cells and support cells, but to a lesser degree since some support cells also had high NSM1 scores (Supplemental Figure 3.13C). NSM2 also showed a slightly skewed distribution and a correlation with distance to the neuromast center (Figure 3.3D, Supplemental Figure 3.13D), with some distinction between hair cells and support cells. Nuclear shape modes therefore also captured variation between hair cells and support cells, although this information was split across multiple shape modes.

3.2.5 Unsupervised Clustering of Neuromast Cells in Shape Space Identifies Groups of Cells With Similar Shapes and Locations

We next wanted to determine whether shape features could be used to assign neuromast cells to biologically meaningful categories beyond hair cells and support cells. To do so, we performed unsupervised clustering on the first 8 cell shape PCs using the Phenograph package

with the Leiden community detection algorithm (Levine et al. 2015; Traag et al. 2019). Five clusters were identified and represented in two dimensions by a uniform manifold approximation and projection (UMAP, Figure 3.4A) (McInnes et al. 2018) where each cell is a point colored by cluster label. The fraction of cells within each cluster was proportional across all individual neuromasts (Supplemental Figure 3.15D) suggesting that clustering is influenced by shared shape parameters and not due to differences between neuromasts. To quantify the relationships between clusters, we performed partition-based graph abstraction (PAGA) as a way to quantify similarities between assigned clusters (Wolf et al. 2019). Relative strength of association is represented by line thickness (Figure 3.4B). PAGA analysis revealed relatively greater similarities between clusters 0/2, 1/2/3, and 2/4. To visualize the characteristic shapes of cells within each cluster and facilitate comparisons between them, we identified the cell closest to the centroid of each cluster in eight-dimensional PC space as a "representative cell" (Figure 3.4C). Cells in clusters 0 tended to be shorter with greater depth, while cells in cluster 3 tended to be tall and wide. Cells in clusters 1 and 2 appeared to have shapes intermediate between clusters 0 and 3. Meanwhile, cells in cluster 4 tended to have flask shapes reminiscent of hair cells; quantifying manually annotated hair cells in each cluster confirmed that most hair cells were assigned to cluster 4 (Supplemental Figure 3.15E) and cluster 4 was primarily composed of hair cells (Supplemental Figure 3.15F).

Cells from a given cluster tended to be found in similar locations across neuromasts in the dataset. In particular, cells in specific clusters were found at distinct radial distances from the neuromast center (Figure 3.4D,E), and we used this order to assign cluster number labels. However, we also found that some clusters were distributed in distinct quadrants of the neuromast (Figure 3.4D,F). This difference in distribution was particularly apparent for cluster 1, where cells were more concentrated within the dorsal-ventral quadrants of the neuromast, and cluster 2, where cells were more often found within the anterior-posterior quadrants. These

results suggest that grouping neuromast cells purely using shape descriptors, without explicitly including information about cell type or identity, recapitulates known aspects of neuromast organization (e.g. concentric and radially symmetric cell populations).

We also performed unsupervised clustering on the first 4 nucleus shape PCs. Similar to cell shape clusters, we found distinct nucleus shape clusters (Figure 3.5A) whose relative relationships could be measured through PAGA analysis (Figure 3.5B). As for cells, we identified representative nuclei for each cluster (Figure 3.5C). Clusters 4 and 5 were primarily composed of hair cells, and cluster 1 was enriched for dorsal-ventral cells (Figure 3.5D). Nucleus shape clusters exhibited distinct spatial locations within the neuromast (Figure 3.5D,E,F). However, nucleus shape clusters did not appear to distinguish as well between support cell subpopulations compared to cell shape clusters. Since the nucleus shape dataset contains cells that were excluded from cell shape analysis, we looked at the distribution of excluded cells across nucleus shape clusters (as a way to understand whether a particular class of cells had been excluded). We found excluded cells in all 5 nucleus shape clusters, suggesting that excluded cells can have a range of nucleus shape phenotypes (Supplemental Figure 3.9E). Based on these results, we decided to perform the remaining analysis using only cell shape clusters.

3.2.6 Cell Fate Markers of Support Cell Subpopulations Are Associated With Distinct Cell Shape Phenotypes

Clustering purely based on shape descriptors yielded groups with distinct spatial patterns in neuromasts resembling those of previously known support cell types. For example, peripheral support cells (mantle cells) form a ring around the outside of the neuromast. Distinct support cell subpopulations also exist within the dorsoventral (DV) and anteroposterior (AP) compartments of the neuromast. These support cell subpopulations have characteristic transcriptional profiles and behaviors during regeneration (Lush et al. 2019; Thomas and Raible

2019): DV cells act as hair cell progenitors while peripheral cells can replenish DV cells depleted by hair cell differentiation. We hypothesized that if cell shape clusters correspond to cells with distinct identities, they would be enriched for markers of these support cell subpopulations.

To examine the relationship between support cell identity and cell shape, we examined neuromasts from knock-in lines that mark distinct support cell subpopulations. The numbers of neuromasts and cells analyzed for each line are summarized in Table 1. The *sost:NLS-Eos* line marks cells in the DV compartment of the neuromast (Figure 3.6A-C, Supplemental Figure 3.14A,B). We measured the mean intensities of Eos fluorescence in each cell, normalizing to z-score for each individual neuromast. We then classified cells as Eos+ if they had fluorescence with z-score greater than 1 (Figure 3.6B, Supplemental Figure 3.14C). An example neuromast with labeled positive cells is shown in Figure 3.6B. As expected, *sost:NLS-Eos*+ cells were found in DV quadrants (Figure 3.6B,C). We next asked whether *sost:NLS-Eos*+ cells were differentially distributed across clusters (Figure 3.6E,F). Most *sost:NLS-Eos*+ cells were found in cluster 1 (Figure 3.6E). 33% of cluster 1 cells were s*ost:NLS-Eos*+, the highest proportion of any cluster (Figure 3.6F). A small number of *sost:NLS-Eos*+ cells were also found in clusters 2 and 3,making up 13% and 17% of clusters 2 and 3, respectively (Figure 3.6F). These results indicate that DV support cells, as measured by *sost:NLS-Eos* expression, occupy a subset of possible cell shape states within neuromast cells.

The *sfrp1a:NLS-Eos* line marks peripheral support cells (Figure 3.6G-I). We again measured the mean intensities of Eos fluorescence in each cell, normalizing to z-score (Supplemental Figure 3.14D-F), and classified cells as Eos+ with fluorescence with z-score greater than 1 (Figure 3.6H, Supplemental Figure 3.14F). Cells expressing higher levels of Eos were found in the neuromast periphery (Figure 3.6H,I; Supplemental Figure 3.14D,E). Most *sfrp1a:NLS-Eos*+ cells were found within cluster 0, making up about half of the cells in this cluster (Figure 3.6K,L). Some *sfrp1a:NLS-Eos*+ cells were also found in clusters 1 and 3, making

up 13% and 29% of clusters 1 and 3, respectively. As with DV support cells, peripheral support cells tended to inhabit a smaller range of shapes within the neuromast cell shape space. Overall, there was no difference in the distribution of clusters among individual neuromasts across wildtype, *sost:NLS-Eos*, and *sfrp1a:NLS-Eos* lines (Supplemental Figure 3.15A). Taken together, these results demonstrate that cells with distinct identities, as indicated by *sost:NLS-Eos* and *sfrp1a:NLS-Eos* expression, can be recognized by distinct cell shape characteristics.

3.2.7 *atoh1a* Mutants Exhibit Changes in Cell Shape Across Cell Populations

We next sought to test what happens to cell shape distributions when a single cell type is absent. The transcription factor *atoh1a* is required for hair cell fate specification in zebrafish lateral line neuromasts (Itoh and Chitnis 2001; Millimaki et al. 2007). We expected that the loss of the hair cell shape phenotype would be readily observable in *atoh1a* mutants. However, we wondered whether support cells would maintain the same shapes seen in wildtype fish or if their shapes would also be altered in *atoh1a* mutants. In the *atoh1a:mRuby* line, the mRuby fluorophore was inserted into the coding sequence of the *atoh1a* gene, disrupting its function but acting as a readout for *atoh1a* promoter activity. This knock-in line enables comparisons not only between wildtype, mutant, and heterozygous cell populations as a whole, but also between mRuby+ and mRuby- populations in each genotype.

In heterozygous fish, mRuby+ cells are localized to the center of the neuromast (Figure 3.7A; Supplemental Figure 3.15B). We measured the mean intensities of mRuby fluorescence in each cell, normalizing to z-score, and classified cells as mRuby+ if they had fluorescence with z-score greater than 1 (Figure 3.7B, Supplemental Figure 3.14G-I). Overall, the proportions of cells in each cluster were similar to those of wildtype fish (Supplemental Figure 3.15A,D). However, mRuby+ cells were differentially proportioned across clusters (Figure 3.7C,D). We found that mRuby+ cells were highly enriched in cluster 4 (Figure 3.7D). We confirmed that cluster 4

represented hair cells by examining the distribution of manually annotated hair cells in our dataset identified by the presence of apical stereocilia (Supplemental Figure 3.15E,F).

In homozygous mutant fish, mRuby+ cells were still found in the center of the neuromast even though they did not differentiate into hair cells (Figure 3.7E, Supplemental Figure 3.15B). There was not a statistically significant difference in the proportion of mRuby+ cells between heterozygous and homozygous animals ($X^2 = 1.8$, df = 1, p = 0.18; Supplemental Figure 3.15C). Like in heterozygotes, mRuby+ cells in homozygotes were differentially distributed across clusters (Figure 3.7G,H; Supplemental Figure 3.15A,D). Relative to wildtype and heterozygotes, mutant fish had far fewer cells in cluster 4 and an increased proportion in cluster 2 (Figure 3.7H; Supplemental Figure 3.15A,D). In heterozygotes, 84% of mRuby+ cells were found in cluster 4 (Figure 3.7D), but only 33% of mRuby+ cells were assigned to cluster 4 in mutants (Figure 3.7H). By contrast, the number of mRuby+ cells in clusters 2 and 3 were expanded in mutants. For mRuby- cells, cluster 2 was expanded in mutants relative to heterozygotes (Figure 3.7D,H). These results suggest that loss of *atoh1a* function is associated with a loss of the hair cell shape phenotype, an effect mainly seen in mRuby+ cells, and a concurrent shift in support cell shapes towards a greater number of cluster 2 phenotypes. The loss of hair cells did not result in the appearance of a new cell shape cluster but rather a redistribution of cells into existing shape clusters. These results demonstrate that cell shape analysis can be used to query changes in phenotype in contexts where development has been perturbed. Additionally, these results show that some aspects of cell shape are genetically determined in our system, rather than being solely due to other factors (such as position within the neuromast).

3.2.8 Shape Modes Can Be Used to Classify Hair Cells

Our results thus far have suggested that hair cells have distinct cell shape phenotype compared to support cells. Previously, we observed that CSM1 scores appear to represent "hair cell-ness" (Figure 3.2C). A histogram of CSM1 scores exhibited a bimodal distribution with a positive and negative peak (Figure 3.2C), unlike the other shape modes that centered around zero (Supplemental Figure 3.10A). Comparing manually annotated hair cells to support cells, we found that hair cells tended to have positive CSM1 scores and comprised the majority of the positive peak in the shape mode histogram (Supplemental Figure 3.11C). To confirm this association, we examined the distribution of CSM1 scores of cells from *atoh1a* heterozygous and mutant fish. We found that the distribution of CSM1 scores in heterozygotes resembled that of wildtype fish, with hair cells associated with positive scores (Figure 3.8A, top and middle). By contrast, the distribution of CSM1 scores in homozygous mutants was no longer bimodal (Figure 3.8A, bottom) and was skewed negative and corresponded to the distribution of support cells in wildtype and heterozygous animals. CSM1 therefore captured the variation in shape between the two broadly defined neuromast cell populations (hair cells and support cells) and was predictably perturbed in mutants lacking hair cells.

The distinction between hair cells and support cells in CSM1 scores suggested that cell shape modes may contain sufficient information to classify cells as belonging to either of these cell types. We trained a logistic regression classifier to predict hair cell identity given the first eight cell shape mode scores (CSM1-8). The Receiver Operating Characteristic (ROC) curve indicated robust classifier performance with Area Under the Curve (AUC) of 0.96 (Figure 3.8B). Despite the imbalance of classes in the dataset (77% support cells and 23% hair cells), the classifier correctly labeled most (78%, 100/128) of the hair cells in the test set, while few support cells (5%, 22/422) were incorrectly labeled as hair cells (Figure 3.8C). We also asked if hair cells could be classified using nucleus shape features. We trained a logistic regression classifier using the first four nucleus shape modes (NSM1-4). Our classifier based on nucleus shape features

performed similarly well to one using cell shape features (AUC score = .0.96; data not shown). Therefore, nuclear shape features can also be used to classify hair cells from support cells.

To visualize the shape characteristics associated with hair cell identity, we created a 3D reconstruction of the idealized mean hair cell in the dataset by calculating the mean CSM1-8 scores for hair cells and deriving the corresponding SHE coefficients (Figure 3.8D). As expected, the "average" hair cell has a flask-like morphology. These results demonstrate the utility of cell shape features both for describing and classifying cell types.

3.3 Discussion

During development and regeneration, cells transition through states as they grow, divide, and differentiate. Measuring the transcription of genes has proven to be a powerful method for understanding and classifying cell types. Using single cell RNA-sequencing, thousands of transcripts can be sequenced for each cell, generating high-dimensional data for cell type annotation and classification. However, cells can change in ways that are not necessarily reflected in RNA transcript levels (Marklein et al. 2016; Gerbin et al. 2021). Cell shape analysis offers another avenue to quantitatively characterize and classify cells. Methods to encode cell shape in an unbiased, high dimensional representation have been employed with great success to cells in culture (Pincus and Theriot 2007; Keren et al. 2008; Viana et al. 2023). However, to our knowledge, most studies of cell shape in living, developing animals have relied on 2D projections of cells or representative 3D geometric features, which may not capture many aspects of cell shape in these tissues. In this study, we use spherical harmonics and PCA to encode cell shape information in a more complete, unbiased fashion, allowing for data-driven analysis of the relationships between cell shape and fate.

A primary goal of our study was to understand the relationship between cell shape and established indicators of cell identity in neuromasts. If cell shape and markers for neuromast

cell fate were tightly correlated, then it might be possible to classify cell types using shape features. Our results suggest that this relationship was true of hair cells, since we were able to build a logistic classifier for hair cells using our shape modes. In addition, when we performed unsupervised clustering of cells in shape space, there was a high degree of overlap between hair cell identity and one of the clusters (hair cells comprised 79% of cluster 4). Few hair cells were found in the other four clusters. In sum, using 3D cell shape analysis, we quantitatively captured differences between two broad classes of cells in our dataset. We believe a similar method could be used to build classifiers for cell types in other developmental contexts, potentially allowing for cell fate to be predicted from image-based data without expression of cell fate markers.

The association between cell shape and support cell subtypes was more nuanced. In our clustering analysis, DV cells defined by *sost:NLS-Eos* were primarily observed in cluster 1 and rarely seen in the remaining four clusters. A similar pattern was observed with peripheral cells defined by *sfrp1a:NLS-Eos*, which were usually observed in cluster 0. However, while each marker was specific to certain clusters, these clusters also contained substantial proportions of cells not expressing the marker. This result may indicate that DV and peripheral support cells have a shape phenotype distinct from each other, but only comprise a subset of cells with that shape phenotype. Given that support cells act as multipotent progenitors (Romero-Carvajal et al. 2015; Viader-Llargués et al. 2018; Thomas and Raible 2019), we speculate that perhaps the more continuous distribution of support cell shapes may reflect this plasticity and smoother transitions between cell states. In contrast, hair cells are a terminally differentiated cell type, which may be represented in their more distinct cell shape phenotype. A caveat is that our cutoff for considering a cell positive for a marker was relatively strict. In addition, our transgenic reporters may not always reflect the cells most recently expressing the transgene due to the time it takes for fluorescent proteins to be expressed and folded and the high stability of the NLS-Eos protein (Cruz et al. 2015). Future studies using other methods to label support cell

subpopulations with genetic markers, such as RNA-FISH, could further elucidate the connection between gene expression and cell shape in neuromasts. More broadly, cell shape analysis could be integrated with other cellular properties, such as RNA transcript expression, protein expression and organelle location.

We were also interested to see whether nuclear shape could be used to classify cell types. Because the nucleus is often easier to label and segment, nuclear shape representations may be more readily attainable in some developmental biology contexts. We found that nuclear shape could also be used to reliably classify hair cells from support cells. However, compared to cell shape features, nuclear shape features did not appear to distinguish as strongly between the support cell subpopulations we tested in this study. This may suggest that cell shape features are more useful for classifying these populations than nuclear shape features. However, nucleus shape may still be informative in other ways – we observed spatial patterns in nuclear shape within neuromasts, which may represent differences in cell type or state that were not tested in this study. Analysis of nucleus shape may also be more amenable to other tissues where cell membranes may not be easily resolved, allow more rapid collections of larger datasets, or allow analysis of cell types whose cell shapes are not amenable to spherical harmonics analysis. More broadly, we imagine that cell shape, nuclear shape, or a combination of the two may be useful as predictors of cell fate in different tissues.

In many developmental contexts, it remains unclear how genetic factors determine cell shape. We tested whether the gene *atoh1a* regulates cell shape by performing cell shape analysis in *atoh1a* muants. Our results suggest that while *atoh1a* is required for neuromast cells to acquire the hair cell shape phenotype, it may be dispensable for other aspects of neuromast cell shape and organization. We observed that loss of function in *atoh1a* results in the large reduction of one cluster (cluster 4, associated with hair cells) and concurrent increases in existing clusters, but does not lead to generation of a new shape cluster. Therefore, it appears

that *atoh1a* is required for the transition from a support cell shape to a hair cell shape; when *atoh1a* function is lost, cells become arrested in shapes that exist in wildtype neuromasts rather than acquiring an *atoh1a* mutant-specific shape phenotype. Similarly, during an RNAi screen for morphological complexity in *Drosophila* Kc cells, RNAi knockdown typically did not generate new shapes but instead changed distributions of pre-existing, wildtype shape states (Yin et al. 2013). It would be illuminating to explore other genes and signaling pathways that may pattern cell shape within neuromasts. For example, Fgf signaling has been shown to be required for apical constriction and rosette formation in the lateral line primordium (Harding and Nechiporuk 2012). It is possible that Fgf signaling could regulate aspects of neuromast cell shape independently of *atoh1a*. Applying cell shape analysis to query other genetic and pharmacological perturbations could elucidate how cell shape in neuromasts is regulated by different signaling pathways.

Previous work has proposed that hair cell death might induce cell shape changes and tissue deformations that trigger support cells to proliferate; this idea originates from observations that (1) mechanical strain and cellular spreading induce proliferation in some contexts (Watt et al. 1988; Chen et al. 1997; Benham-Pyle et al. 2015), and (2) support cell shape change during hair cell death is positively correlated with an organism's hair cell regeneration capability (Meyers and Corwin 2007; Burns et al. 2008, 2013; Burns and Corwin 2014). Mechanical cues and cell density might also act as a brake on proliferation during regeneration, similar to what has been observed during development in the murine utricle (Gnedeva et al. 2017). Quantifying cell shape change during hair cell death or targeted ablation of neuromast cells in the presence of reporters for genes of interest could elucidate the role of cell shape in regulating proliferation and regeneration. Of particular interest is Yap, a transcriptional coactivator that regulates cell proliferation downstream of cell adhesions, cell shape change, and mechanical cues (Piccolo et al. 2014). Yap is known to play a role in regulating proliferation

during development and regeneration of hair cells in the mammalian utricle and organ of Corti (Rudolf et al. 2020; Gnedeva et al. 2020; Kastan et al. 2021). Coupling cell shape analysis with reporters for Yap activity and subcellular localization could shed light on whether cell shape change acts upstream of Yap-induced cell proliferation. Cell shape analysis could also be combined with computational simulations and techniques to measure and perturb forces *in vivo* to relate changes in force with cell shape. Although relating cell shape change to physical forces was previously possible with simpler shape metrics, we anticipate that robust 3D cell shape representations will better detect subtle shape changes and be relevant to a greater variety of tissues than 2D methods.

Previously, Hartmann and colleagues (2020) analyzed 3D cell morphology in the migrating posterior lateral line primordium. Rather than using a spherical harmonics-based shape representation, this study employed a novel method (ISLA-CBE) based on point cloud morphometry. A strength of ISLA-CBE is that rotational variation can be minimized using a pairwise distance transformation, which is arguably less arbitrary than the method of registration used in our study (which tried to preserve biologically meaningful axes while minimizing rotational variation). In addition, ISLA-CBE is not limited to cells that can be accurately spherically parameterized, as ours was (although it is possible this limitation may be overcome with future implementations of spherical harmonics). However, ISLA-CBE does not easily allow cell shapes to be reconstructed from any point in feature space, which is an advantage of our method. We anticipate that both methods will be useful in the future, as the ideal method of cell shape encoding will likely depend on the context and goals of the study.

Although the method of encoding cell shape was different, we observed some commonalities between the results of our study and that of Hartmann and colleagues (2020). Our observations suggested that hair cells represent a discrete morphological state from support cells, while support cells appeared to vary more continuously in shape. Similarly, Hartmann and

colleagues (2020) observed a continuous spectrum of shapes, without distinct clusters, in the lateral line primordium. Together, these results suggest a model whereby initially, cells in the lateral line vary continuously in shape, but as hair cells differentiate, they emerge as a discrete shape. How early these patterns develop and whether they change over time or remain static during neuromast deposition and maturity, could be addressed in future studies.

Although our study looked only at homeostatic, mature neuromasts at one time point, we believe the cell shape representation used here could be valuable for integrating information across multiple spatial and temporal scales. Using time lapse imaging and cell tracking, it would be possible to study dynamic cell shape changes during hair cell development, death, and regeneration. We envision that cell shape states could be ordered along trajectories that represent developmental time, analogous to pseudotime analysis employed in single cell RNA sequencing studies (Andrews et al. 2021). In addition, shape analysis can be applied to understand the morphologies of whole tissues and organs (Dalmasso et al. 2022). Combining pseudotime analysis with tissue-scale measurements can elucidate the relationship between individual cell shape change and tissue/organ morphogenesis, as has been demonstrated in a study of notochord development in amphioxus (Andrews et al. 2021). Quantifying how these relationships evolve over time as the animal grows and develops could shed light into how individual cell shape changes and movements shape organs, as well as how, conversely, the shape of organs constrain individual cell shape. Comparative cell shape studies could also be done between different sensory epithelia in the same organism or even between different species or ages, which could inform evolutionary relationships.

Limitations of the Study

In the spherical harmonics-based approach used here, all points on the surface of the cell must be able to be mapped onto a sphere to generate accurate reconstructions. However, some

of our cells are sufficiently concave that this is not possible, since a line drawn from the center to the outside of the surface would intersect the surface more than once. As a result, 16% of the cells were excluded from further analysis, and some cell shape states may have been lost. Since this problem likely extends to other cell types beyond neuromasts, there is a need for other 3D cell shape analysis methods that can better represent complex, concave shapes. Development and application of alternative methods for spherical parameterization and spherical harmonics expansion offer one potential solution to this problem. For example, Dalmasso and colleagues (2022) represented cell shapes as signed distances from concentric spheres, which enabled them to represent concave structures of mouse limbs using spherical harmonics. Another method using 4D hyperspherical harmonics enables multiple disjointed objects to be parameterized together, and also enables representation of shapes with gaps or holes (Pasha Hosseinbor et al. 2015). There are also alternatives for data-driven 3D shape representations that are not based on spherical harmonics. Promising methods in this category include 3D point cloud morphometry-based methods like ISLA-CBE (Hartmann et al. 2020) and deep learning approaches such as autoencoders (De Vries et al. 2022). With the rate of exciting developments in the field, we expect that many methods will be available to study cell shape in a variety of contexts in the future.

3.4 Materials and Methods

Fish lines

The following zebrafish lines were used for these studies: *Tg(-8.0cldnb:LY-EGFP)*^{zf106Tg} (Haas and Gilmour 2006), *sost*^{w215Tg} (Thomas and Raible 2019), *sfrp1a*^{w217Tg} (Thomas and Raible 2019), *atoh1a*^{w271Tg} (this paper).

Generation of *atoh1a*^{w271Tg}

The *atoh1a*^{w271Tg} line was generated by CRISPR-Cas9 knock-in of the mRuby fluorophore into the coding sequence of the endogenous atoh1a locus, as previously published (Kimura et al. 2014; Thomas and Raible 2019). Homozygotes exhibit phenotypes consistent with atoh1a loss of function, such as hearing and vestibular defects, and are viable until approximately 10 dpf.

Fish handling

Experiments were conducted on five days post fertilization (5 dpf) larval zebrafish (*Danio rerio*). Prior to experiments, embryos and larvae were raised in E3 embryo medium (14.97 mM NaCl, 500 μM KCL, 42 μM Na_2HPO_4, 150 μM KH_2PO_4, 1 mM $CaCl_2$dehydrate, 1 mM $MgSO_4$, 0.714 mM $NaHCO_3$, pH 7.2) at 28.5°C. Zebrafish larvae were fed rotifers daily from 4 dpf onwards. Zebrafish experiments and husbandry followed standard protocols in accordance with University of Washington Institutional Animal Care and Use Committee guidelines.

DRAQ5 staining

On the day of imaging, DRAQ5 dye (Thermo-Fisher) was diluted in E3 embryo medium to a working concentration of 5 μM. 5 dpf larval zebrafish were incubated in this solution for approximately 1 hour, then prepared as described in "Preparation of larvae for live imaging." We observed best results when the fish were incubated in DRAQ5 no longer than 1 hour and immediately prepared for imaging afterward.

Photoconversion of NLS-Eos

For experiments done with *sost:NLS-Eos* or *sfrp1a:NLS-Eos* lines, larvae were photoconverted using an an iLumen 8 UV flashlight (purchased from Amazon) for 15-20

minutes. Photoconversion was done by placing fish in a 60 × 15 mm petri dish, removing the petri dish lid, and placing the UV flashlight directly over the dish within a box lined with aluminum foil.

Preparation of larvae for live imaging

Fish were transferred to E3 embryo medium containing approximately 1.5 mM MESAB to be anesthetized. Once larvae were suitably anesthetized, they were mounted on slides with bridged coverslips in 1.2% low melting point agarose. Fish were mounted in a standard orientation of anterior facing left and dorsal up.

Confocal imaging

Imaging was performed using a Zeiss LSM 880 with Airyscan equipped with a Zeiss C-Apochromat 40x/1.2W numerical water objective. Imaging was performed at room temperature (approximately 25°C). For each fish, several anterior neuromasts were imaged. Neuromasts were chosen from a list based on which had the most ideal orientations in the fish being imaged (e.g. those neuromasts closest to the coverslip with apical-basal axes roughly parallel to the axial plane/Z-axis of imaging). 633 nm, 561 nm, and 488 nm lasers were used for excitation. Gain was adjusted for different transgenes but kept constant across experiments with the same transgene. Images were collected with physical voxel size of 0.05 x 0.05 x 0.22 μm^3. All images were captured using the Zen Black acquisition software (Zeiss).

Image preprocessing

Using Zen Blue, Airyscan Processing was applied to all raw images using the default settings for pixel reassignment and deconvolution (Huff 2015). Next, a custom Python script using the aicsimageio package (Brown et al. 2021) was used to remove any unneeded channels

and export the CZI files to TIFFs. The original CZI files were kept to ensure access to the original acquisition metadata. To correct for xy drift between z-slices, StackReg was used, either through the MultiStackReg FIJI plugin or a custom script using the pystackreg Python port of StackReg (Thevenaz et al. 1998). Using the "rigid body" method and "previous" setting for the reference, transformation matrices were calculated for the membrane channel, saved, and applied to all channels in the image. Images were manually inspected following stack registration to ensure appropriate drift correction.

Occasionally, imaging acquisition errors or z drift caused either duplication of z slices within the stack or the need to acquire additional z-slices to cover the entire neuromast. In cases where this could be easily manually corrected, duplicated z-slices were deleted, or two z-stacks were concatenated together to cover the entire neuromast. These manual corrections were done using FIJI (Schindelin et al. 2012) prior to stack registration.

Training of machine learning models for detection of nuclei and membranes

Models to detect neuromast nuclei and membranes were trained using the iterative deep learning workflow of the Allen Cell and Structure Segmenter (Chen et al. 2018). For the membrane model, preliminary segmentations of cell boundaries were initially generated using the lamin B1 workflow from the Segmenter. The "Curator" tool from the Segmenter was used to mask out areas of the images that were not segmented accurately. The original membrane model was trained on a dataset of 14 neuromasts labeled with *Tg(-8.ocldnb:LY-EGFP)*. The membrane model predictions were thresholded and used as input for an interactive distance transform watershed segmentation workflow. Upon generating the label images, the find_boundaries function from scikit-image was used to generate watershed lines, which was used as input to train a second membrane model with improved performance. This process was repeated once more with a new dataset of 9 *Tg(-8.ocldnb:LY-EGFP)* neuromasts stained with DRAQ5, except

labeled nuclei were used to generate seeds for the watershed instead of the distance transform. The results were used to train the third membrane model, which was used for instance segmentation (delineation of individual objects) of all the images in this study.

To generate the nucleus mask model, the "H2B coarse" model provided by the AICS was used to generate preliminary nucleus predictions. The predictions were thresholded, and the membrane intensity image (or membrane boundary predictions) were used to "split" the nuclei (as described in "Instance segmentation"). Similar to the refinement for the membrane model, a distance transform watershed workflow was applied to thresholded nuclei predictions to generate labeled nuclei, which were converted to binary masks and used to train the first nucleus mask model. This process was repeated (starting from the model 1 predictions instead of the H2B coarse model predictions) to generate a second nucleus mask model with improved performance, which was used for all the images in this study.

Instance segmentation

Instance segmentation of nuclei was done in a semi-automated, interactive fashion using a custom Python script. The Python packages napari (Sofroniew et al. 2022) and magicgui (Lambert et al. 2023) were used to create a graphical user interface for this step, enabling parameter tuning, interactivity, and manual annotations when needed (Sofroniew et al. 2022).

First, the nucleus mask predictions and cell boundary predictions were binarized using thresholds of 0.6 and 0.4, respectively. These thresholds were selected a balance between capturing intensity signal corresponding to the structures of interest and minimizing artifacts due to noise. The binarized membrane predictions were used to "split" falsely merged nuclei in the binarized nucleus mask predictions, using one of two methods. For experiments not involving nlsEos transgenes, the nucleus mask splitting was done fully automatically (e.g. wherever the membrane mask value was 1, the corresponding pixels in the nucleus mask were

set to 0). For experiments involving NLS-Eos transgenes, incomplete photoconversion and/or ongoing transgene expression can cause some signal in the nuclei in the green channel, where the membranes are also imaged. This overlap can create artifacts when the cell boundary model is applied. To circumvent the issue, an alternative "interactive" nucleus splitting strategy was devised. For interactive nucleus splitting, regions of interest (ROIs) were manually drawn slice-by-slice in areas where splitting was desired using the shapes tool in napari. Then, only these regions within the membrane mask were considered during the splitting process.

Following nucleus splitting, individual nuclei were labeled using distance transform watershed. First, the Euclidean distance transform of the nucleus mask was calculated and smoothed using a Gaussian kernel. Next, the local maxima of the smoothed distance transform were calculated using the peak_local_max function from scikit-image (van der Walt et al. 2014). The local maxima were then used as markers for a watershed segmentation using the inverted distance transform as the input. The sigma parameter for the Gaussian smoothing of the distance transform and the minimum distance parameter for the peak_local_max function were adjusted interactively to yield the best results for each image. Remaining segmentation errors were corrected by manual annotation using a Wacom Cintiq 16 drawing tablet and built-in labels layer tools in napari (Sofroniew et al. 2022).

To segment cells, the segmented nuclei were used as markers for a watershed segmentation with the cell boundary predictions (i.e. the raw, unthresholded output of the membrane model inference) as input. The resulting preliminary cell labels were post-processed to remove small objects and manually corrected using a Wacom Cintiq 16 drawing tablet and built-in labels layer tools in napari (Sofroniew et al. 2022).

Cell dataset preparation

Prior to running the cell variance analysis pipeline (Viana et al. 2023), individual cells from the raw and labeled whole neuromast images were cropped, subsampled in z to obtain isotropic voxel size, and saved as individual images. A custom Python script was used to prepare cropped single cells and a manifest.csv file compatible with the pipeline.

Cell and nucleus alignment

Cells were aligned using a series of three rotations. The first rotation was done with reference to the neuromast organ. The neuromast centroid was calculated from a mask representing the whole neuromast (created from the cell segmentation channel). For each cell, the relative position of the cell centroid to the neuromast centroid was used to calculate the angle between the cell centroid and the x-axis. The corresponding cropped image of the cell was then rotated around the z-axis by this angle to minimize variation originating from the rosette structure of the neuromast.

The second and third rotations were done with reference to the cropped cell only. For the second rotation, the cropped image of the cell was rotated such that the long axis of the cell projected in the xz-plane was aligned to the z-axis. For the second rotation, the cropped image of the cell was rotated such that the long axis of the cell projected in the yz-plane was aligned to the z-axis, unless this angle would be greater than 45 degrees. In that case, the yz long axis was aligned to the y-axis instead. This adjustment prevented cells from being incorrectly rotated by 90 degrees if their long axis was in the horizontal plane.

To generate the nucleus shape space, the nuclei were aligned separately from the cells. The procedure was the same as for the cells, except for the second rotation which also was constrained to be no greater than 45 degrees. If the angle would be greater than 45 degrees, the long axis of the nuclei in the xz-plane was aligned to the x-axis instead of the z-axis.

Spherical harmonics parameterization

Following cell dataset preparation and alignment, spherical harmonics coefficients for each cell and nucleus were calculated using the cvapipe_analysis package (Viana et al. 2023). First, the "loaddata" step was run with the prepared manifest.csv, then the "computefeatures" step was run. To determine the degree of expansion (L_{max}) for spherical harmonics parameterization, we plotted several metrics of reconstruction fidelity for different values of L_{max} using a subset of the data. As L_{max} increases, shapes can be reconstructed with greater detail, but higher L_{max} values incur additional computational costs and exhibit diminishing returns in reconstruction fidelity. We selected an L_{max} of 32 as a value around which reconstruction fidelity plateaued, which yielded 2178 coefficients. The directed Hausdorff distance, which represents the furthest distance between the closest points on the original and reconstructed meshes, was used as a measure of reconstruction error. A Gaussian mixture model was used to identify cells belonging to the second peak in the reconstruction error distribution, which were subsequently excluded from cell shape analysis.

Principal components analysis and unsupervised clustering

Principal components analysis (PCA) was performed using the Python library scikit-learn (Pedregosa et al. 2011). To create "shape modes," PCs were z-scored (i.e. the values for each PC were divided by their respective standard deviation). Visualizations of cells in shape space were generated by applying the inverse PCA transform to generate corresponding SHE coefficients, which were then used to generate 3D reconstructions using the aics-shparam package (Viana et al. 2023). Reconstructions were visualized in 3D using ParaView (Ahrens et al. 2005).

Clustering was performed using the Python package Phenograph (Levine et al. 2015) with the Leiden algorithm for community detection (Traag et al. 2019). For analysis of cell

shape, the first eight PCs were used for clustering; for nuclear shape, the first four PCs were used. These PCs explained 70% and 76% of total variance, respectively. The Uniform Manifold Approximation and Projection (UMAP) implementation from the Python package umap-learn was used to project the data in two dimensions for visualization (McInnes et al. 2018). Partition based graph abstraction (PAGA) was performed using the scanpy Python package (Wolf et al. 2018, 2019). PAGA was used to initialize the layout of UMAPs.

Quantification of fluorescence intensity of transgenes

For reporter lines expressing nuclear localized Eos, *sost:NLS-Eos* and *sfrp1a:NLS-Eos*, the mean intensity within each cell was calculated using the segmented nuclei as masks. For *atoh1a:mRuby*, which has cytoplasmic mRuby localization, the mean intensity within each cell was calculated using the segmented cell as masks. Because intensities of fluorescent proteins from targeted insertions can vary between individual neuromasts and fish, we z-scored the mean intensities for each neuromast and used a threshold of 1 to determine cells "positive" for a marker. In other words, the mean intensity of fluorescent protein within a cell needed to be at least one standard deviation above the mean for that neuromast to be classified as "positive" for that protein.

Measurement of cell location and shape features

Locations of neuromast cells were estimated using the x and y coordinates of the cell segmentation centroids. The neuromast centroid was calculated by using the cell segmentation channel to generate a mask representing the whole neuromast. For each cell, the distance between the cell centroid and neuromast centroid in the xy plane was calculated. This distance was normalized to that of the cell with the greatest distance from the neuromast centroid to account for differences in neuromast size (Viader-Llargués et al. 2018).

We used the first alignment rotation angle to approximate the angular location of each neuromast cell. This angle represents the angle between the neuromast x-axis (which extends from the neuromast centroid) and a vector drawn from the cell centroid to the neuromast centroid in the xy-plane (Figure 3.2B). In our images, the neuromast x-axis is approximately parallel to the anterior-posterior body axis of the fish. Lateral line neuromasts can be polarized in one of two ways relative to the anteroposterior body axis: parallel or perpendicular (López-Schier et al. 2004). Because our dataset contained neuromasts of both types, we standardized the orientations of the neuromasts by adjusting the angles of perpendicular neuromasts using the following formula:

$$if\ o \leq 90 : a = o + 90$$

$$if\ o > 90 : a = 360 - (o + 90)$$

where o is the original angle, and a is the adjusted angle. This is equivalent to rotating a perpendicular neuromast 90 degrees counterclockwise such that its dorsoventral axis is aligned with the anteroposterior body axis. The decision to rotate counterclockwise was based on the fact that Emx2 is expressed in the anterior region of parallel neuromasts and the dorsal region of perpendicular neuromasts (Jiang et al. 2017). The radial distances and angular locations of each cell were combined to plot the locations of neuromast cells on polar coordinates.

Other shape measurements, such as volume, height, etc. were obtained as outputs of the cvapipe_analysis computefeatures step (Viana et al. 2023).

Logistic regression classification

Logistic regression was performed using the Python package scikit-learn (Pedregosa et al. 2011). The data were split into an 80/20 ratio of training data to test data. The test and train

subsets were split such that both had similar proportions of hair cells. The logistic regression model was trained to classify hair cells on the train subset, using one or more shape modes as predictor variables. The trained model was then applied to the testing subset to generate the ROC curves and confusion matrices.

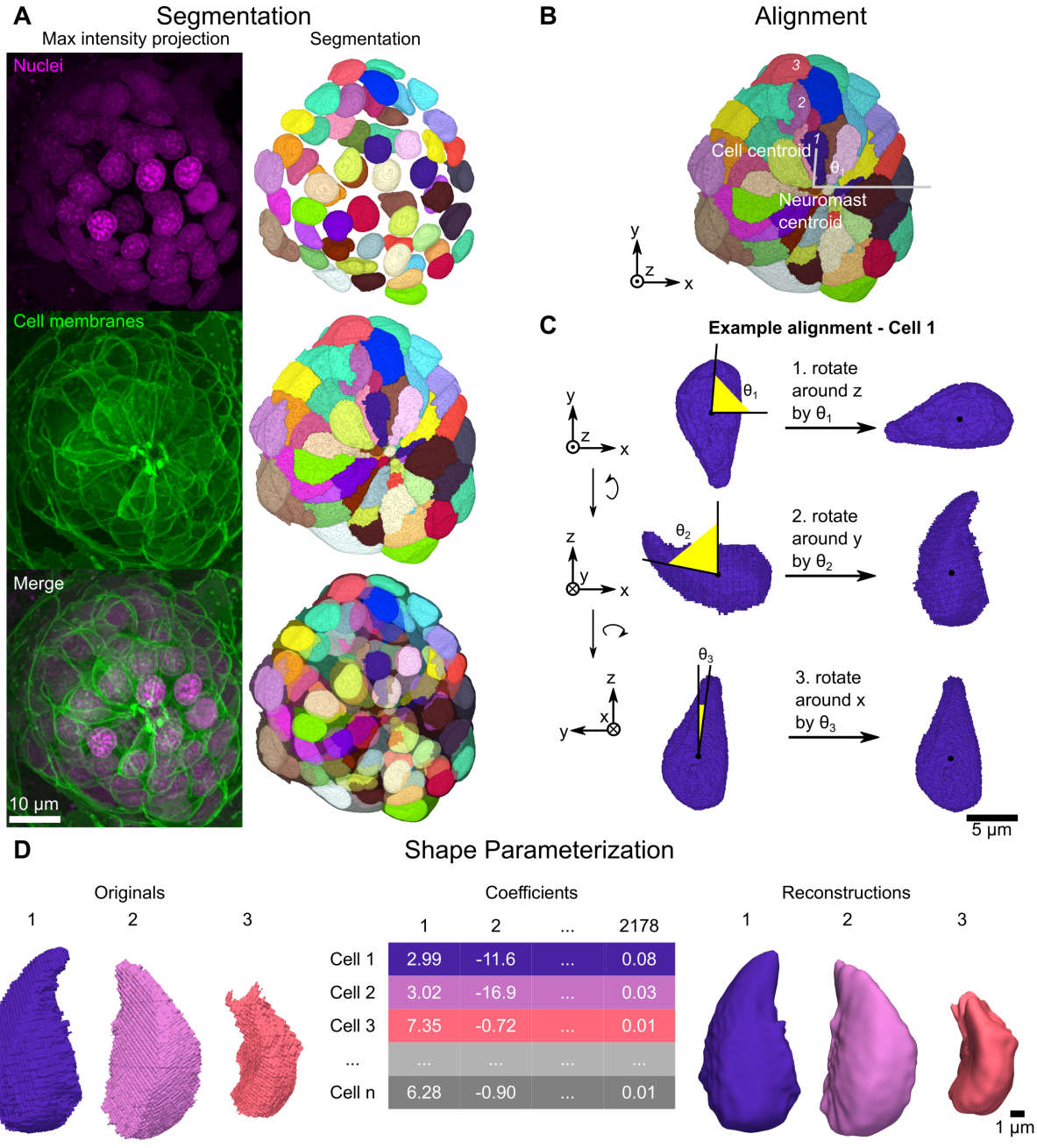

Figure 3.1: Overview of segmentation and shape parameterization

(A) Representative maximum intensity projections (left column) and corresponding 3D projections of segmentations (right column) for nuclei labeled by DRAQ5 dye (top row), cells labeled by *Tg(-8.0cldnb:LY-EGFP)* (middle row), and both channels together (bottom row).

(B) Image depicting how the first rotation angle is calculated. Example given for the maximum intensity projection segmentation channel of the neuromast shown in (A). Lines extending from the neuromast centroid to the cell centroid and depicting the x-axis originating from the

neuromast centroid are overlaid on the image. Cells 1, 2, and 3 used in (C) and (D) are labeled with the corresponding numbers.

(C) Example of the alignment procedure as applied to cell 1 from (B). To correct for radial symmetry, cells are first rotated around the z axis. Cells were then rotated around the y axis to correct for apicobasal tilt, and then around the x axis to correct for off-parallel tilt during imaging.

(D) Overview of shape parameterization using spherical harmonics, as applied to cells 1, 2, and 3 from (B). Spherical harmonics expansion (SHE) is applied to 3D surface meshes of the original, segmented cell surfaces (left) to generate the cell-by-SHE coefficients table (middle) which can then be used to generate 3D reconstructions (right) of each cell.

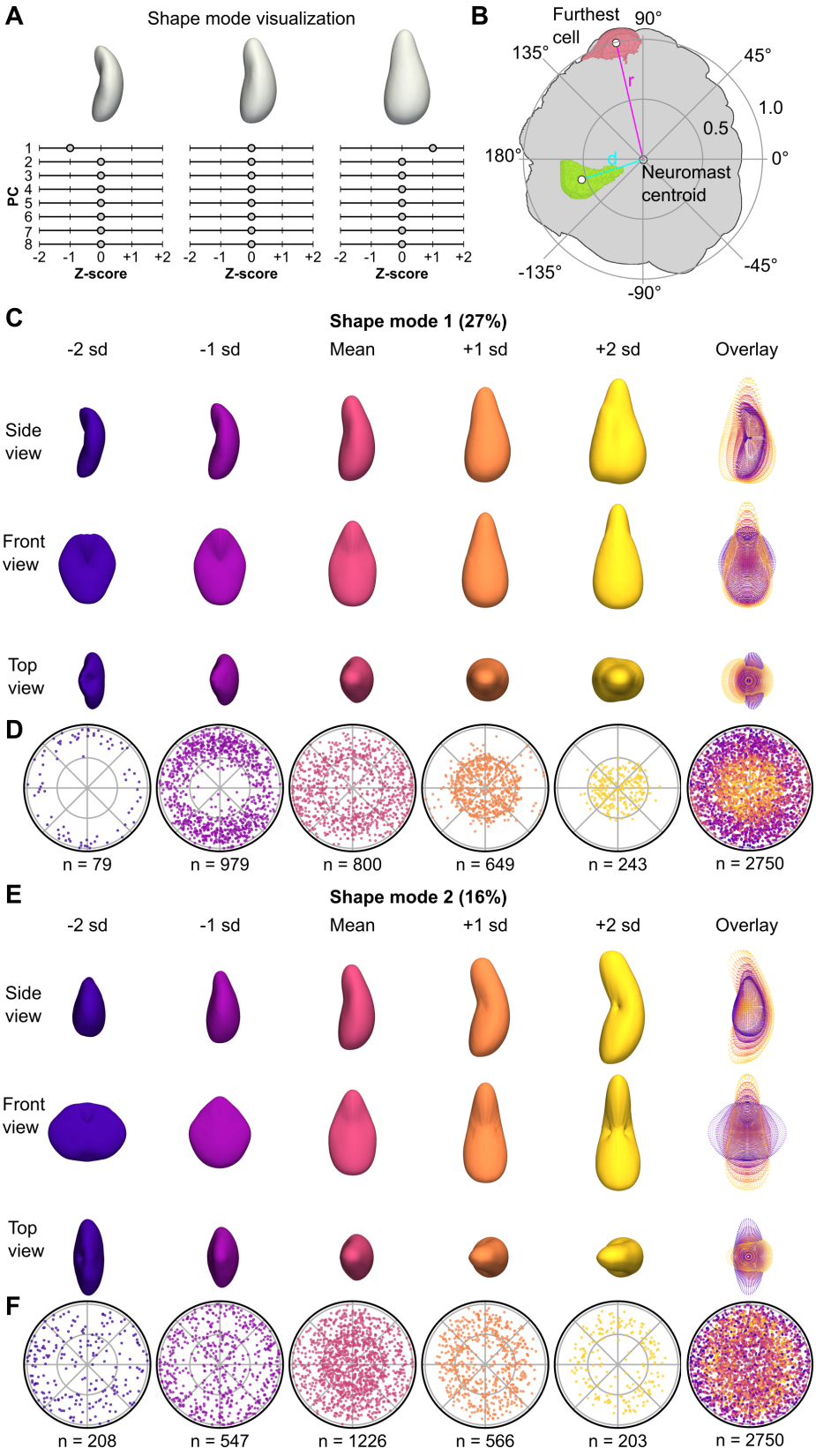
A
Shape mode visualization
PC
1
2
3
4
5
6
7
8
-2 -1 0 +1 +2
Z-score
B
Furthest cell
90°
135°
45°
1.0
0.5
180°
0°
r
d
Neuromast centroid
-135°
-45°
-90°
C
Shape mode 1 (27%)
-2 sd
-1 sd
Mean
+1 sd
+2 sd
Overlay
Side view
Front view
Top view
D
n = 79
n = 979
n = 800
n = 649
n = 243
n = 2750
E
Shape mode 2 (16%)
-2 sd
-1 sd
Mean
+1 sd
+2 sd
Overlay
Side view
Front view
Top view
F
n = 208
n = 547
n = 1226
n = 566
n = 203
n = 2750

Figure 3.2: Visualization of cell shape modes 1 and 2

(A) Schematic depicting how shape variation was visualized. PCs were first z-scored to generate shape modes. Visual representations of each shape mode were generated by finding the mean cell (a hypothetical cell with a value of 0 for all 8 shape modes) and varying one shape mode (here, shape mode 1) by up to 2 standard deviations (sd) in increments of 1 sd while holding other shape modes at the mean (0).

(B) Schematic depicting how relative cell locations within each neuromast were calculated. First, for each neuromast, the distance between the neuromast centroid and the furthest cell (r) in the XY plane was calculated. The distances between the neuromast centroid and cell centroids were divided by (r) to yield the normalized distance from the neuromast center (d) for each cell. The angular location of each cell was determined in reference to the positive x-axis centered on the neuromast centroid. Neuromast cell locations were thus projected onto a unit circle with radius 1, allowing relative cell locations from multiple neuromasts to be plotted together.

(C) Visualization of the first mode of cell shape variation (Cell shape mode 1, CSM1), generated as described in (A). 3D surface renderings are shown from 3 different views, as well as an overlay of point representations for each view (rightmost column).

(D) Polar plots of relative cell locations (generated as shown in B) binned by CSM1 scores. Bins were centered on the corresponding z-score and included cells with values within 0.5 (e.g., the second plot from the right corresponded to cells with CSM1 scores between -1.5 sd and -0.5 sd). For the -2 sd and 2 sd plots, the upper bounds were not limited to within 0.5 (e.g. the first plot includes all cells with CSM1 values < -1.5 sd). An overlay of the first 5 plots is shown in the rightmost column.

(E) Visualization of the second mode of cell shape variation (Cell shape mode 2, CSM2), generated as described in (A). 3D surface renderings are shown from 3 different views, as well as an overlay of point representations for each view (rightmost column).

(F) Polar plots of relative cell locations (generated as shown in B) binned by CSM2 scores. An overlay of the first 5 plots is shown in the rightmost column.

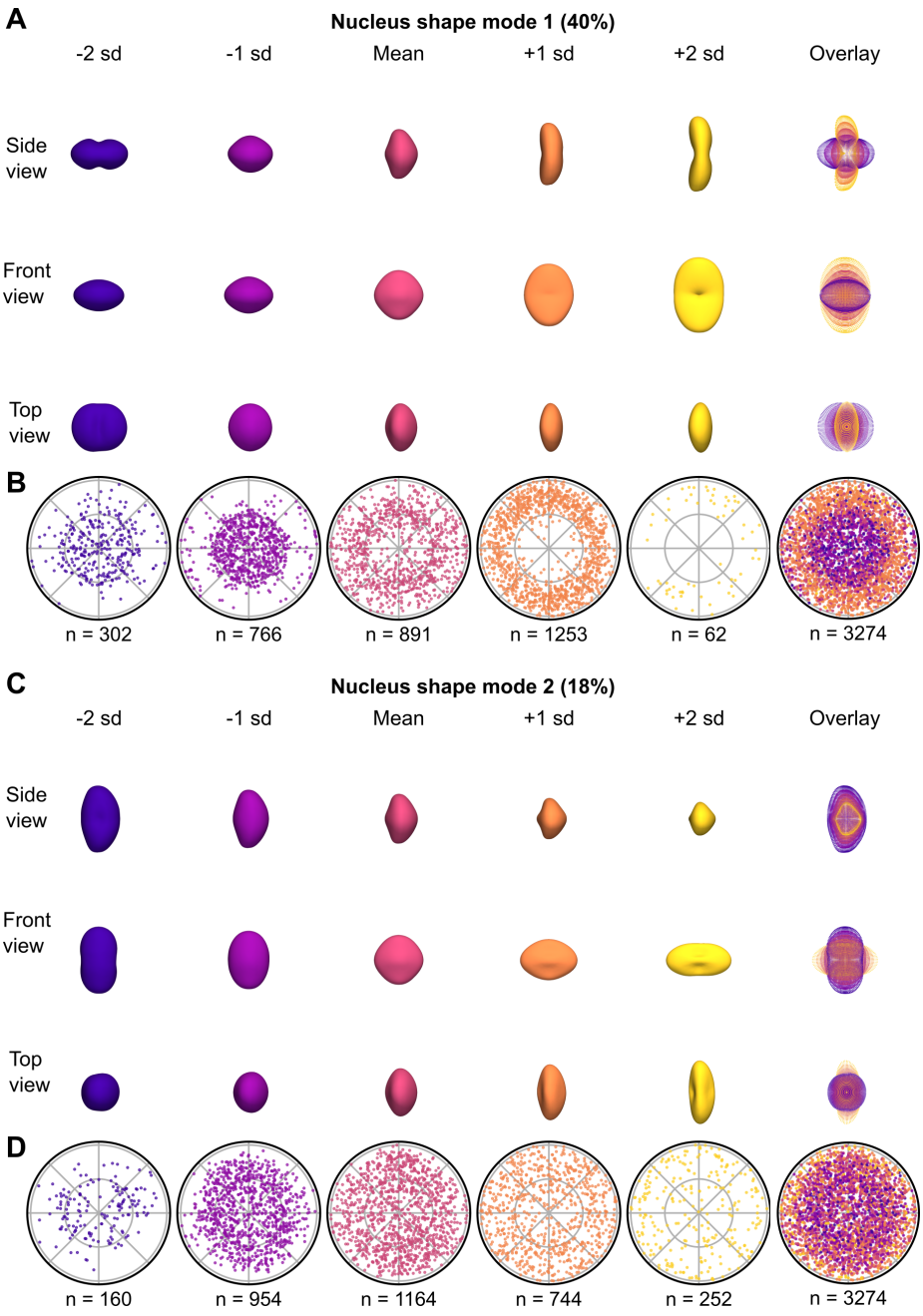

Figure 3.3: Visualization of nuclear shape modes 1 and 2

(A) Visualization of the first mode of nucleus shape variation (Nucleus shape mode 1, NSM1), generated as described in Figure 3.2A. 3D surface renderings are shown from 3 different views, as well as an overlay of point representations for each view (rightmost column).

(B) Polar plots of relative cell locations (generated as shown in Figure 3.2B) binned by NSM1 scores. Bins were centered on the corresponding z-score and included cells with values within 0.5 (e.g., the second plot from the right corresponded to cells with NSM1 scores between -1.5 sd and -0.5 sd). For the -2 sd and 2 sd plots, the upper bounds were not limited to within 0.5 (e.g.

the first plot includes all cells with NSM1 values < -1.5 sd). An overlay of the first 5 plots is shown in the rightmost column.

(C) Visualization of the second mode of nucleus shape variation (Nucleus shape mode 2, NSM2), generated as described in Figure 3.2A. 3D surface renderings are shown from 3 different views, as well as an overlay of point representations for each view (rightmost column).

(D) Polar plots of relative cell locations (generated as shown in Figure 3.2B) binned by NSM2 scores. An overlay of the first 5 plots is shown in the rightmost column.

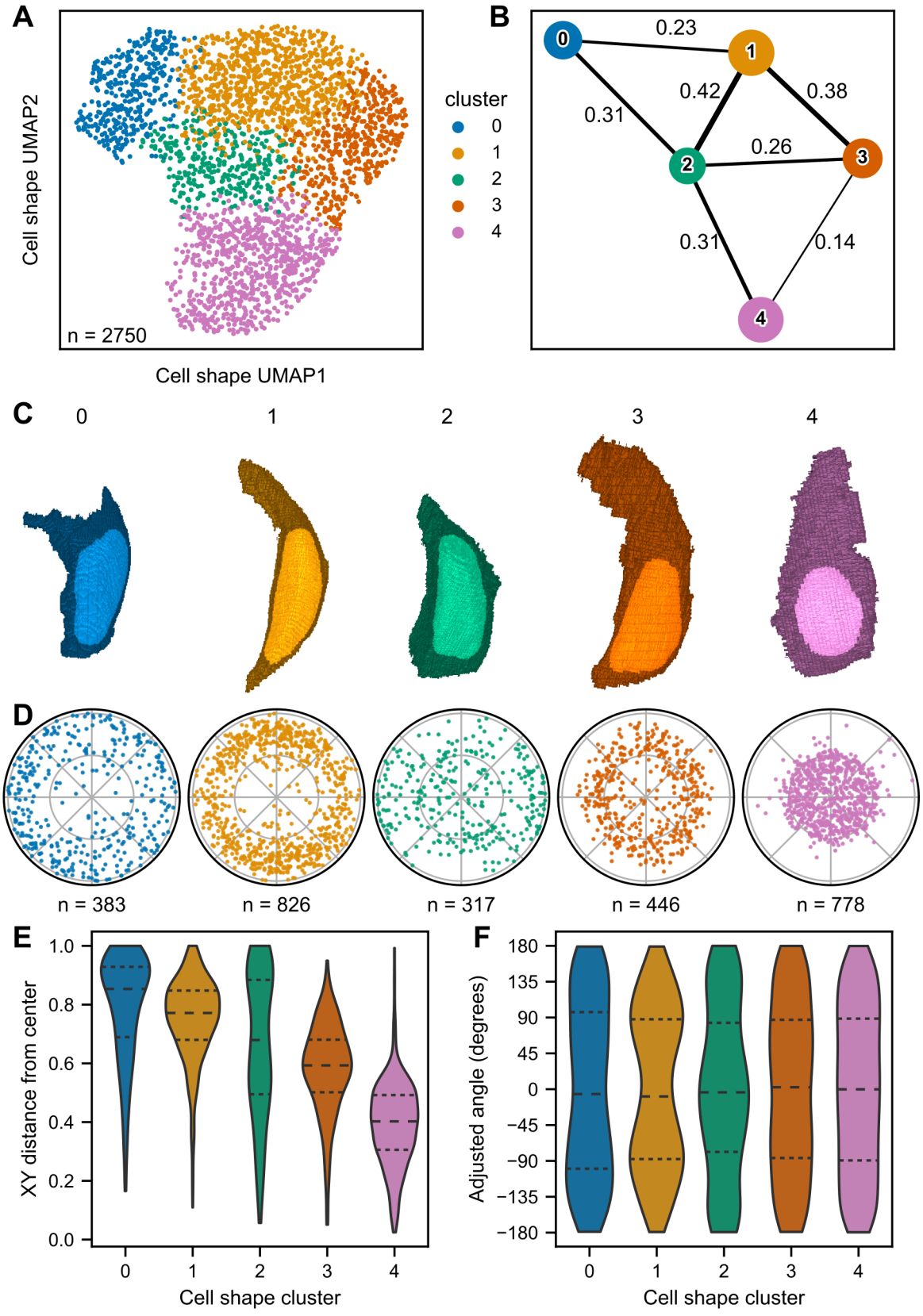
A
Cell shape UMAP2
Cell shape UMAP1
n = 2750
cluster
0
1
2
3
4
B
0.23
0.31
0.42
0.38
0.26
0.31
0.14
C
D
n = 383
n = 826
n = 317
n = 446
n = 778
E
XY distance from center
Cell shape cluster
F
Adjusted angle (degrees)
Cell shape cluster

Figure 3.4: Unsupervised clustering of cells in shape space

(A) UMAP of neuromast cells, color coded by cell shape cluster. Colors and associated cluster numbers are used in (B), (C), (D), (E), and (F).

(B) PAGA plot of cell shape clusters. Each node represents a cluster. Thickness of the line drawn between nodes indicates estimated connectivity between clusters (the value of which is shown adjacent to the corresponding line). Edges with connectivity below 0.1 are not depicted.

(C) 3D projections of representative cells for each cluster, defined as the cell closest to the cluster centroid in eight-dimensional PC space. The original segmentation masks (not SHE reconstructions) are depicted.

(D) Polar plots of relative neuromast locations of cells within each cluster.

(E) Distributions of the cell distance from the neuromast center for each cluster. Dashed lines indicate quartiles. Distances were calculated as the distance between the xy coordinates of cell centroids and the xy coordinates of the corresponding neuromast centroid. Distances were normalized to that of the cell with the greatest distance from the center (see Figure 3.2B).

(F) Distributions of neuromast cell angles for each cluster. Dashed lines indicate quartiles. Angles were calculated with reference to the positive x-axis extending from the neuromast centroid. Cluster 1 shows a bias towards the dorsoventral poles (90, -90), while cluster 2 shows a bias to the anterior-posterior compartments (0, 180, -180).

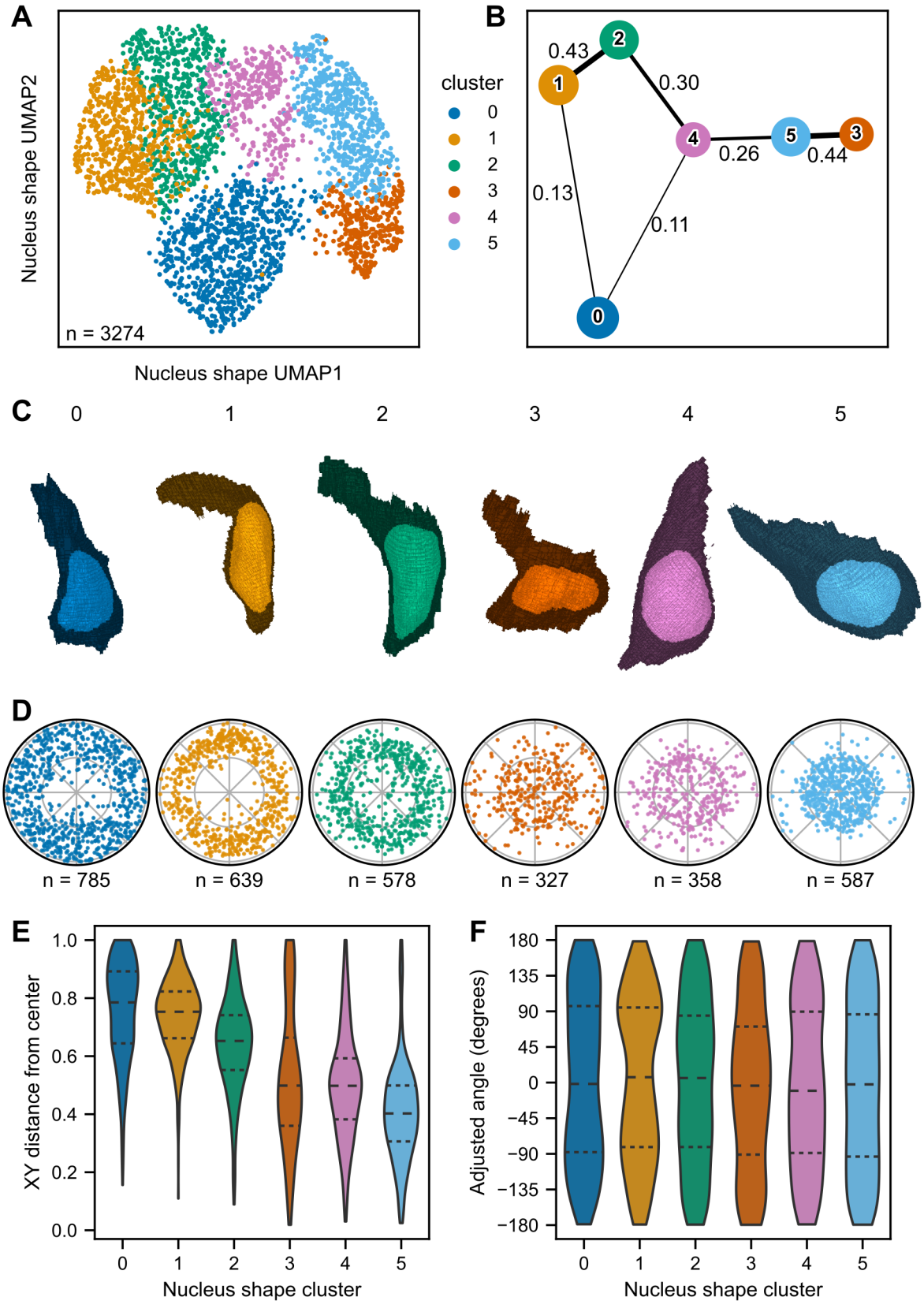
A
Nucleus shape UMAP2
Nucleus shape UMAP1
n = 3274
B
cluster
0
1
2
3
4
5
0.43
0.30
0.26
0.44
0.13
0.11
C
0
1
2
3
4
5
D
n = 785
n = 639
n = 578
n = 327
n = 358
n = 587
E
XY distance from center
1.0
0.8
0.6
0.4
0.2
0.0
Nucleus shape cluster
F
Adjusted angle (degrees)
180
135
90
45
0
−45
−90
−135
−180
Nucleus shape cluster

Figure 3.5: Unsupervised clustering of nuclei in shape space

(A) UMAP of neuromast cells, color coded by nucleus shape cluster. Colors and associated cluster numbers are used in (B), (C), (D), (E), and (F).

(B) PAGA plot of nucleus shape clusters. Each node represents a cluster. Thickness of the line drawn between nodes indicates estimated connectivity between clusters (the value of which is shown adjacent to the corresponding line). Edges with connectivity below 0.1 are not depicted.

(C) 3D projections of representative cells for each nuclear cluster, defined as the cell closest to the cluster centroid in four-dimensional PC space. The original segmentation masks are depicted (not SHE reconstructions).

(D) Polar plots of relative locations of cells within each cluster.

(E) Distributions of the cell distance from the neuromast center for each cluster. Dashed lines indicate quartiles. Distances were calculated as the distance between the xy coordinates of cell centroids and the xy coordinates of the corresponding neuromast centroid. Distances were normalized to that of the cell with the greatest distance from the center.

(F) Distributions of neuromast cell angles for each cluster. Dashed lines indicate quartiles. Angles were calculated with reference to the positive x-axis extending from the neuromast centroid.

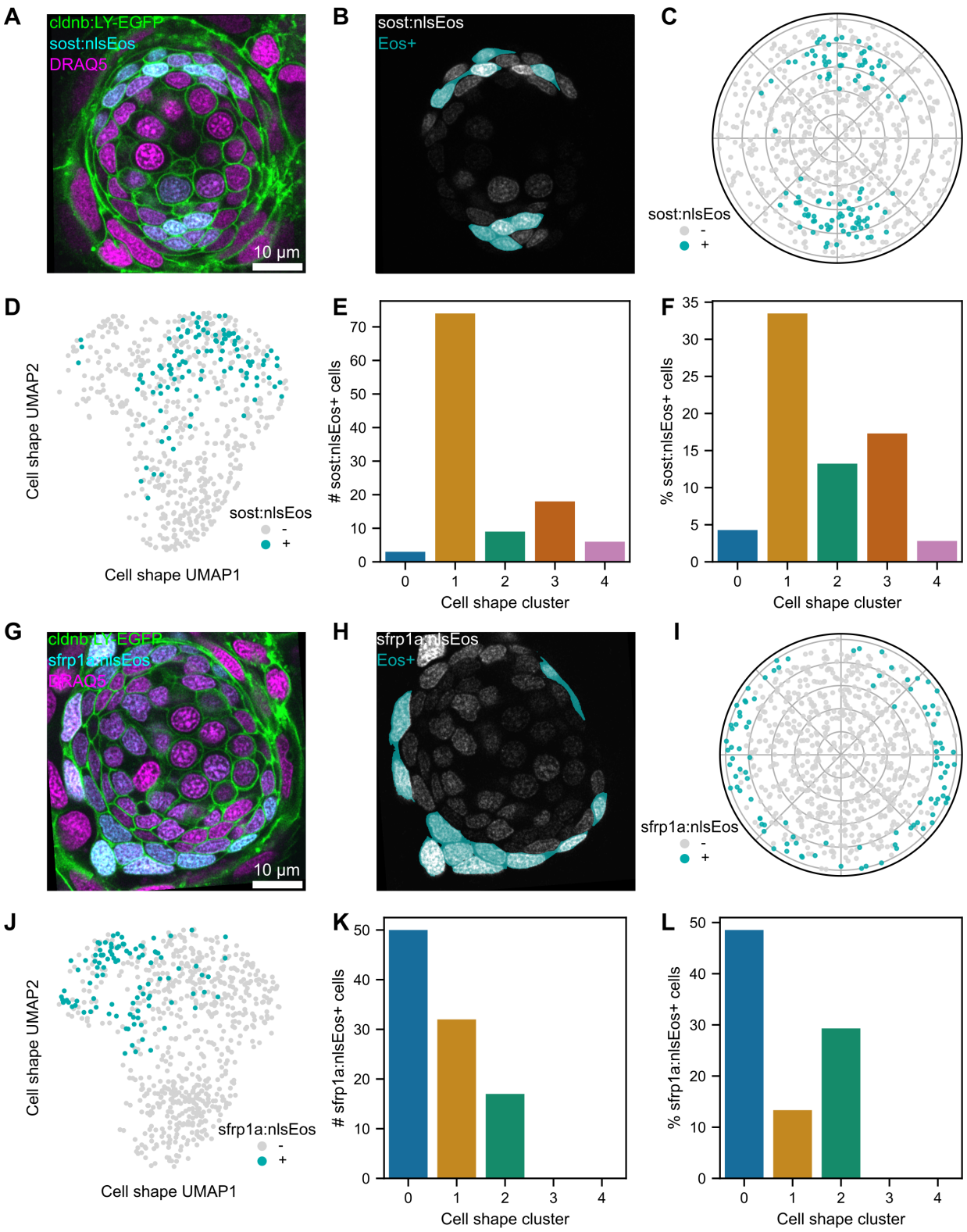
A
cldnb:LY-EGFP
sost:nlsEos
DRAQ5
10 µm
B
sost:nlsEos
Eos+
C
sost:nlsEos
-
+
D
Cell shape UMAP2
Cell shape UMAP1
sost:nlsEos
-
+
E
sost:nlsEos+ cells
Cell shape cluster
F
% sost:nlsEos+ cells
Cell shape cluster
G
cldnb:LY-EGFP
sfrp1a:nlsEos
DRAQ5
10 µm
H
sfrp1a:nlsEos
Eos+
I
sfrp1a:nlsEos
-
+
J
Cell shape UMAP2
Cell shape UMAP1
sfrp1a:nlsEos
-
+
K
sfrp1a:nlsEos+ cells
Cell shape cluster
L
% sfrp1a:nlsEos+ cells
Cell shape cluster

Figure 3.6: Location and shape characteristics of cells expressing *sost:NLS-Eos* and *sfrp1a:NLS-Eos*

(A) Single confocal slice of a neuromast from *sost:NLS-Eos; Tg(-8.0cldnb:LY-EGFP)* fish stained with DRAQ5. Image contrast was adjusted for visibility.

(B) The same slice as in (A), with the *sost:NLS-Eos* channel (gray) overlaid with a mask indicating cells classified as Eos+ (dark cyan).

(C) Polar plot showing relative cell locations of locations of Eos+ (dark cyan) and Eos- (gray) cells.

(D) UMAP of Eos+ (dark cyan) and Eos- (gray) cells from *sost:NLS-Eos*.

(E) *sost:NLS-Eos*+ cells plotted as raw counts within each cell shape cluster.

(F) *sost:NLS-Eos*+ cells plotted as the percentage of each cell shape cluster.

(G) Single confocal slice of a neuromast from *sfrp1a:NLS-Eos; Tg(-8.0cldnb:LY-EGFP)* fish stained with DRAQ5. Image contrast was adjusted for visibility.

(H) The same slice as in (A), with the *sfrp1a:NLS-Eos* channel (gray) overlaid with a mask indicating cells classified as Eos+ (dark cyan).

(I) Polar plot showing relative cell locations of locations of Eos+ (dark cyan) and Eos- (gray) cells.

(J) UMAP of Eos+ (dark cyan) and Eos- (gray) cells from *sfrp1a:NLS-Eos*.

(K) *sfrp1a:NLS-Eos*+ cells plotted as raw counts within each cell shape cluster.

(L) *sfrp1a:NLS-Eos*+ cells plotted as the percentage of each cell shape cluster.

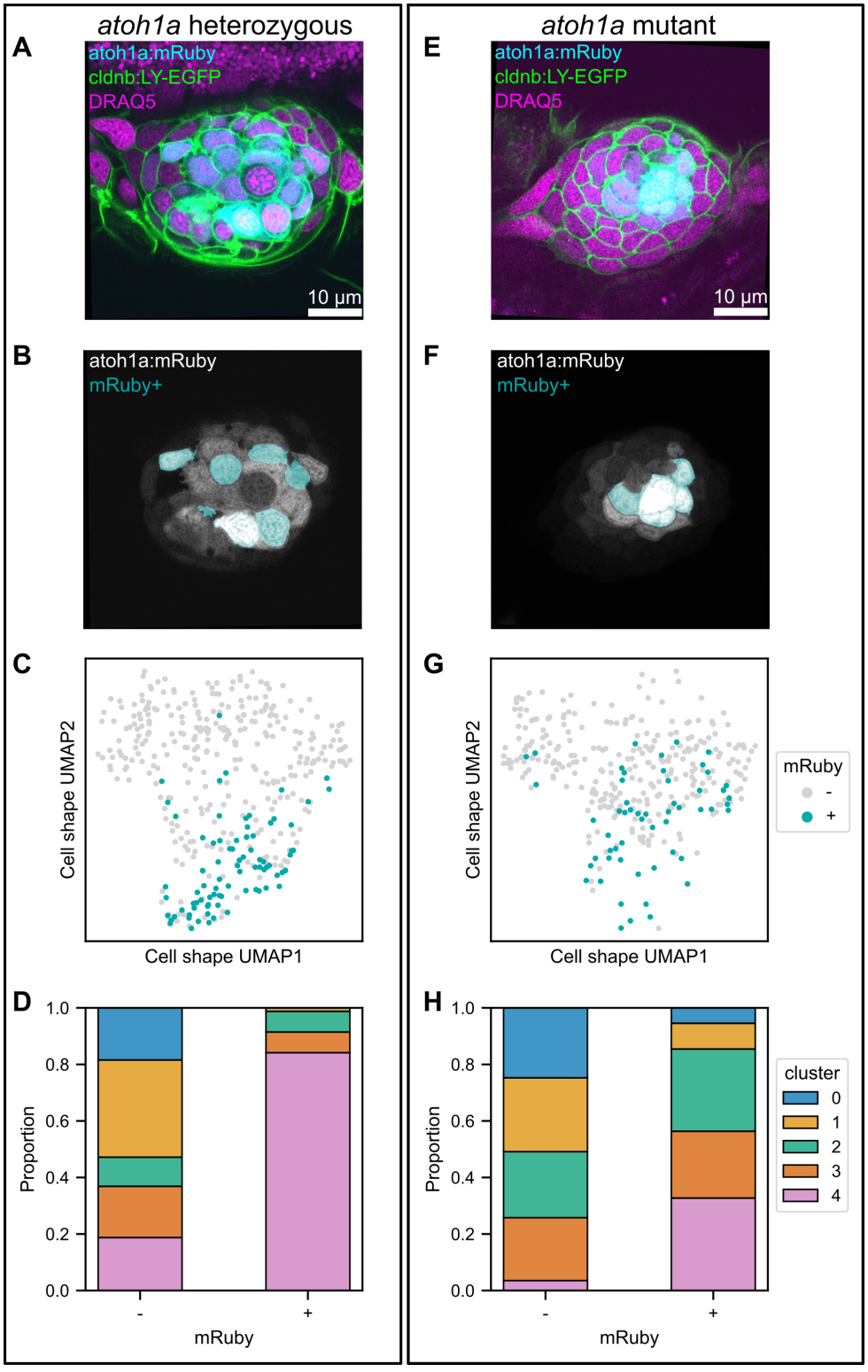
atoh1a heterozygous
atoh1a mutant
A
E
atoh1a:mRuby
cldnb:LY-EGFP
DRAQ5
10 µm
B
F
atoh1a:mRuby
mRuby+
C
G
Cell shape UMAP2
Cell shape UMAP1
mRuby
-
+
D
H
Proportion
1.0
0.8
0.6
0.4
0.2
0.0
cluster
0
1
2
3
4

Figure 3.7: Shape characteristics of *atoh1a:mRuby* heterozygotes and mutants

Analysis of cell shape distributions in *atoh1a:mRuby* heterozygotes (A-D) and mutants (E-G).

(A, E) Single confocal slice of a neuromast from a *atoh1a:mRuby* heterozygote (A) and mutant (E) also expressing *Tg(-8.0cldnb:LY-EGFP)* and stained with DRAQ5. Image contrast was adjusted for visibility.

(B, F) The same slices as in (A) and (E), with the *atoh1a:mRuby* channel (gray) overlaid with a mask indicating cells classified as mRuby+ (dark cyan) for a *atoh1a:mRuby* heterozygote (B) and mutant (F).

(C, G) UMAP of mRuby+ (dark cyan) and mRuby- (gray) cells from *atoh1a:mRuby* heterozygotes (C) and mutants (F).

(D, H) Proportions of mRuby- cells (left bar) and mRuby+ cells (right bar) from *atoh1a:mRuby* heterozygotes (D) and mutants (H) in each cell shape cluster.

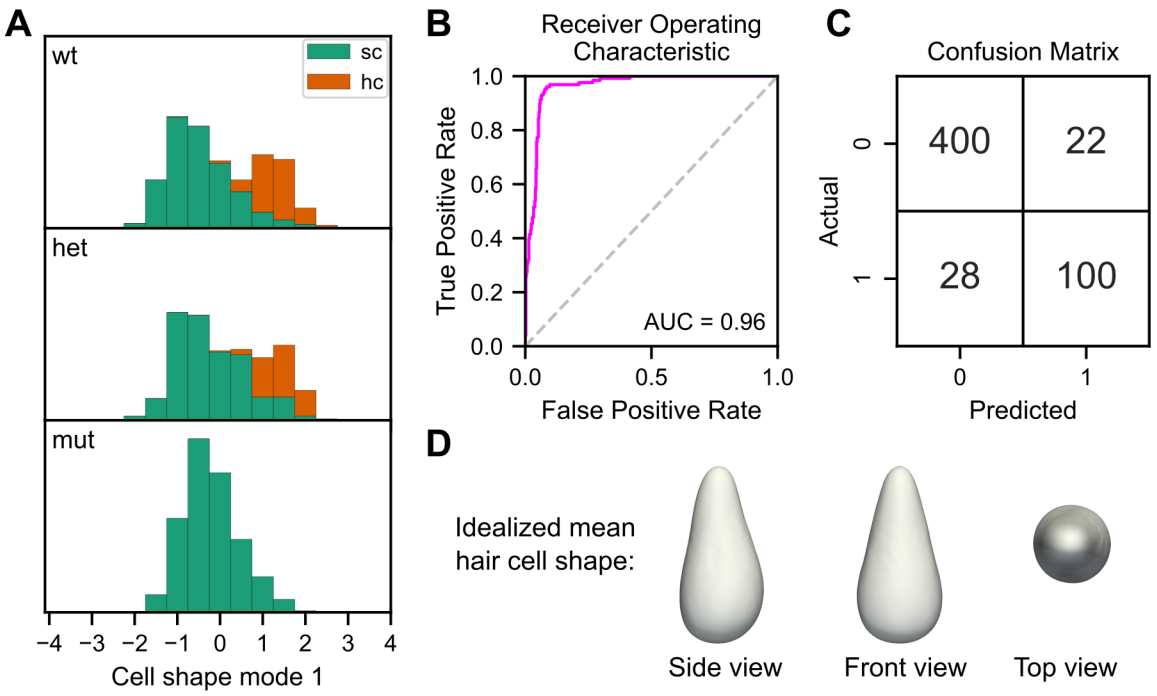

Figure 3.8: Logistic classifier for hair cells based on cell shape features

(A) Distributions of cell shape mode 1 scores, separated by genotype (top row: wildtype; middle row: *atoh1a* heterozygous; bottom row: *atoh1a* mutant). Hair cells (hc, green) and support cells (sc, orange) are color coded and displayed as stacked histograms.

(B) Receiver Operating Characteristic (ROC) curve (fuchsia) for a logistic regression classifier trained to detect hair cells based on cell shape mode 1-8 scores. The Area Under the Curve (AUC) score is shown in the lower left of the plot (0.96). The silver dashed line on the diagonal represents the performance of a random classifier.

(C) Confusion matrix for the cell shape-based hair cell classifier. 0 = support cells; 1 = hair cells. Top left: true negatives; top right: false positives; bottom left: false negatives; bottom right: true positives.

(D) The idealized mean cell shape for hair cells within the dataset.

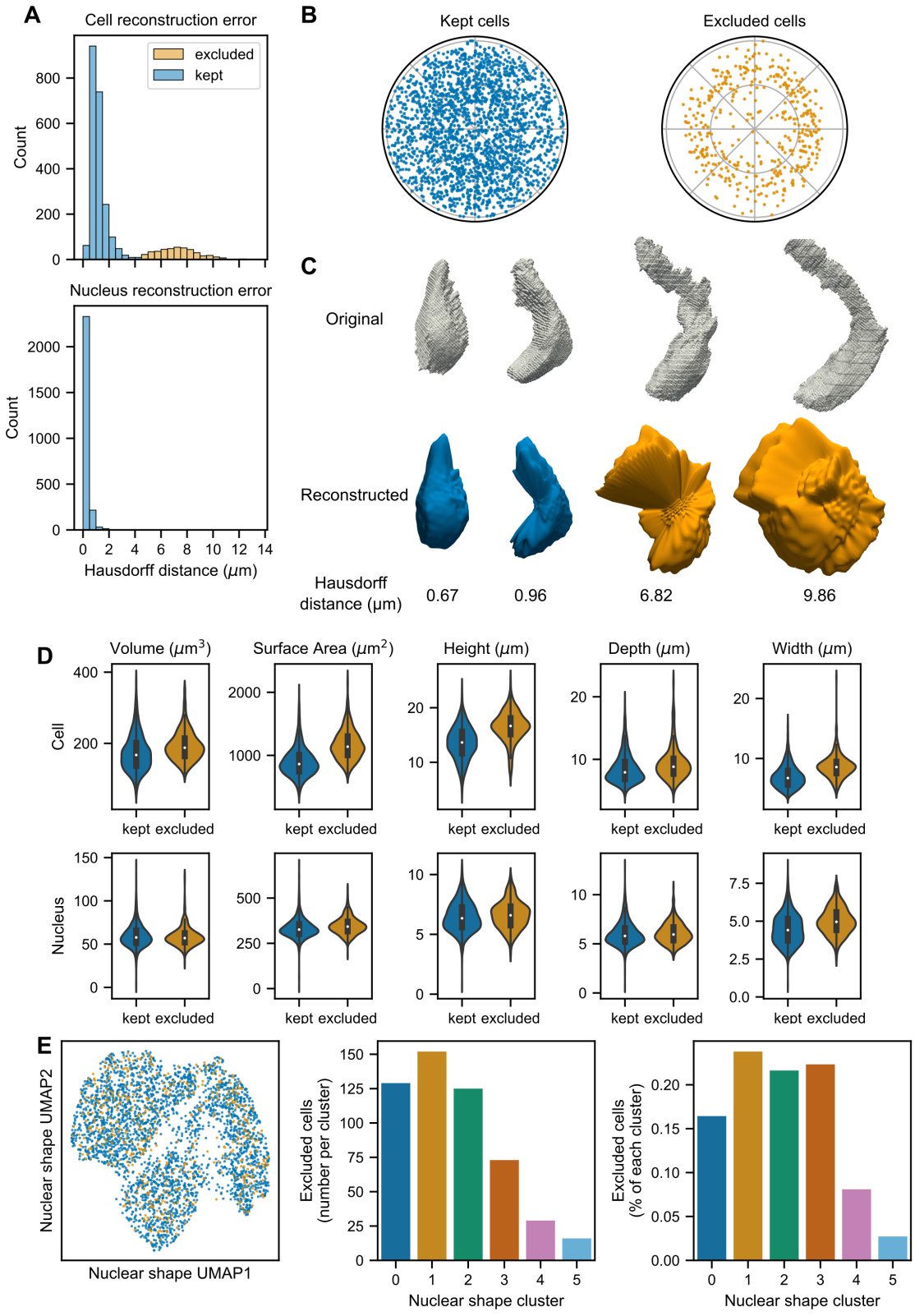
A
Cell reconstruction error
excluded
kept
Count
Nucleus reconstruction error
Hausdorff distance (μm)
B
Kept cells
Excluded cells
C
Original
Reconstructed
Hausdorff distance (μm)
0.67
0.96
6.82
9.86
D
Volume (μm³)
Surface Area (μm²)
Height (μm)
Depth (μm)
Width (μm)
Cell
Nucleus
kept excluded
E
Nuclear shape UMAP2
Nuclear shape UMAP1
Excluded cells (number per cluster)
Excluded cells (% of each cluster)
Nuclear shape cluster

Supplemental Figure 3.9

(A) Distribution of reconstruction error, as measured by directed Hausdorff distance, for cell shape (top) and nuclear shape (bottom). Some cells were excluded from cell shape analysis (orange) due to high reconstruction error.

(B) Polar plots showing relative locations of cells kept (left, blue) and excluded from cell shape analysis (right, orange).

(C) Examples of well reconstructed (left) and poorly reconstructed (right) cells. 3D representations of the original mesh (top), reconstructed mesh (middle), and the associated Hausdorff distances (bottom) for two examples of each are shown.

(D) Distributions of cell (top) and nuclei (bottom) shape features in kept (blue) and excluded (orange) cells.

(E) Left: UMAP projection of cells in nuclear shape space (corresponding with Figure 5A) colored by whether they were kept (blue) or excluded (orange) from cell shape analysis. Middle: Excluded cells plotted as number (raw counts) for each nuclear shape cluster. Right: Excluded cells as a percentage of each nuclear shape cluster.

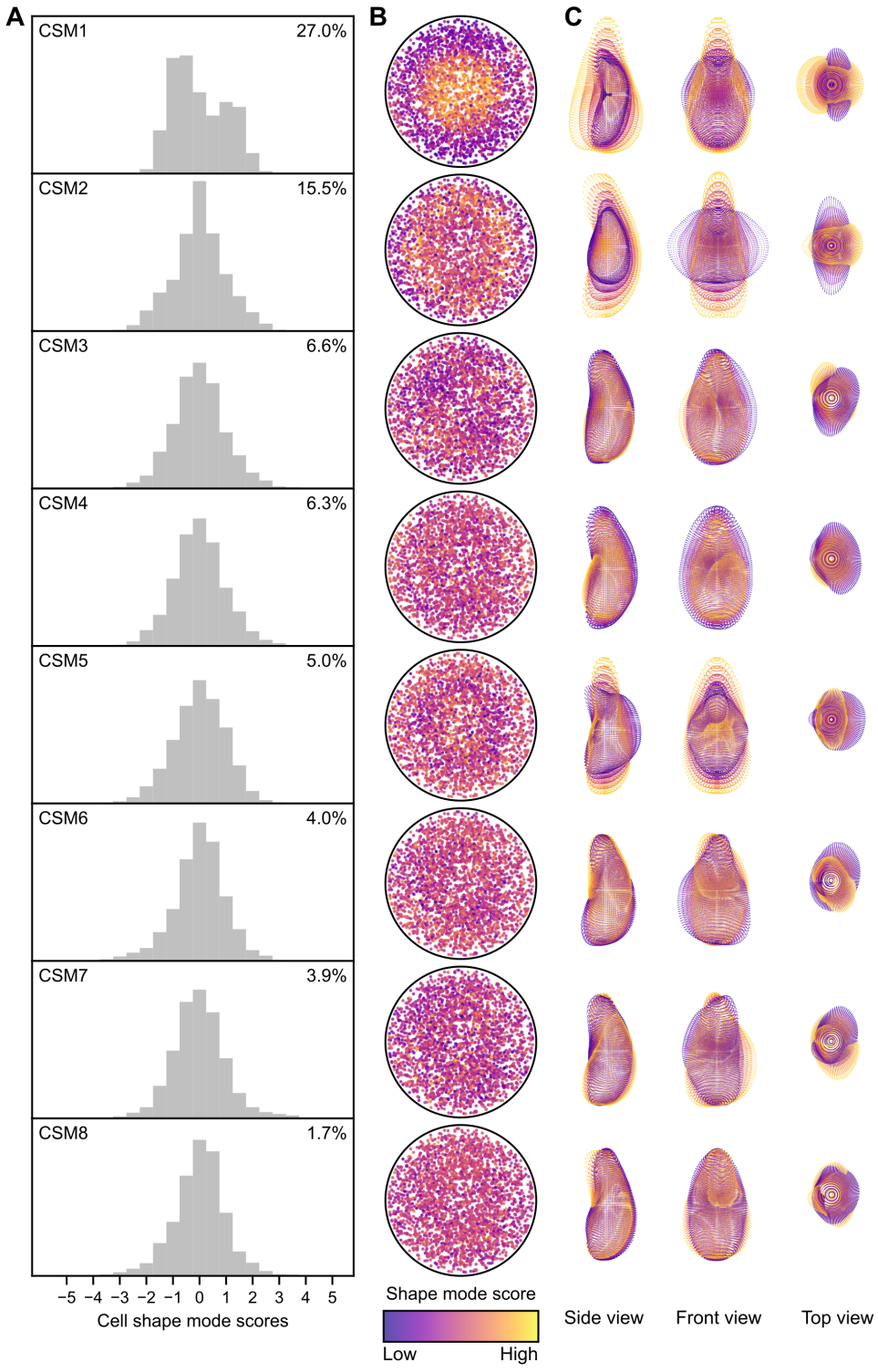
A
CSM1
27.0%
CSM2
15.5%
CSM3
6.6%
CSM4
6.3%
CSM5
5.0%
CSM6
4.0%
CSM7
3.9%
CSM8
1.7%
−5 −4 −3 −2 −1 0 1 2 3 4 5
Cell shape mode scores
B
Shape mode score
Low
High
C
Side view
Front view
Top view

Supplemental Figure 3.10

(A) Distributions of shape mode scores for the first eight cell shape modes (CSM1-CSM8). Percent variance explained for each shape mode is provided in the upper right corner.

(B) Polar plots showing relative locations of neuromast cells in the dataset, color coded by shape mode scores for CSM1-CSM8.

(C) Overlaid 3D point view representations of CSM1-CSM8, generated by finding the mean cell and varying each shape mode by up to 2 standard deviations (sd) in increments of 1 sd while holding other shape modes at the mean (0).

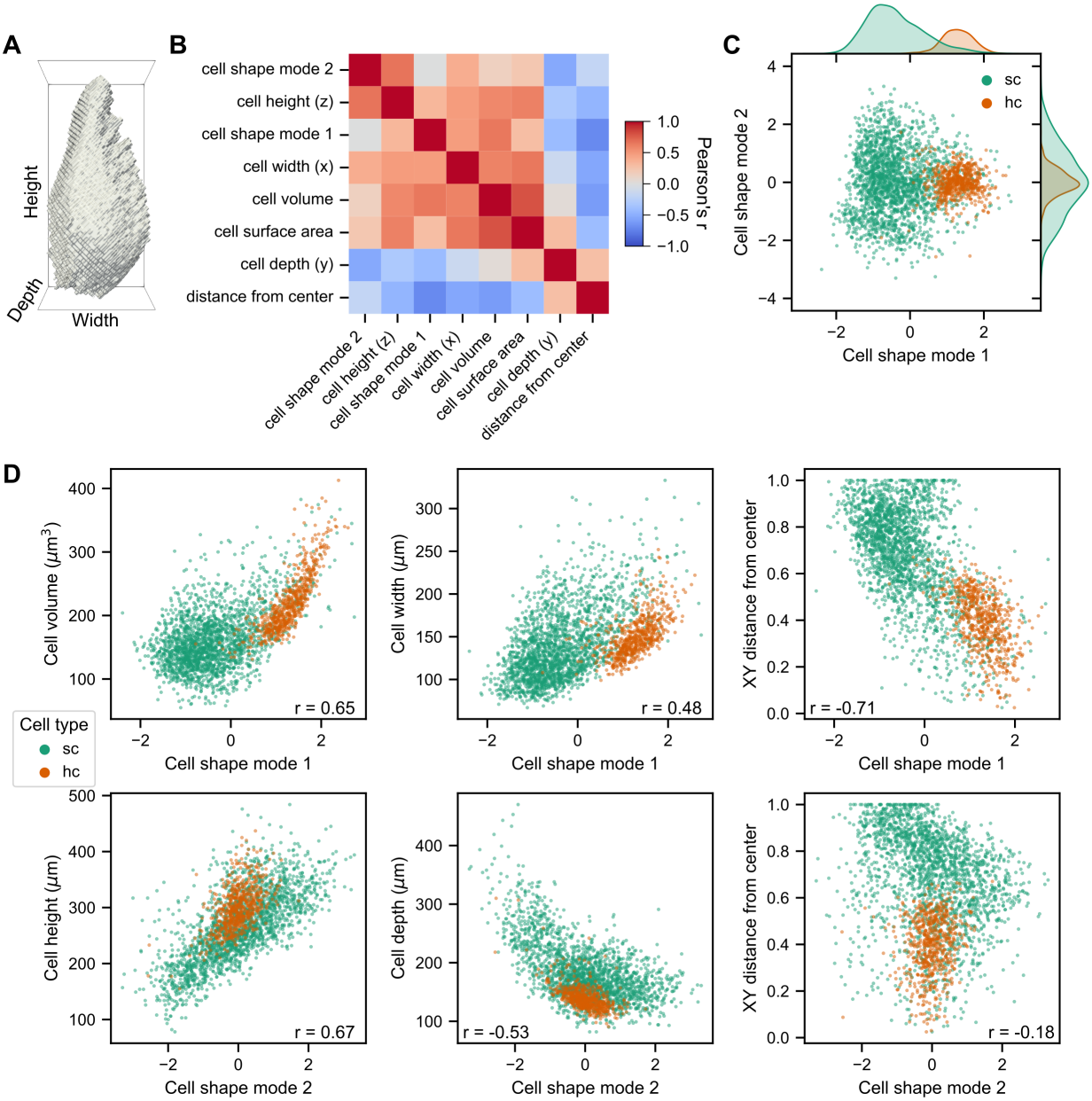

Supplemental Figure 3.11

(A) Side view of a 3D projection of a representative cell with its dimensions labeled.

(B) Heatmap of correlations between cell shape mode 1, cell shape mode 2, and cell shape/location features.

(C) Plot of cell shape mode 1 and cell shape mode 2 for support cells (green) and hair cells (orange).

(D) Top row: Correlations between cell volume (left), width (center), and distance from center (right) versus cell shape mode 1 color coded by cell type. Bottom row: Correlations between cell height (left), depth (center), and distance from center (right) versus cell shape mode 2 color coded by cell type. The Pearson correlation coefficient (r) is displayed on each plot. Support cells (green) and hair cells (orange).

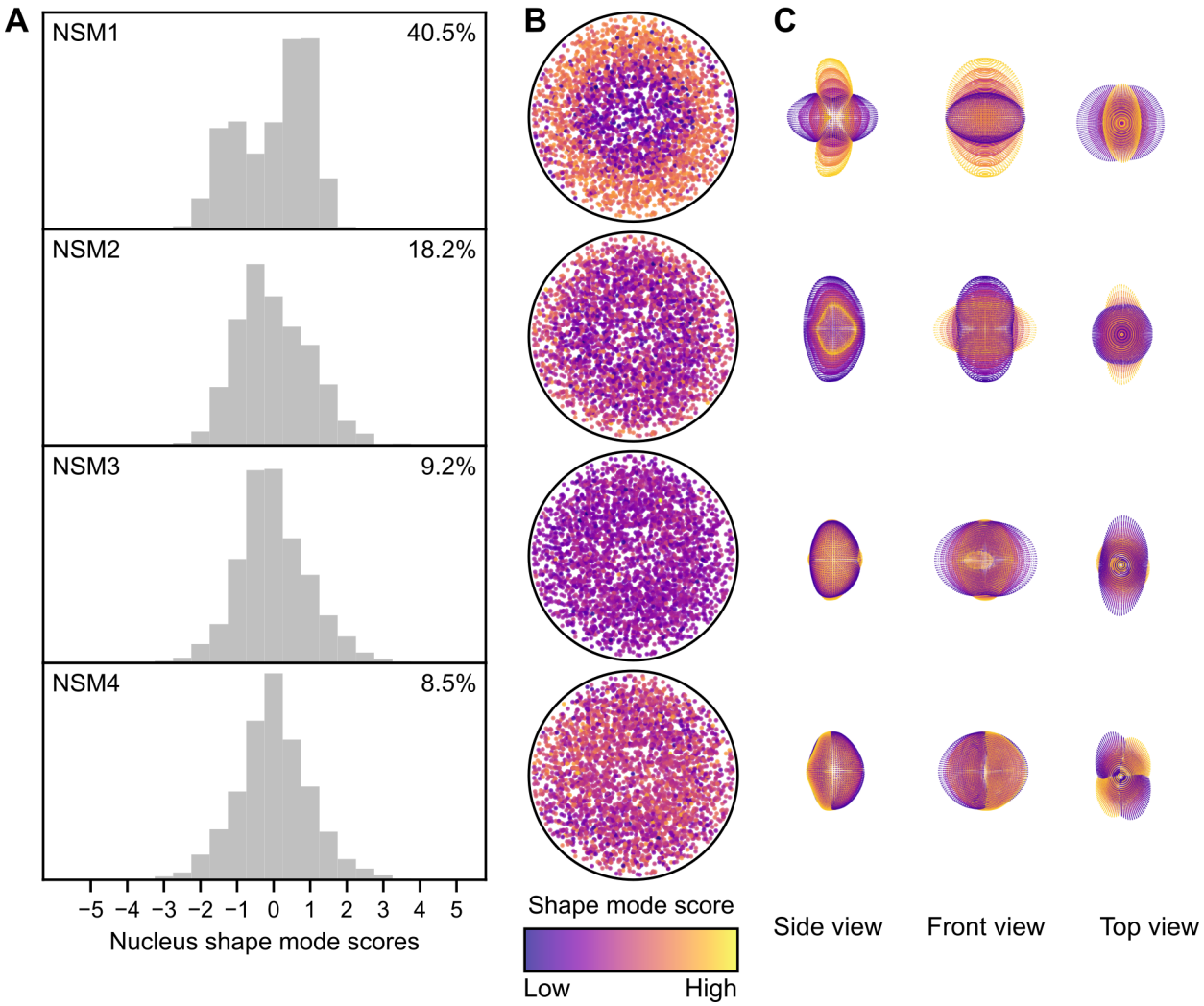

Supplemental Figure 3.12

(A) Distributions of shape mode scores for the first four nucleus shape modes (NSM1-NSM4). Percent variance explained for each shape mode is provided in the upper right corner.

(B) Polar plots showing relative locations of neuromast cells in the dataset, color coded by shape mode scores for NSM1-NSM4.

(C) Overlaid 3D point view representations of CSM1-CSM8, generated by finding the mean cell and varying each shape mode by up to 2 standard deviations (sd) in increments of 1 sd while holding other shape modes at the mean (0).

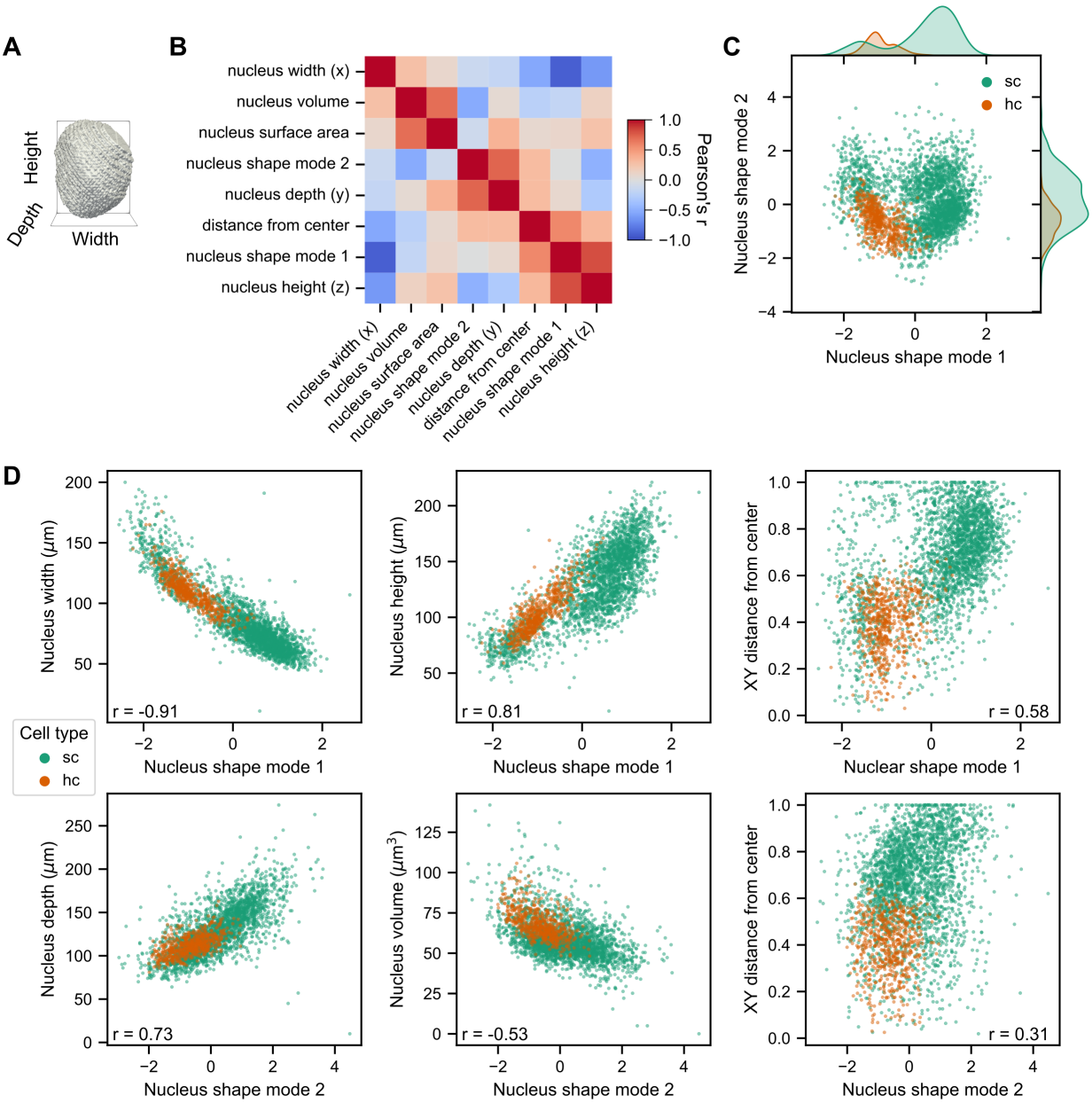

Supplemental Figure 3.13

(A) Side view of a 3D projection of a representative nucleus with its dimensions labeled.

(B) Heatmap of correlations between nucleus shape mode 1, nucleus shape mode 2, and nucleus shape/location features.

(C) Plot of nucleus shape mode 1 and nucleus shape mode 2 for support cells (green) and hair cells (orange).

(D) Top row: Correlations between nucleus width (left), height (center), and distance from center (right) versus nucleus shape mode 1 color coded by cell type. Bottom row: Correlations between nucleus depth (left), volume (center), and distance from center (right) versus nucleus shape mode 2 color coded by cell type. The Pearson correlation coefficient (r) is displayed on each plot. Support cells (green) and hair cells (orange).

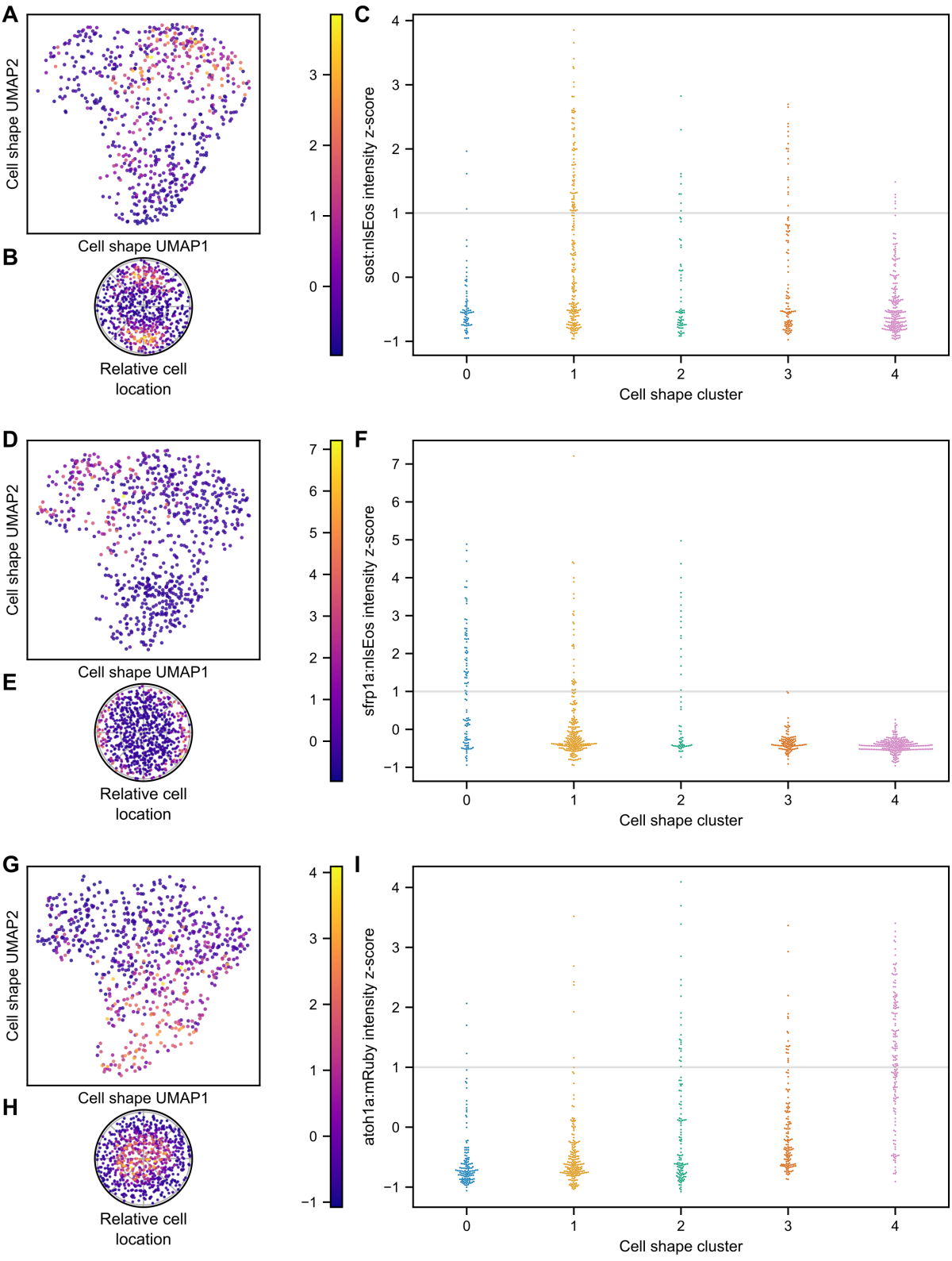
A
Cell shape UMAP2
Cell shape UMAP1
B
Relative cell location
C
sost:nlsEos intensity z-score
Cell shape cluster
D
Cell shape UMAP2
Cell shape UMAP1
E
Relative cell location
F
sfrp1a:nlsEos intensity z-score
Cell shape cluster
G
Cell shape UMAP2
Cell shape UMAP1
H
Relative cell location
I
atoh1a:mRuby intensity z-score
Cell shape cluster

Supplemental Figure 3.14

(A) UMAP of cells from *sost:NLS-Eos* colored by mean Eos intensity (z-scored).

(B) Polar plot showing relative locations of neuromast cells colored by mean *sost:NLS-Eos* intensity (z-scored).

(C) Distribution of mean *sost:NLS-Eos* intensities (z-scored) for cells in each cell shape cluster. Gray line represents intensity threshold (1 SD) used to label a cell as positive.

(D) UMAP of cells from *sfrp1a:NLS-Eos* colored by mean Eos intensity (z-scored).

(E) Polar plot showing relative locations of neuromast cells colored by mean *sfrp1a:NLS-Eos* intensity (z-scored).

(F) Distribution of mean *sfrp1a:NLS-Eos* intensities (z-scored) for cells in each cell shape cluster. Gray line represents intensity threshold (1 SD) used to label a cell as positive.

(G) UMAP of cells from *atoh1a:mRuby* colored by mean Eos intensity (z-scored).

(H) Polar plot showing relative locations of neuromast cells colored by mean *atoh1a:mRuby* intensity (z-scored).

(I) Distribution of mean *atoh1a:mRuby* intensities (z-scored) for cells in each cell shape cluster. Gray line represents intensity threshold (1 SD) used to label a cell as positive.

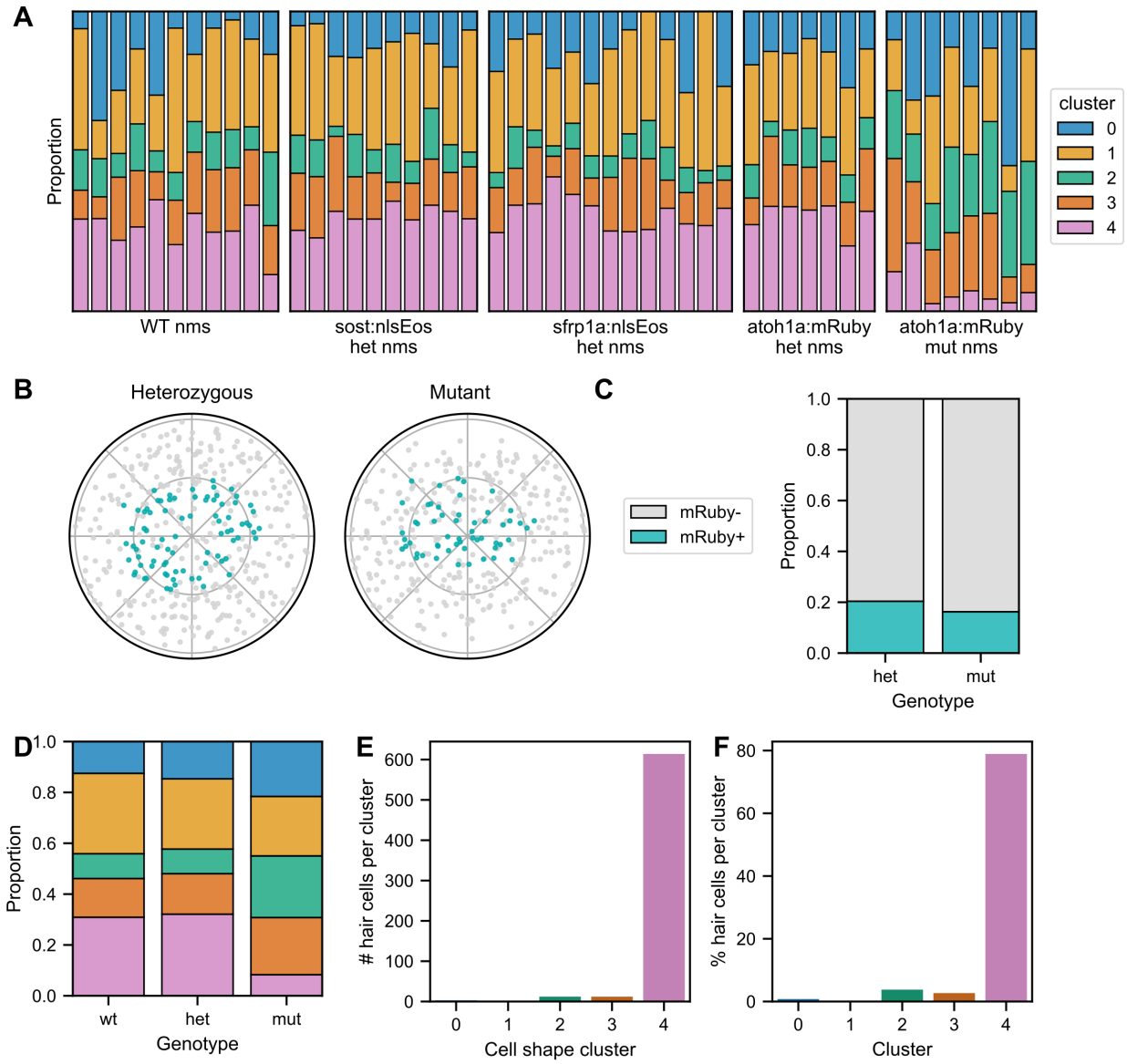

Supplemental Figure 3.15

(A) Proportions of cells in individual neuromasts belonging to each cluster, grouped by reporter expression and genotype (n=49 neuromasts).

(B) Polar plots of relative cell locations of mRuby- cells (gray) and mRuby+ cells (dark cyan) in *atoh1a:mRuby* heterozygotes (left) and *atoh1a:mRuby* mutants (right).

(C) Proportions of mRuby+ cells (dark cyan) and mRuby- cells (gray) in *atoh1a:mRuby* heterozygotes (left bar) and *atoh1a:mRuby* mutants (right bar).

(D) Proportions of cells of each genotype - *atoh1a:mRuby* mutants, heterozygotes, and wildtype - belonging to each cell shape cluster.

(E) Hair cells as raw counts (number) within each cell shape cluster.

(F) Hair cells as a percentage of each cell shape cluster.

batch	reporter	# neuromasts	# cells (pre-filter)	# cells (post-filter)
1	sfrp1a:nlsEos	7	453	383
2	sost:nlsEos	10	824	676
3	sfrp1a:nlsEos	6	459	371
4	atoh1a:mRuby	10	560	496
5	atoh1a:mRuby	5	295	244
6	N/A (wildtype)	11	683	580

Table 1: Summary of the dataset. Each batch represents a separate imaging session. All neuromasts were labeled with DRAQ5 dye in the *Tg(-8.ocldnb:LY-EGFP)* background; the "reporter" column indicates additional genetic labels. "Filter" refers to cells excluded for having high cell shape reconstruction error (see Supplemental Figure 3.9 for details).

CHAPTER 4: SUMMARY OF CODE AND SOFTWARE CREATED

During the course of my studies, I created a number of Python scripts and Jupyter notebooks to perform data processing and analysis. The details of the code are summarized here to acknowledge this product of my work and serve as a reference to future users. Most of the code used for these projects will be available in a public GitHub repository (github.com/raible-lab/neuromast3d). Note that the descriptions here correspond to the code at the time of writing and may not reflect future developments.

4.1 Overview

Most of the code is organized into a Python package called *neuromast3d*. This package is built around the *cvapipe_analysis* package available from the Allen Institute for Cell Science (Viana et al. 2023). It contains code for segmentation, alignment, and preparation of single cell datasets that can be used as inputs to the *cvapipe_analysis* package (which is primarily used to generate the cell-by-SHE coefficients table as well as a list of basic shape features, such as volume, for each cell). The *neuromast3d* package also contains code that can be used for analysis and visualization after spherical harmonics coefficients have been calculated using *cvapipe_analysis*.

The package contains a number of independent modules organized into several directories, most of which correspond to a "step" in the overall processing and analysis pipeline. The first five steps (used for segmentation and dataset preparation) can be run together or separately by setting values in a YAML configuration file. The YAML configuration file is organized into sections corresponding to each step, each of which can be set to run by setting the "state" parameter to True, providing the other required parameters, and using a command that invokes the *run_neuromast3d* runner script with the path to the configuration file. Each of the five steps requires that the previous step has been run (although the alignment step may be

omitted if submitting unaligned cells to the *cvapipe_analysis*). Once these first five steps are complete, the main output is a *manifest.csv* file that contains the path to cropped images for each cell and other metadata associated with an identifier ("CellId") for each cell. The *manifest.csv* can then be submitted to *cvapipe_analysis* (using the *loaddata* and *computefeatures* steps) for calculation of cell shape features. Following *cvapipe_analysis,* modules in the *visualization* directory can be used for subsequent analysis and visualization. Other parts of the package include the *misc* directory, which contains miscellaneous scripts used for tasks like removing unneeded channels from Airyscan images and correcting images for z-drift. Some steps make use of the package napari, which allows for easy creation of graphical user interfaces (GUIs) (Sofroniew et al. 2022). In addition, unit tests are available in the *tests* directory, which are implemented using the *pytest* library. The primary components of the package are summarized in greater detail below.

4.2 Segmentation

The first script here is used for segmenting nuclei and known as *nucleus_segmentation*. This script takes the following as input (provided in the YAML configuration file):

- raw_dir: Directory containing raw (intensity) images.
- mask_dir: Directory containing nucleus mask predictions (i.e. the unthresholded output of a machine learning model trained to detect nuclei).
- nuc_threshold: A float between 0 and 1 corresponding to the desired threshold to be applied to the nucleus mask predictions.
- sigma: An integer corresponding to the size of the kernel used for Gaussian smoothing of the distance transform used for the watershed algorithm.
- min_distance: An integer used to set the minimum distance between seeds during the distance transform watershed.

If the “split_nuclei” functionality (which automatically splits nuclei using membrane boundary predictions) is desired, the following inputs must also be provided:

- boundary_dir: Directory containing membrane predictions (i.e. the unthresholded output of a machine learning model trained to detect cell membranes).
- mem_threshold: A float between 0 and 1 corresponding to the desired threshold to be applied to the membrane predictions.
- mode: Used to control whether nuclei splitting is “automatic” (i.e. wherever the membrane prediction image > mem_threshold, the nucleus mask is set to zero) or “interactive” (which allows the user to define areas where nucleus splitting should be done using the shapes tool in napari).

Upon running the script, the user is presented with a napari window containing a set of magicgui buttons. These buttons allow the user to open raw and ML prediction images, threshold the ML prediction images, split nuclei, run the DT watershed, save the segmentation layer, and clear the viewer of layers. Whenever the user opens an image, the image id (corresponding to the stem of the image filename) is automatically updated. When saving the image, the image id is combined with the layer name to create the name of the saved image.

The second script is used for segmenting cells and is called *dual_channel_annotator*. This script takes the following as input (provided in the YAML configuration file):

- raw_dir: Directory containing raw (intensity) images.
- nuc_labels_dir: Directory containing labeled (segmented) nuclei.
- mem_pred_dir: Directory containing membrane predictions (i.e. the unthresholded output of a machine learning model trained to detect cell membranes).
- output_dir: The desired output directory where the segmentations will be saved.

Similar to the nucleus segmentation script, this script opens a napari window with a number of magicgui buttons. These buttons can be used to open the raw and ML prediction

images, run the seeded watershed, apply a size filter to the segmentation, create watershed lines, and save the segmentations. Both the nuclei and cell segmentations can be edited during this step. When using the "save layers merged" function, the labels layers corresponding to the nuclei and cell segmentations are saved as multichannel image to a single file. The "image id" functionality of preserving file names implemented in the nucleus segmentation script is again used here. The function to open the images includes an option to "open existing labels," which will search the output directory for previously saved segmentations with the given image id. This allows the user to save their progress during segmentation and return to continue refining the annotations.

Note: the segmentation scripts assume that both nuclei and membrane intensity images (and their corresponding ML prediction images) are available. The nucleus segmentation can be run by itself, but the nucleus splitting functionality (which is based on the locations of cell membranes) will not be available. The membrane segmentation script requires labeled nuclei as an input because they are used as markers for the watershed. However, the code could be modified to use other methods of marker generation. Previously, when I segmented images with only the membrane channel, I initially used the local maxima of the distance transform to initially generate point seeds, which I then edited manually using the points tool in napari. However, I found that using labeled nuclei as the markers generally produced higher quality cell segmentation than this older point-based method.

4.3 Preparation of the Single Cell Dataset

This step contains two substeps organized into separate modules: *create_fov_dataset* and *prep_single_cells*. The first, *create_fov_dataset,* takes the following inputs (from the YAML configuration file):

- original_dir: Directory containing the original CZI images. Normally the input images are in TIFF format. Here, the CZI images are provided purely to extract certain metadata (e.g. physical pixel size) which were lost when saving the images as TIFFs in previous steps. Ideally the image metadata would be preserved when the files were converted to TIFFs, so this is a bit of a workaround.
- raw_dir: Directory containing raw (intensity) images.
- seg_dir: Directory containing label images (segmentations), the output of the dual_channel_annotator script.
- project_dir: Desired output directory where the results will be saved. The project directory acts as the root directory for this step, prep_single_cells, and alignment. These steps will save their resulting files and directories with predetermined names within project_dir. Note that all of these steps will also expect the preceding step results used the same project_dir.
- rotate_auto: Whether to rotate the entire neuromast to correct for tilt during image acquisition.
- raw_channel_ids, seg_channel_ids: Dictionaries that contain the name of each channel as keys and their corresponding indices as values. For example, if the raw images contain nuclei in the first channel and membranes in the second channel, the raw_channel_ids might be {nucleus: 0, cell: 1}. Note: the names of the channels used here will persist and eventually be used as column names in cell dataframes in downstream steps, so make sure to pick good names. In addition, cell segmentations are required for the auto_rotate feature and for the alignment script downstream (because they require the cell segmentations be used to create a mask of the whole neuromast). The cell segmentation channel must be named cell_seg.

The script iterates through the list of files and creates a dataframe where every row corresponds to a neuromast and the columns contain the following information: the neuromast id (filename stem), path to the raw image, path to the segmented image, physical pixel size, and the names and indices of the channels in both the raw and segmented images. The dataframe is saved as a CSV file to the specified output directory.

The second part, prep_single_cells, requires that create_fov_dataset has already been run. It takes the following inputs (from the YAML configuration file):

- project_dir: Directory where the results will be saved. See notes above for details.
- raw_channel_ids, seg_channel_ids: Dictionaries that contain the name of each channel as keys and their corresponding indices as values. See notes above for details.

This script uses bilinear interpolation to rescale the raw and segmented images so that they have isotropic voxel dimensions (a requirement for spherical harmonics expansion). It also removes objects with a volume of less than 500 pixels, which are usually artifacts or fragments of cells. After the images have been resized, each individual cell within the neuromast is cropped to a region of interest (ROI) based on the extents of the cell segmentation. Both raw and segmented images are cropped to the same ROI. The single cell raw and segmented images are saved within nested directories in project_dir that correspond to the neuromast ID and cell label number (i.e. the integer that identifies the cell in the segmented image). Associated metadata for each cell, including the paths to the cropped single cell images, are saved in a manifest.csv file.

4.4 Alignment

The module for the alignment step is called *nm_alignment_basic*. It requires that *prep_single_cells* has already been run. It takes the following as inputs (from the YAML configuration file):

- project_dir: Directory where the results will be saved. See notes above for details.

- rot_ch_index: The index of the channel in the segmented image to use to calculate the radial rotation angle (the first rotation in the series of three used to align the cells). The cell segmentation channel is used to calculate the neuromast centroid, while the channel indicated here is used to indicate which channel should be used to calculate the cell centroid. This allows the user to choose whether to use the cell or the nucleus to calculate the cell centroid.
- mode: The rotation strategy to use. The following are available:
    - *unaligned:* No alignment is applied.
    - *xy_only:* Only the radial alignment is applied.
    - *xy_xz:* Radial alignment is applied, followed by alignment of the long axis in the xz plane to the z-axis.
    - *xy_xz_yz:* Radial alignment is applied, followed by alignment of the long axis in the xz plane to the z-axis, followed by alignment of the long axis in the yz plane to the z-axis.
    - principal_axes: PCA is used to calculate the principal axes of the cell. All cells are aligned such that their first three principal axes are aligned to the x, y, and z coordinates.
- use_channels: The index of the channel to be used to calculate the rotation angles (aside from the radial rotation angle, which uses the channel specified by rot_ch_index). Note: multiple channels can be specified here, which is to reproduce an older behavior where the code (unintentionally) used all available segmentation channels to calculate the alignment angles.
- 45_corr: For xz and yz rotations, whether to apply a correction such that if the rotation to the vertical (z) axis would be >45 degrees, align with the horizontal (x or y) axis instead.

4.5 Visualization

This directory contains scripts used for data analysis and visualization. It is intended to be run after the preprocessing pipeline (segmentation, preparation of the single cell dataset, and alignment) and necessary cvapipe_analysis steps (loaddata and compute features) have been run. Visualization modules include:

- curate_fov: A script used to open the field of view (fov) raw and segmented images for an experiment and pick labels to be excluded (such as poorly segmented cells). Includes an option to indicate the neuromast polarity relative to the body axis (AP or DV). Information is saved as a CSV file. Implemented using napari and magicgui.
- rec_error: A script that can automatically calculate error metrics (such as Hausdorff distance) for the original and reconstructed meshes for an experiment. Results are saved in a CSV file.
- *analysis:* A script that takes the outputs from proceeding steps and organizes them in an AnnData object (Virshup et al. 2021), which is then saved. Can exclude manually annoted cells by providing output from *curate_fov*.
- plotting_tools: Module with a variety of functions used for data analysis and plotting.
- visualization: A script that allows the user to display data in UMAP space and pick points to open the corresponding single cell images. Useful for exploratory data analysis.

4.5 Miscellaneous

Other modules include:

- *find_closest_cells:* Contains a class called "RepresentativeCellFinder," which inherits from scipy.spatial.KDTree (Gommers et al. 2023). Used to find representative cells (i.e. the cells closest to cluster centroids in multidimensional space).

- split_channels: A simple script used to automatically remove channels from an image that are not needed for analysis, such as “preview” channels on an AiryScan image.
- *stackreg_script:* A script that can be used to efficiently register images in batches using the pystackreg package (the Python port of the FIJI plugin StackReg) (Thevenaz et al. 1998).

CHAPTER 5: CONCLUSIONS AND FUTURE DIRECTIONS

In this dissertation, I explored the relationship between cell shape and fate/identity in zebrafish lateral line neuromasts. I successfully applied spherical harmonics and PCA to morphologically profile neuromast cells (Chapter 3). As a result, I found that hair cells have a quantifiable and distinct morphological phenotype and can be classified using cell shape features. Using transgenic lines that label support cell subpopulations, I also discovered that peripheral support cells and dorsoventral support cells have characteristic cell shapes. In addition, *atoh1a* mutants (which lack hair cells) exhibit loss of the hair cell shape phenotype and shifts in support cell shape phenotypes. As part of this work, I also integrated cutting-edge libraries for segmentation and data analysis/visualization into a streamlined Python package (Chapter 4). Together, these results and resources provide a useful foundation for future studies quantifying cell and nuclear shape phenotypes in neuromasts (and beyond). In the following sections, I discuss potential future avenues of investigation building off of this work.

5.1 From 3D to 4D: Adding the Temporal Dimension

In my work, I used an information-rich shape representation to quantify neuromast cell shape in 3D, which represents a significant advancement over past methods that relied on 2D projections or simple geometric measurements. A logical next step would be to add another dimension: time. In my studies, I only looked at one point in developmental time (5 dpf) and did not quantify how cell shape changes over time. Although it is possible to make some predictions from my data about how cell shape might change as cells transition through certain lineages (e.g. from a DV support cell to a hair cell), to address this question more thoroughly requires time lapse experiments.

There are several exciting questions related to cell shape dynamics in neuromasts. For example, how do cells change shape during development? My work examined cell shape in 5 dpf

neuromasts, while Hartmann and colleagues (2020) quantified cell shape in the posterior lateral line primordium (the migratory collective of cells that gives rise to neuromasts of the posterior lateral line) at 32-36 hpf. Comparing these studies provides some hints about how cell shape might change during development. However, many questions remain. What happens between these two time points? Do support cells resemble primordium cells, or do they change in shape as the neuromast develops? How do the shapes of individual cells evolve they transition between support cell identities, divide, and/or differentiate into hair cells? These questions could be addressed by imaging *Tg(cldnb:LY-EGFP)* fish over time. Ideally, studies would be performed longitudinally (by imaging the same neuromasts at multiple time points) so individual cells can be tracked as they go through developmental trajectories. It would be interesting to image posterior lateral line neuromasts starting at their initial deposition by the primordium (~1-2 dpf) up until they reach functional maturity (5 dpf). This time course would elucidate how neuromast cell shapes change as progenitor cells divide and differentiate as hair cells.

3D cell shape analysis could also be applied to understand how support cells change shape when hair cells die. During hair cell death, support cells form apical F-actin cables that surround the dying hair cell and close around it (Bird et al. 2010). Comparative studies have suggested that differences in support cell adhesions and cytoskeletal structures may render them less dynamic in adult mammals, which has been cited as a possible explanation for their lessened regenerative capacity compared to non-mammalian vertebrates (Burns et al. 2008, 2013). Could support cell shape change during hair cell death act as a "death signal" that induces proliferation and regeneration? To answer this question, it is first necessary to demonstrate that support cell shape dynamics during hair cell death are quantifiably different between species, which could be addressed using 3D shape analysis. In zebrafish neuromasts, support cell shape dynamics during hair cell death could be observed by performing time lapse imaging of *Tg(cldnb:LY-EGFP)* zebrafish treated with an ototoxic drug such as neomycin. In preliminary

experiments, I found that treating fish with 50 micromolar neomycin and imaging them over the course of an hour worked well to reliably induce at least one hair cell death event without causing too many hair cells to die at once (which can make the data harder to interpret). Alternatively, a single hair cell could be targeted for death using laser ablation or by scatter labeling with rat TrpV1 channels and applying capsaicin (Chen et al. 2016). This targeted approach would enable precise quantification of the responses to a single cell dying, avoiding potential confounds from multiple dying cells at once. Single cell ablation experiments would enable comparisons in support cell shape changes at various distances from the dying cell, providing data about how far hair cell death is "felt" by support cells from a physical perspective. Similar studies could be done in other species to quantify and compare shape changes in both regenerative and non-regenerative species. 3D cell shape analysis could also be used to generate reconstructions and models of support cell shape transitions during hair cell death, allowing more precise quantification and visualization of how these events typically occur in different species.

Once support cell shape dynamics during hair cell death have been established, the next logical step would be to study shape change during hair cell regeneration. High concentrations of neomycin could be applied to *Tg(cldnb:LY-EGFP)* zebrafish, which could then be imaged at multiple time points over the course of regeneration (which takes approximately 2-3 days to complete). If combined with time lapse imaging during hair cell death, it would be possible to determine whether support cell shape change is correlated with proliferation. By tracking cell shapes as they divide and differentiate, it could be possible to determine the shape characteristics of hair cell progenitors and perhaps even train a shape-based classifier to detect them, although many images would likely be necessary to train a good classifier. Quantifying cell shape change during regeneration could provide insight into whether regenerative cell shape dynamics recapitulate development or if there are cell shape states unique to regeneration. Cell

shape modeling could also facilitate deeper investigation into how mechanical forces might regulate regeneration in neuromasts.

I foresee two technical hurdles to timelapse studies of cell shape in neuromasts. First, imaging would need to be done live, at high spatial resolution, and across multiple time points while avoiding phototoxicity and photobleaching. Although my studies demonstrate that live imaging of neuromasts at sufficiently high spatial resolution is feasible for a single time point, adding additional time points may be challenging. The z-stacks acquired for my analysis in Chapter 3, which had multiple channels and were optimized for spatial resolution, could take 10-30 minutes to acquire on the microscope I was using (a Zeiss LSM 880 with AiryScan). The high requirement for spatial resolution might limit temporal resolution, although improved hardware, deconvolution, or content aware image restoration (Weigert et al. 2018) may help to address this issue. Second, a 3D cell tracking algorithm would need to be implemented so that the shape evolution of single cells could be followed over time. Because some of the proposed studies involve cell division and death, thereby changing the number of cells in the field of view, I anticipate that automated tracking of cells could be difficult without some level of manual supervision. A deep learning-based platform such as ELEPHANT, which incorporates human annotation to incrementally improve model performance, could be a potential solution (Sugawara et al. 2022).

5.2 Integrating Cell Shape and Gene Expression Data

In my work, I used transgenic knock-in lines to label and characterize the shapes of support cell subpopulations within neuromasts. An advantage of transgenic lines is that they can be used in live imaging experiments, which will likely be useful for the time lapse experiments discussed above. However, there is a limited number of transgenic lines currently available that label neuromast cell subpopulations, and new transgenic lines can be difficult and time-

consuming to create. An alternative would be to label cell subpopulations using RNA fluorescent *in situ* hybridization (FISH). FISH could be useful for characterizing the morphologies of additional cell states and types for which transgenic lines are not yet available. In addition, FISH could guide the creation of new transgenic lines as new genes with interesting patterns are identified, which could then be used for live imaging studies.

There is already a strong foundation for integrating gene expression with cell shape in the lab. Our lab has successfully developed a protocol to apply *in situ* hybridization chain reaction (HCR) to zebrafish neuromasts, which allows RNA transcripts to be quantified at subcellular resolution (Choi et al. 2018). *In situ* HCR labeling produces fluorescent spots corresponding to single RNA molecules that can be detected using confocal microscopy. Preliminary work together with Iván Cruz has demonstrated that the tools I developed for segmentation in my work can be adapted to fixed images of *Tg(cldnb:LY-EGFP)* fish stained with DAPI and an HCR probe. Additionally, I have observed that the Allen Cell and Structure Segmenter (Chen et al. 2018) can be used to detect and segment spots produced by HCR in images of neuromasts. Once the cells and HCR spots have been segmented, the cell shape analysis pipeline can likely be applied in a similar manner to my work on live images. Segmented HCR spots could be assigned to individual cells, allowing for quantification of transcript expression in each cell. Using this method, relationships between cell shape features and transcript expression could theoretically be established for any gene that can be labeled using HCR. Creating this sort of "atlas" of cell shape and gene expression has many potential applications, including building predictive models of gene expression from cell shape features and investigating genetic regulation of cell shape.

Which genes are likely to have interesting patterns and cell shape phenotypes remains an open question. However, one promising candidate is *her9,* a gene that Iván Cruz has extensively investigated. *her9* is expressed specifically in central support cells that lie underneath hair cells

and interdigitate between them. In my work, I did not investigate any markers specific to central support cells, although I expect they would have distinct shape features due to their proximity to hair cells and thin apical projections. A marker for central support cells would also provide insight into why these cells did not appear to form a distinct cluster in the shape analysis study I described in Chapter 3. Given that many central support cells have thin, concave projections, some of them were likely discarded due to high reconstruction error. Others may have been assigned to cell shape clusters (such as cluster 3), but it is difficult to ascertain the distribution of central support cells across clusters without a label for these cells. Looking at *her9*-expressing cells would serve to address this current gap. Another potential candidate is *fgfr3,* a gene identified in a single cell RNA-sequencing study that also labels central support cells (Lush et al. 2019). I expect that mining RNA-seq studies for other candidates will be fruitful, and could serve to further establish the link between gene transcription and cell shape. Eventually, spatial transcriptomics may enable high-dimensional morphological and transcriptional profiling of the same cells, greatly enhancing our ability to identify genes associated with morphological features and providing deeper insights into the relationships between cell shape, fate, and spatial context.

5.3 Analysis of Organ Shape

In a sense, the shape of an organ can be thought of as the sum of shapes of the cells within it. As cells change shape, they deform the shapes of cells around them, and coordinated movements of cells can determine the shapes of organs during morphogenesis. However, organs also impose boundaries and constrain the shapes of individual cells. Understanding the relationships between individual cell shape and organ shape can inform how growth is coordinated across scales during development.

The zebrafish lateral line is made up of many neuromasts at distinct locations on the surface of the fish. In zebrafish, neuromasts are added in multiple waves during embryonic and postembryonic devleopment (Nuñez et al. 2009). The first neuromasts on the trunk of the body (known as the posterior lateral line, or pLL) are added by a collectively migrating group of cells called the primordium (primI). A second set of pLL neuromasts is deposited by a second primordium, known as primII. Additional neuromasts, known as intercalary neuromasts, originate from proliferation and aggregation of interneuromast cells (Grant et al. 2005). Compared to the pLL, the development of neuromasts on the head (known as the anterior lateral line, or aLL) has been less extensively studied. However, it has been shown that during embryonic development, aLL neuromasts are added through a variety of mechanisms, including collective migration, budding, and division of interneuromast cells (Iwasaki et al. 2020). In later stages of life, additional neuromasts are formed from cells budding off of the periphery of existing neuromasts, forming structrues known as "stitches" (Nuñez et al. 2009). In this way, neuromasts on both the head and the trunk arise from several different mechanisms.

The age, location, and mechanism of formation of each neuromast likely has consequences on the overall shape of the organ. In my thesis work, I looked at aLL neuromasts, and noticed some differences in the shape and size of different neuromasts. For example, the MI1 neuromast, which lies on top of the round, bony ear, appeared to be flattened along the z-axis and more "spread out," as if stretched across the surface of the ear. Many neuromasts also appeared to have pairs of peripheral support cells that formed a "triangle" where the edge of the neuromast meets the chain of interneuromast cells. The location of these "triangles" may depend on how the neuromast was originally formed. To understand variation in neuromast organ shape, a similar analysis pipeline as that used for cells could be applied: whole neuromasts could be segmented, aligned, and subjected to spherical harmonics and PCA. The shapes of different neuromasts could then be quantified and compared. If done in tandem with

cell shape analysis, it would be possible to determine whether differences in neuromast shape are associated with differences in individual cell shape.

Organ shape could also be analyzed in the context of genetic mutants and other perturbations. For example, I anecdotally observed that neuromasts in *atoh1a* mutants (which lack hair cells) appeared to be flatter and have reduced apical surface area compared to their wildtype counterparts. However, I did not have a large enough sample of individual neuromasts to test this potential effect of *atoh1a* mutation. Other pathways that regulate the number and proportions of neuromast cell types could also be manipulated to investigate their effects on neuromast shape. For example, effects on organ shape due to inhibiting Notch signaling (which increases the number of hair cells at the expense of support cells) could be compared to those caused by inhibiting Wnt signaling (which causes the neuromast to increase in size without altering cell type proportions) (Haddon et al. 1998; Itoh and Chitnis 2001; Head et al. 2013; Jacques et al. 2014). These studies could further elucidate how organ shape is affected when certain cell types are either lost or present in abnormal proportions.

Additionally, combined cell and organ shape analysis could shed light on the "rules" of how neuromasts form and become organized. Studies in which large portions of neuromasts were ablated have shown that only a few cells need to be present to regenerate a neuromast with normal numbers, proportions, and relative locations of cells (Seleit et al. 2017; Viader-Llargués et al. 2018). How neuromasts accomplish this feat remains unknown. It is possible that density and shape cues may be involved in regulating cell proliferation and differentiation so that regenerative "overshoot" does not occur. By combining large scale ablation with cell and organ shape analysis, the evolution of shape over time in individual cells and organs could be studied to identify how the structure of a neuromast emerges from cell shape changes, movements, and divisions.

REFERENCES

Abzhanov A, Protas M, Grant BR, et al (2004) Bmp4 and Morphological Variation of Beaks in Darwin's Finches. Science 305:1462–1465. https://doi.org/10.1126/science.1098095

Adler HJ, Raphael Y (1996) New hair cells arise from supporting cell conversion in the acoustically damaged chick inner ear. Neuroscience Letters 205:17–20. https://doi.org/10.1016/0304-3940(96)12367-3

Ahrens J, Geveci B, Law C (2005) ParaView: An End-User Tool for Large-Data Visualization. In: Visualization Handbook. Elsevier, pp 717–731

Alvarado DM, Hawkins RD, Bashiardes S, et al (2011) An RNA Interference-Based Screen of Transcription Factor Genes Identifies Pathways Necessary for Sensory Regeneration in the Avian Inner Ear. J Neurosci 31:4535–4543. https://doi.org/10.1523/JNEUROSCI.5456-10.2011

Andrews TGR, Pönisch W, Paluch EK, et al (2021) Single-cell morphometrics reveals ancestral principles of notochord development. Development 148:dev199430. https://doi.org/10.1242/dev.199430

Avallone B, Porritiello M, Esposito D, et al (2003) Evidence for hair cell regeneration in the crista ampullaris of the lizard Podarcis sicula. Hearing Research 178:79–88. https://doi.org/10.1016/S0378-5955(03)00040-6

Bai H, Yang S, Xi C, et al (2021) Signaling pathways (Notch, Wnt, Bmp and Fgf) have additive effects on hair cell regeneration in the chick basilar papilla after streptomycin injury in vitro: Additive effects of signaling pathways on hair cell regeneration. Hear Res 401:108161. https://doi.org/10.1016/j.heares.2020.108161

Baird RA, Steyger PS, Schuff NR (1996) Mitotic and Nonmitotic Hair Cell Regeneration in the Bullfrog Vestibular Otolith Organsa. Annals of the New York Academy of Sciences 781:59–70. https://doi.org/10.1111/j.1749-6632.1996.tb15693.x

Baird RA, Torres MA, Schuff NR (1993) Hair cell regeneration in the bullfrog vestibular otolith organs following aminoglycoside toxicity. Hearing Research 65:164–174. https://doi.org/10.1016/0378-5955(93)90211-I

Balak KJ, Corwin JT, Jones JE (1990) Regenerated hair cells can originate from supporting cell progeny: evidence from phototoxicity and laser ablation experiments in the lateral line system. J Neurosci 10:2502–2512. https://doi.org/10.1523/JNEUROSCI.10-08-02502.1990

Barnhart EL, Lee K-C, Keren K, et al (2011) An Adhesion-Dependent Switch between Mechanisms That Determine Motile Cell Shape. PLOS Biology 9:e1001059. https://doi.org/10.1371/journal.pbio.1001059

Behra M, Bradsher J, Sougrat R, et al (2009) Phoenix Is Required for Mechanosensory Hair Cell Regeneration in the Zebrafish Lateral Line. PLOS Genetics 5:e1000455. https://doi.org/10.1371/journal.pgen.1000455

Behra M, Gallardo VE, Bradsher J, et al (2012) Transcriptional signature of accessory cells in the lateral line, using the Tnk1bp1:EGFP transgenic zebrafish line. BMC Developmental Biology 12:6. https://doi.org/10.1186/1471-213X-12-6

Benham-Pyle BW, Pruitt BL, Nelson WJ (2015) Mechanical strain induces E-cadherin–dependent Yap1 and β-catenin activation to drive cell cycle entry. Science 348:1024–1027. https://doi.org/10.1126/science.aaa4559

Bermingham NA, Hassan BA, Price SD, et al (1999) Math1: An Essential Gene for the Generation of Inner Ear Hair Cells. Science 284:1837–1841. https://doi.org/10.1126/science.284.5421.1837

Bermingham-McDonogh O, Rubel EW (2003) Hair cell regeneration: winging our way towards a sound future. Current Opinion in Neurobiology 13:119–126. https://doi.org/10.1016/S0959-4388(03)00018-7

Beucher S, Lantuéjoul C (1979) Use of Watersheds in Contour Detection. In: Proceedings of the International workshop on image processing, real-time edge and motion detection. CCETT, Rennes, France

Bird JE, Daudet N, Warchol ME, Gale JE (2010) Supporting cells eliminate dying sensory hair cells to maintain epithelial integrity in the avian inner ear. J Neurosci 30:12545–12556. https://doi.org/10.1523/JNEUROSCI.3042-10.2010

Bradford YM, Van Slyke CE, Ruzicka L, et al (2022) Zebrafish information network, the knowledgebase for Danio rerio research. Genetics 220:iyac016. https://doi.org/10.1093/genetics/iyac016

Breitzler L, Lau IH, Fonseca PJ, Vasconcelos RO (2020) Noise-induced hearing loss in zebrafish: investigating structural and functional inner ear damage and recovery. Hearing Research 391:107952. https://doi.org/10.1016/j.heares.2020.107952

Breuskin I, Bodson M, Thelen N, et al (2008) Strategies to regenerate hair cells: identification of progenitors and critical genes. Hearing Research 236:1–10. https://doi.org/10.1016/j.heares.2007.08.007

Brignull HR, Raible DW, Stone JS (2009) Feathers and fins: Non-mammalian models for hair cell regeneration. Brain Research 1277:12–23. https://doi.org/10.1016/j.brainres.2009.02.028

Brown EM, Toloudis D, Sherman J, et al (2021) AICSImageIO: Image Reading, Metadata Conversion, and Image Writing for Microscopy Images in Pure Python. GitHub. https://github.com/AllenCellModeling/aicsimageio

Burns J, Christophel JJ, Collado MS, et al (2008) Reinforcement of cell junctions correlates with the absence of hair cell regeneration in mammals and its occurrence in birds. Journal of Comparative Neurology 511:396–414. https://doi.org/10.1002/cne.21849

Burns JC, Collado MS, Oliver ER, Corwin JT (2013) Specializations of intercellular junctions are associated with the presence and absence of hair cell regeneration in ears from six vertebrate classes. Journal of Comparative Neurology 521:1430–1448. https://doi.org/10.1002/cne.23250

Burns JC, Corwin JT (2014) Responses to Cell Loss Become Restricted as the Supporting Cells in Mammalian Vestibular Organs Grow Thick Junctional Actin Bands That Develop High Stability. J Neurosci 34:1998–2011. https://doi.org/10.1523/JNEUROSCI.4355-13.2014

Butler LC, Blanchard GB, Kabla AJ, et al (2009) Cell shape changes indicate a role for extrinsic tensile forces in Drosophila germ-band extension. Nat Cell Biol 11:859–864. https://doi.org/10.1038/ncb1894

Cafaro J, Lee GS, Stone JS (2007) Atoh1 expression defines activated progenitors and differentiating hair cells during avian hair cell regeneration. Developmental Dynamics 236:156–170. https://doi.org/10.1002/dvdy.21023

Campàs O, Mallarino R, Herrel A, et al (2010) Scaling and shear transformations capture beak shape variation in Darwin's finches. Proc Natl Acad Sci U S A 107:3356–3360. https://doi.org/10.1073/pnas.0911575107

Carey JP, Fuchs AF, Rubel EW (1996) Hair cell regeneration and recovery of the vestibuloocular reflex in the avian vestibular system. Journal of Neurophysiology. https://doi.org/10.1152/jn.1996.76.5.3301

Chan CJ, Heisenberg C-P, Hiiragi T (2017) Coordination of Morphogenesis and Cell-Fate Specification in Development. Current Biology 27:R1024–R1035. https://doi.org/10.1016/j.cub.2017.07.010

Chen CS, Mrksich M, Huang S, et al (1997) Geometric Control of Cell Life and Death. Science 276:1425–1428. https://doi.org/10.1126/science.276.5317.1425

Chen J, Ding L, Viana MP, et al (2018) The Allen Cell and Structure Segmenter: a new open source toolkit for segmenting 3D intracellular structures in fluorescence microscopy images. Cell Biology. BioRxiv (Preprint). https://doi.org/10.1101/491035

Chen S, Chiu CN, McArthur KL, et al (2016) TRP channel mediated neuronal activation and ablation in freely behaving zebrafish. Nat Methods 13:147–150. https://doi.org/10.1038/nmeth.3691

Chitnis AB, Nogare DD, Matsuda M (2012) Building the posterior lateral line system in zebrafish. Dev Neurobiol 72:234–255. https://doi.org/10.1002/dneu.20962

Choi HMT, Schwarzkopf M, Fornace ME, et al (2018) Third-generation in situ hybridization chain reaction: multiplexed, quantitative, sensitive, versatile, robust. Development 145:dev165753. https://doi.org/10.1242/dev.165753

Chrysostomou E, Zhou L, Darcy YL, et al (2020) The Notch Ligand Jagged1 Is Required for the Formation, Maintenance, and Survival of Hensen's Cells in the Mouse Cochlea. J Neurosci 40:9401–9413. https://doi.org/10.1523/JNEUROSCI.1192-20.2020

Coffin AB, Mohr RA, Sisneros JA (2012) Saccular-Specific Hair Cell Addition Correlates with Reproductive State-Dependent Changes in the Auditory Saccular Sensitivity of a Vocal Fish. J Neurosci 32:1366–1376. https://doi.org/10.1523/JNEUROSCI.4928-11.2012

Corwin JT (1985) Perpetual production of hair cells and maturational changes in hair cell ultrastructure accompany postembryonic growth in an amphibian ear. PNAS 82:3911–3915. https://doi.org/10.1073/pnas.82.11.3911

Corwin JT (1981) Postembryonic production and aging of inner ear hair cells in sharks. Journal of Comparative Neurology 201:541–553. https://doi.org/10.1002/cne.902010406

Corwin JT, Cotanche DA (1988) Regeneration of Sensory Hair Cells After Acoustic Trauma. Science 240:1772–1774. https://doi.org/10.1126/science.3381100

Cotanche DA (1987) Regeneration of hair cell stereociliary bundles in the chick cochlea following severe acoustic trauma. Hearing Research 30:181–195. https://doi.org/10.1016/0378-5955(87)90135-3

Cotanche DA, Kaiser CL (2010) Hair cell fate decisions in cochlear development and regeneration. Hearing Research 266:18–25. https://doi.org/10.1016/j.heares.2010.04.012

Cruz IA, Kappedal R, Mackenzie SM, et al (2015) Robust regeneration of adult zebrafish lateral line hair cells reflects continued precursor pool maintenance. Developmental Biology 402:229–238. https://doi.org/10.1016/j.ydbio.2015.03.019

Dalmasso G, Musy M, Niksic M, et al (2022) 4D reconstruction of murine developmental trajectories using spherical harmonics. Developmental Cell 57:2140-2150.e5. https://doi.org/10.1016/j.devcel.2022.08.005

Daudet N, Gibson R, Shang J, et al (2009) Notch regulation of progenitor cell behavior in quiescent and regenerating auditory epithelium of mature birds. Developmental Biology 326:86–100. https://doi.org/10.1016/j.ydbio.2008.10.033

De Vries M, Dent L, Curry N, et al (2022) 3D single-cell shape analysis using geometric deep learning. BioRxiv (Preprint). https://doi.org/10.1101/2022.06.17.496550

Dickman JD, Lim I (2004) Posture, Head Stability, and Orientation Recovery During Vestibular Regeneration In Pigeons. JARO 5:323–336. https://doi.org/10.1007/s10162-004-4047-0

Doetzlhofer A, Avraham KB (2017) Insights into inner ear-specific gene regulation: Epigenetics and non-coding RNAs in inner ear development and regeneration. Seminars in Cell & Developmental Biology 65:69–79. https://doi.org/10.1016/j.semcdb.2016.11.002

Dooling RJ, Ryals BM, Manabe K (1997) Recovery of hearing and vocal behavior after hair-cell regeneration. PNAS 94:14206–14210. https://doi.org/10.1073/pnas.94.25.14206

Dufourcq P, Roussigné M, Blader P, et al (2006) Mechano-sensory organ regeneration in adults: The zebrafish lateral line as a model. Molecular and Cellular Neuroscience 33:180–187. https://doi.org/10.1016/j.mcn.2006.07.005

Faucherre A, Pujol-Martí J, Kawakami K, López-Schier H (2009) Afferent Neurons of the Zebrafish Lateral Line Are Strict Selectors of Hair-Cell Orientation. PLOS ONE 4:e4477. https://doi.org/10.1371/journal.pone.0004477

Fritz JA, Brancale J, Tokita M, et al (2014) Shared developmental programme strongly constrains beak shape diversity in songbirds. Nat Commun 5:3700. https://doi.org/10.1038/ncomms4700

Frucht CS, Santos-Sacchi J, Navaratnam DS (2011) MicroRNA181a plays a key role in hair cell regeneration in the avian auditory epithelium. Neuroscience Letters 493:44–48. https://doi.org/10.1016/j.neulet.2011.02.017

Frucht CS, Uduman M, Duke JL, et al (2010) Gene Expression Analysis of Forskolin Treated Basilar Papillae Identifies MicroRNA181a as a Mediator of Proliferation. PLOS ONE 5:e11502. https://doi.org/10.1371/journal.pone.0011502

Gerbin KA, Grancharova T, Donovan-Maiye RM, et al (2021) Cell states beyond transcriptomics: Integrating structural organization and gene expression in hiPSC-derived cardiomyocytes. Cell Systems 12:670-687.e10. https://doi.org/10.1016/j.cels.2021.05.001

Gerig G, Styner M, Jones D, et al (2001) Shape analysis of brain ventricles using SPHARM. In: Proceedings IEEE Workshop on Mathematical Methods in Biomedical Image Analysis (MMBIA 2001). pp 171–178

Giffen KP, Liu H, Kramer KL, He DZ (2019) Expression of Protein-Coding Gene Orthologs in Zebrafish and Mouse Inner Ear Non-sensory Supporting Cells. Front Neurosci 13:. https://doi.org/10.3389/fnins.2019.01117

Gnedeva K, Jacobo A, Salvi JD, et al (2017) Elastic force restricts growth of the murine utricle. eLife Sciences 6:e25681. https://doi.org/10.7554/eLife.25681

Gnedeva K, Wang X, McGovern MM, et al (2020) Organ of Corti size is governed by Yap/Tead-mediated progenitor self-renewal. Proc Natl Acad Sci USA 117:13552–13561. https://doi.org/10.1073/pnas.2000175117

Goman AM, Lin FR (2016) Prevalence of Hearing Loss by Severity in the United States. Am J Public Health 106:1820–1822. https://doi.org/10.2105/AJPH.2016.303299

Gommers R, Virtanen P, Burovski E, et al (2023) scipy/scipy: SciPy 1.10.1. https://doi.org/10.5281/zenodo.7655153

Goode CT, Carey JP, Fuchs AF, Rubel EW (1999) Recovery of the Vestibulocolic Reflex After Aminoglycoside Ototoxicity in Domestic Chickens. Journal of Neurophysiology. https://doi.org/10.1152/jn.1999.81.3.1025

Gou Y, Guo J, Maulding K, Riley BB (2018a) sox2 and sox3 cooperate to regulate otic/epibranchial placode induction in zebrafish. Developmental Biology 435:84–95. https://doi.org/10.1016/j.ydbio.2018.01.011

Gou Y, Vemaraju S, Sweet EM, et al (2018b) sox2 and sox3 Play unique roles in development of hair cells and neurons in the zebrafish inner ear. Developmental Biology 435:73–83. https://doi.org/10.1016/j.ydbio.2018.01.010

Grant KA, Raible DW, Piotrowski T (2005) Regulation of Latent Sensory Hair Cell Precursors by Glia in the Zebrafish Lateral Line. Neuron 45:69–80. https://doi.org/10.1016/j.neuron.2004.12.020

Haas P, Gilmour D (2006) Chemokine Signaling Mediates Self-Organizing Tissue Migration in the Zebrafish Lateral Line. Developmental Cell 10:673–680. https://doi.org/10.1016/j.devcel.2006.02.019

Haddon C, Jiang YJ, Smithers L, Lewis J (1998) Delta-Notch signalling and the patterning of sensory cell differentiation in the zebrafish ear: evidence from the mind bomb mutant. Development 125:4637–4644

Haque A, Zakir M, Dickman JD (2009) Regeneration of Vestibular Horizontal Semicircular Canal Afferents in Pigeons. J Neurophysiol 102:1274–1286. https://doi.org/10.1152/jn.91000.2008

Harding MJ, Nechiporuk AV (2012) Fgfr-Ras-MAPK signaling is required for apical constriction via apical positioning of Rho-associated kinase during mechanosensory organ formation. Development 139:3130–3135. https://doi.org/10.1242/dev.082271

Hardy K, Amariutei AE, De Faveri F, et al (2021) Functional development and regeneration of hair cells in the zebrafish lateral line. The Journal of Physiology 599:3913–3936. https://doi.org/10.1113/JP281522

Harris JA, Cheng AG, Cunningham LL, et al (2003) Neomycin-Induced Hair Cell Death and Rapid Regeneration in the Lateral Line of Zebrafish (Danio rerio). JARO 4:219–234. https://doi.org/10.1007/s10162-002-3022-x

Hartmann J, Wong M, Gallo E, Gilmour D (2020) An image-based data-driven analysis of cellular architecture in a developing tissue. eLife 9:e55913. https://doi.org/10.7554/eLife.55913

Hawkins RD, Bashiardes S, Helms CA, et al (2003) Gene expression differences in quiescent versus regenerating hair cells of avian sensory epithelia: implications for human hearing and balance disorders. Hum Mol Genet 12:1261–1272. https://doi.org/10.1093/hmg/ddg150

Hawkins RD, Bashiardes S, Powder KE, et al (2007) Large Scale Gene Expression Profiles of Regenerating Inner Ear Sensory Epithelia. PLoS One 2:. https://doi.org/10.1371/journal.pone.0000525

He Y, Cai C, Tang D, et al (2014) Effect of histone deacetylase inhibitors trichostatin A and valproic acid on hair cell regeneration in zebrafish lateral line neuromasts. Front Cell Neurosci 8:. https://doi.org/10.3389/fncel.2014.00382

He Y, Tang D, Cai C, et al (2016) LSD1 is Required for Hair Cell Regeneration in Zebrafish. Mol Neurobiol 53:2421–2434. https://doi.org/10.1007/s12035-015-9206-2

He Y, Yu H, Sun S, et al (2013) Trans-2-phenylcyclopropylamine regulates zebrafish lateral line neuromast development mediated by depression of LSD1 activity. Int J Dev Biol 57:365–373. https://doi.org/10.1387/ijdb.120227hl

Head JR, Gacioch L, Pennisi M, Meyers JR (2013) Activation of canonical Wnt/β-catenin signaling stimulates proliferation in neuromasts in the zebrafish posterior lateral line. Developmental Dynamics 242:832–846. https://doi.org/10.1002/dvdy.23973

Hernández PP, Olivari FA, Sarrazin AF, et al (2007) Regeneration in zebrafish lateral line neuromasts: Expression of the neural progenitor cell marker sox2 and proliferation-dependent and-independent mechanisms of hair cell renewal. Developmental Neurobiology 67:637–654. https://doi.org/10.1002/dneu.20386

Huff J (2015) The Airyscan detector from ZEISS: confocal imaging with improved signal-to-noise ratio and super-resolution. Nat Methods 12:i–ii. https://doi.org/10.1038/nmeth.f.388

Huttenlocher DP, Klanderman GA, Rucklidge WJ (1993) Comparing images using the Hausdorff distance. IEEE Transactions on Pattern Analysis and Machine Intelligence 15:850–863. https://doi.org/10.1109/34.232073

Itoh M, Chitnis AB (2001) Expression of proneural and neurogenic genes in the zebrafish lateral line primordium correlates with selection of hair cell fate in neuromasts. Mechanisms of Development 102:263–266. https://doi.org/10.1016/S0925-4773(01)00308-2

Iwasaki M, Yokoi H, Suzuki T, et al (2020) Development of the anterior lateral line system through local tissue-tissue interactions in the zebrafish head. Developmental Dynamics 249:1440–1454. https://doi.org/10.1002/dvdy.225

Jacobo A, Dasgupta A, Erzberger A, et al (2019) Notch-Mediated Determination of Hair-Bundle Polarity in Mechanosensory Hair Cells of the Zebrafish Lateral Line. Current Biology 29:3579-3587.e7. https://doi.org/10.1016/j.cub.2019.08.060

Jacques BE, Montgomery WH, Uribe PM, et al (2014) The role of Wnt/β-catenin signaling in proliferation and regeneration of the developing basilar papilla and lateral line. Developmental Neurobiology 74:438–456. https://doi.org/10.1002/dneu.22134

Janesick A, Scheibinger M, Benkafadar N, et al (2021) Cell-type identity of the avian cochlea. Cell Reports 34:. https://doi.org/10.1016/j.celrep.2021.108900

Ji YR, Warrier S, Jiang T, et al (2018) Directional selectivity of afferent neurons in zebrafish neuromasts is regulated by Emx2 in presynaptic hair cells. eLife 7:e35796. https://doi.org/10.7554/eLife.35796

Jiang L, Romero-Carvajal A, Haug JS, et al (2014) Gene-expression analysis of hair cell regeneration in the zebrafish lateral line. Proc Natl Acad Sci U S A 111:E1383–E1392. https://doi.org/10.1073/pnas.1402898111

Jiang L, Xu J, Jin R, et al (2018) Transcriptomic analysis of chicken cochleae after gentamicin damage and the involvement of four signaling pathways (Notch, FGF, Wnt and BMP) in

hair cell regeneration. Hearing Research 361:66–79. https://doi.org/10.1016/j.heares.2018.01.004

Jiang T, Kindt K, Wu DK (2017) Transcription factor Emx2 controls stereociliary bundle orientation of sensory hair cells. In: eLife. https://elifesciences.org/articles/23661. Accessed 20 Sep 2018

Jones JE, Corwin JT (1993) Replacement of lateral line sensory organs during tail regeneration in salamanders: identification of progenitor cells and analysis of leukocyte activity. J Neurosci 13:1022–1034

Jones JM, Montcouquiol M, Dabdoub A, et al (2006) Inhibitors of Differentiation and DNA Binding (Ids) Regulate Math1 and Hair Cell Formation during the Development of the Organ of Corti. J Neurosci 26:550–558. https://doi.org/10.1523/JNEUROSCI.3859-05.2006

Jørgensen JM, Mathiesen C (1988) The avian inner ear. Continuous production of hair cells in vestibular sensory organs, but not in the auditory papilla. Die Naturwissenschaften 75:319–320. https://doi.org/10.1007/BF00367330

Kamaid A, Neves J, Giráldez F (2010) Id Gene Regulation and Function in the Prosensory Domains of the Chicken Inner Ear: A Link between Bmp Signaling and Atoh1. J Neurosci 30:11426–11434. https://doi.org/10.1523/JNEUROSCI.2570-10.2010

Kastan N, Gnedeva K, Alisch T, et al (2021) Small-molecule inhibition of Lats kinases may promote Yap-dependent proliferation in postmitotic mammalian tissues. Nat Commun 12:3100. https://doi.org/10.1038/s41467-021-23395-3

Kelley MW (2003) Cell adhesion molecules during inner ear and hair cell development, including notch and its ligands. Curr Top Dev Biol 57:321–356. https://doi.org/10.1016/s0070-2153(03)57011-9

Kelley MW, Stone JS (2017) Development and Regeneration of Sensory Hair Cells. In: Cramer KS, Coffin AB, Fay RR, Popper AN (eds) Auditory Development and Plasticity: In Honor of Edwin W Rubel. Springer International Publishing, Cham, pp 17–48

Keren K, Pincus Z, Allen GM, et al (2008) Mechanism of shape determination in motile cells. Nature 453:475–480. https://doi.org/10.1038/nature06952

Kiernan AE, Cordes R, Kopan R, et al (2005) The Notch ligands DLL1 and JAG2 act synergistically to regulate hair cell development in the mammalian inner ear. Development 132:4353–4362. https://doi.org/10.1242/dev.02002

Kil J, Warchol ME, Corwin JT (1997) Cell death, cell proliferation, and estimates of hair cell life spans in the vestibular organs of chicks. Hearing Research 114:117–126. https://doi.org/10.1016/S0378-5955(97)00166-4

Kilian KA, Bugarija B, Lahn BT, Mrksich M (2010) Geometric cues for directing the differentiation of mesenchymal stem cells. PNAS 107:4872–4877. https://doi.org/10.1073/pnas.0903269107

Kimura Y, Hisano Y, Kawahara A, Higashijima S (2014) Efficient generation of knock-in transgenic zebrafish carrying reporter/driver genes by CRISPR/Cas9-mediated genome engineering. Scientific Reports 4:srep06545. https://doi.org/10.1038/srep06545

Kindt KS, Sheets L (2018) Transmission Disrupted: Modeling Auditory Synaptopathy in Zebrafish. Frontiers in Cell and Developmental Biology 6:114. https://doi.org/10.3389/fcell.2018.00114

Kozak EL, Palit S, Miranda-Rodríguez JR, et al (2020) Epithelial Planar Bipolarity Emerges from Notch-Mediated Asymmetric Inhibition of Emx2. Current Biology 30:1142-1151.e6. https://doi.org/10.1016/j.cub.2020.01.027

Ku Y-C, Renaud NA, Veile RA, et al (2014) The Transcriptome of Utricle Hair Cell Regeneration in the Avian Inner Ear. J Neurosci 34:3523–3535. https://doi.org/10.1523/JNEUROSCI.2606-13.2014

Lambert T, Liu H, Buckley G, et al (2023) pyapp-kit/magicgui: v0.7.2. https://doi.org/10.5281/zenodo.7700260

Lanford PJ, Presson JC, Popper AN (1996) Cell proliferation and hair cell addition in the ear of the goldfish, Carassius auratus. Hearing Research 100:1–9. https://doi.org/10.1016/0378-5955(96)00110-4

Ledent V (2002) Postembryonic development of the posterior lateral line in zebrafish. Development 129:597–604

Lee SG, Huang M, Obholzer ND, et al (2016) Myc and Fgf Are Required for Zebrafish Neuromast Hair Cell Regeneration. PLOS ONE 11:e0157768. https://doi.org/10.1371/journal.pone.0157768

Levine JH, Simonds EF, Bendall SC, et al (2015) Data-Driven Phenotypic Dissection of AML Reveals Progenitor-like Cells that Correlate with Prognosis. Cell 162:184–197. https://doi.org/10.1016/j.cell.2015.05.047

Lewis ER, Li CW (1973) Evidence concerning the morphogenesis of saccular receptors in the bullfrog (Rana catesbeiana). Journal of Morphology 139:351–361. https://doi.org/10.1002/jmor.1051390305

Lewis RM, Hume CR, Stone JS (2012) Atoh1 expression and function during auditory hair cell regeneration in post-hatch chickens. Hear Res 289:74–85. https://doi.org/10.1016/j.heares.2012.04.008

Lewis RM, Keller JJ, Wan L, Stone JS (2018) Bone morphogenetic protein 4 antagonizes hair cell regeneration in the avian auditory epithelium. Hearing Research 364:1–11. https://doi.org/10.1016/j.heares.2018.04.008

Li T, Bellen HJ, Groves AK (2018) Using Drosophila to study mechanisms of hereditary hearing loss. Disease Models & Mechanisms 11:. https://doi.org/10.1242/dmm.031492

Li T, Giagtzoglou N, Eberl DF, et al (2016) The E3 ligase Ubr3 regulates Usher syndrome and MYH9 disorder proteins in the auditory organs of Drosophila and mammals. eLife 5:e15258. https://doi.org/10.7554/eLife.15258

Liang J, Wang D, Renaud G, et al (2012) The stat3/socs3a Pathway Is a Key Regulator of Hair Cell Regeneration in Zebrafish stat3/socs3a Pathway: Regulator of Hair Cell Regeneration. J Neurosci 32:10662–10673. https://doi.org/10.1523/JNEUROSCI.5785-10.2012

Liu Z, Dearman JA, Cox BC, et al (2012) Age-Dependent In Vivo Conversion of Mouse Cochlear Pillar and Deiters' Cells to Immature Hair Cells by Atoh1 Ectopic Expression. J Neurosci 32:6600–6610. https://doi.org/10.1523/JNEUROSCI.0818-12.2012

López-Schier H, Hudspeth AJ (2004) Directional Cell Migration Establishes the Axes of Planar Polarity in the Posterior Lateral-Line Organ of the Zebrafish. Developmental Cell 7:401-412. https://doi.org/10.1016/j.devcel.2004.07.018

López-Schier H, Hudspeth AJ (2006) A two-step mechanism underlies the planar polarization of regenerating sensory hair cells. PNAS 103:18615–18620. https://doi.org/10.1073/pnas.0608536103

Lush ME, Diaz DC, Koenecke N, et al (2019) scRNA-Seq reveals distinct stem cell populations that drive hair cell regeneration after loss of Fgf and Notch signaling. eLife 8:e44431. https://doi.org/10.7554/eLife.44431

Ma EY, Raible DW (2009) Signaling Pathways Regulating Zebrafish Lateral Line Development. Current Biology 19:R381–R386. https://doi.org/10.1016/j.cub.2009.03.057

Ma EY, Rubel EW, Raible DW (2008) Notch Signaling Regulates the Extent of Hair Cell Regeneration in the Zebrafish Lateral Line. J Neurosci 28:2261–2273. https://doi.org/10.1523/JNEUROSCI.4372-07.2008

Mackenzie SM, Raible DW (2012) Proliferative Regeneration of Zebrafish Lateral Line Hair Cells after Different Ototoxic Insults. PLOS ONE 7:e47257. https://doi.org/10.1371/journal.pone.0047257

Mallarino R, Campàs O, Fritz JA, et al (2012) Closely related bird species demonstrate flexibility between beak morphology and underlying developmental programs. Proceedings of the National Academy of Sciences 109:16222–16227. https://doi.org/10.1073/pnas.1206205109

Marean GC, Burt JM, Beecher MD, Rubel EW (1993) Hair cell regeneration in the European starling (Sturnus vulgaris): Recovery of pure-tone detection thresholds. Hearing Research 71:125–136. https://doi.org/10.1016/0378-5955(93)90028-Y

Marklein RA, Lo Surdo JL, Bellayr IH, et al (2016) High Content Imaging of Early Morphological Signatures Predicts Long Term Mineralization Capacity of Human Mesenchymal Stem Cells upon Osteogenic Induction. Stem Cells 34:935–947. https://doi.org/10.1002/stem.2322

Matsui JI, Haque A, Huss D, et al (2003) Caspase Inhibitors Promote Vestibular Hair Cell Survival and Function after Aminoglycoside Treatment In Vivo. J Neurosci 23:6111–6122. https://doi.org/10.1523/JNEUROSCI.23-14-06111.2003

Matsui JI, Oesterle EC, Stone JS, Rubel EW (2000) Characterization of Damage and Regeneration in Cultured Avian Utricles. JARO 1:46–63. https://doi.org/10.1007/s101620010005

Matsunaga M, Kita T, Yamamoto R, et al (2020) Initiation of Supporting Cell Activation for Hair Cell Regeneration in the Avian Auditory Epithelium: An Explant Culture Model. Frontiers in Cellular Neuroscience 14:583994. https://doi.org/10.3389/fncel.2020.583994

McHenry MJ, Feitl KE, Strother JA, Trump WJV (2009) Larval zebrafish rapidly sense the water flow of a predator's strike. Biology Letters. https://doi.org/10.1098/rsbl.2009.0048

McInnes L, Healy J, Saul N, Großberger L (2018) UMAP: Uniform Manifold Approximation and Projection. JOSS 3:861. https://doi.org/10.21105/joss.00861

Mekdara PJ, Schwalbe MAB, Coughlin LL, Tytell ED (2018) The effects of lateral line ablation and regeneration in schooling giant danios. Journal of Experimental Biology 221:. https://doi.org/10.1242/jeb.175166

Metcalfe WK (1985) Sensory neuron growth cones comigrate with posterior lateral line primordial cells in zebrafish. Journal of Comparative Neurology 238:218–224. https://doi.org/10.1002/cne.902380208

Meyers JR, Corwin JT (2007) Shape Change Controls Supporting Cell Proliferation in Lesioned Mammalian Balance Epithelium. J Neurosci 27:4313–4325. https://doi.org/10.1523/JNEUROSCI.5023-06.2007

Millimaki BB, Sweet EM, Dhason MS, Riley BB (2007) Zebrafish atoh1 genes: classic proneural activity in the inner ear and regulation by Fgf and Notch. Development 134:295–305. https://doi.org/10.1242/dev.02734

Millimaki BB, Sweet EM, Riley BB (2010) Sox2 is required for maintenance and regeneration, but not initial development, of hair cells in the zebrafish inner ear. Developmental Biology 338:262–269. https://doi.org/10.1016/j.ydbio.2009.12.011

Monaghan JR, Maden M (2012) Visualization of retinoic acid signaling in transgenic axolotls during limb development and regeneration. Dev Biol 368:63–75. https://doi.org/10.1016/j.ydbio.2012.05.015

Montcouquiol M, Corwin JT (2001) Brief Treatments with Forskolin Enhance S-Phase Entry in Balance Epithelia from the Ears of Rats. J Neurosci 21:974–982. https://doi.org/10.1523/JNEUROSCI.21-03-00974.2001

Morishita Y, Hironaka K, Lee S-W, et al (2017) Reconstructing 3D deformation dynamics for curved epithelial sheet morphogenesis from positional data of sparsely-labeled cells. Nat Commun 8:15. https://doi.org/10.1038/s41467-017-00023-7

Nagiel A, Andor-Ardó D, Hudspeth AJ (2008) Specificity of Afferent Synapses onto Plane-Polarized Hair Cells in the Posterior Lateral Line of the Zebrafish. J Neurosci 28:8442–8453. https://doi.org/10.1523/JNEUROSCI.2425-08.2008

Namdaran P, Reinhart KE, Owens KN, et al (2012) Identification of Modulators of Hair Cell Regeneration in the Zebrafish Lateral Line. J Neurosci 32:3516–3528. https://doi.org/10.1523/JNEUROSCI.3905-11.2012

Neves J, Kamaid A, Alsina B, Giraldez F (2007) Differential expression of Sox2 and Sox3 in neuronal and sensory progenitors of the developing inner ear of the chick. Journal of Comparative Neurology 503:487–500. https://doi.org/10.1002/cne.21299

Niemiec AJ, Raphael Y, Moody DB (1994) Return of auditory function following structural regeneration after acoustic trauma: Behavioral measures from quail. Hearing Research 79:1–16. https://doi.org/10.1016/0378-5955(94)90122-8

Nuñez VA, Sarrazin AF, Cubedo N, et al (2009) Postembryonic development of the posterior lateral line in the zebrafish. Evolution & Development 11:391–404. https://doi.org/10.1111/j.1525-142X.2009.00346.x

Oesterle EC, Campbell S, Taylor RR, et al (2008) Sox2 and Jagged1 Expression in Normal and Drug-Damaged Adult Mouse Inner Ear. J Assoc Res Otolaryngol 9:65–89. https://doi.org/10.1007/s10162-007-0106-7

Oesterle EC, Rubel EW (1993) Postnatal production of supporting cells in the chick cochlea. Hearing Research 66:213–224. https://doi.org/10.1016/0378-5955(93)90141-M

Oesterle EC, Stone JS (2008) Hair Cell Regeneration: Mechanisms Guiding Cellular Proliferation and Differentiation. In: Salvi RJ, Popper AN, Fay RR (eds) Hair Cell Regeneration, Repair, and Protection. Springer, New York, NY, pp 141–197

Olsen AM (2017) Feeding ecology is the primary driver of beak shape diversification in waterfowl. Functional Ecology 31:1985–1995. https://doi.org/10.1111/1365-2435.12890

Pasha Hosseinbor A, Chung MK, Koay CG, et al (2015) 4D hyperspherical harmonic (HyperSPHARM) representation of surface anatomy: A holistic treatment of multiple disconnected anatomical structures. Medical Image Analysis 22:89–101. https://doi.org/10.1016/j.media.2015.02.004

Pedregosa F, Varoquaux G, Gramfort A, et al (2011) Scikit-learn: Machine Learning in Python. Journal of Machine Learning Research 12:2825–2830

Pei W, Huang SC, Xu L, et al (2016) Loss of Mgat5a-mediated N-glycosylation stimulates regeneration in zebrafish. Cell Regen 5:. https://doi.org/10.1186/s13619-016-0031-5

Pei W, Xu L, Huang SC, et al (2018) Guided genetic screen to identify genes essential in the regeneration of hair cells and other tissues. npj Regenerative Medicine 3:1–11. https://doi.org/10.1038/s41536-018-0050-7

Piccolo S, Dupont S, Cordenonsi M (2014) The Biology of YAP/TAZ: Hippo Signaling and Beyond. Physiological Reviews. https://doi.org/10.1152/physrev.00005.2014

Pincus Z, Theriot JA (2007) Comparison of quantitative methods for cell-shape analysis. Journal of Microscopy 227:140–156. https://doi.org/10.1111/j.1365-2818.2007.01799.x

Pinto-Teixeira F, Viader-Llargués O, Torres-Mejía E, et al (2015) Inexhaustible hair-cell regeneration in young and aged zebrafish. Biology Open 4:903–909. https://doi.org/10.1242/bio.012112

Pittlik S, Begemann G (2012) New sources of retinoic acid synthesis revealed by live imaging of an Aldh1a2-GFP reporter fusion protein throughout zebrafish development. Dev Dyn 241:1205–1216. https://doi.org/10.1002/dvdy.23805

Popper AN, Hoxter B (1984) Growth of a fish ear: 1. Quantitative analysis of hair cell and ganglion cell proliferation. Hearing Research 15:133–142. https://doi.org/10.1016/0378-5955(84)90044-3

Presson JC, Lanford PJ, Popper AN (1996) Hair cell precursors are ultrastructurally indistinguishable from mature support cells in the ear of a postembryonic fish. Hearing Research 100:10–20. https://doi.org/10.1016/0378-5955(96)00109-8

Rhinn M, Dollé P (2012) Retinoic acid signalling during development. Development 139:843–858. https://doi.org/10.1242/dev.065938

Roberson DF, Weisleder P, Bohrer PS, Rubel EW (1992) Ongoing production of sensory cells in the vestibular epithelium of the chick. Hearing Research 57:166–174. https://doi.org/10.1016/0378-5955(92)90149-H

Roberson DW, Krieg C, Rubel EW (2004) Light microscopic evidence that direct transdifferentiation gives rise to new hair cells in regenerating avian auditory epithelium. Aud Neurosci 2:195–205

Romero-Carvajal A, Navajas Acedo J, Jiang L, et al (2015) Regeneration of Sensory Hair Cells Requires Localized Interactions between the Notch and Wnt Pathways. Developmental Cell 34:267–282. https://doi.org/10.1016/j.devcel.2015.05.025

Ruan X, Murphy RF (2019) Evaluation of methods for generative modeling of cell and nuclear shape. Bioinformatics 35:2475–2485. https://doi.org/10.1093/bioinformatics/bty983

Rubbini D, Robert-Moreno À, Hoijman E, Alsina B (2015) Retinoic Acid Signaling Mediates Hair Cell Regeneration by Repressing p27kip and sox2 in Supporting Cells. J Neurosci 35:15752–15766. https://doi.org/10.1523/JNEUROSCI.1099-15.2015

Rubel EW, Furrer SA, Stone JS (2013) A Brief History of Hair Cell Regeneration Research and Speculations on the Future. Hear Res 297:42–51. https://doi.org/10.1016/j.heares.2012.12.014

Rudolf MA, Andreeva A, Kozlowski MM, et al (2020) YAP Mediates Hair Cell Regeneration in Balance Organs of Chickens, But LATS Kinases Suppress Its Activity in Mice. J Neurosci 40:3915–3932. https://doi.org/10.1523/JNEUROSCI.0306-20.2020

Ryals BM, Dent ML, Dooling RJ (2013) Return of Function after Hair Cell Regeneration. Hear Res 297:113–120. https://doi.org/10.1016/j.heares.2012.11.019

Ryals BM, Rubel EW (1988) Hair cell regeneration after acoustic trauma in adult Coturnix quail. Science 240:1774–1776. https://doi.org/10.1126/science.3381101

Scheibinger M, Ellwanger DC, Corrales CE, et al (2018) Aminoglycoside Damage and Hair Cell Regeneration in the Chicken Utricle. JARO 19:17–29. https://doi.org/10.1007/s10162-017-0646-4

Schindelin J, Arganda-Carreras I, Frise E, et al (2012) Fiji: an open-source platform for biological-image analysis. Nat Methods 9:676–682. https://doi.org/10.1038/nmeth.2019

Schuck JB, Smith ME (2009) Cell proliferation follows acoustically-induced hair cell bundle loss in the zebrafish saccule. Hearing Research 253:67–76. https://doi.org/10.1016/j.heares.2009.03.008

Schuck JB, Sun H, Penberthy WT, et al (2011) Transcriptomic analysis of the zebrafish inner ear points to growth hormone mediated regeneration following acoustic trauma. BMC Neuroscience 12:88. https://doi.org/10.1186/1471-2202-12-88

Segal D, Mazloom-Farsibaf H, Chang B-J, et al (2022) In vivo 3D profiling of site-specific human cancer cell morphotypes in zebrafish. Journal of Cell Biology 221:e202109100. https://doi.org/10.1083/jcb.202109100

Seleit A, Krämer I, Riebesehl BF, et al (2017) Neural stem cells induce the formation of their physical niche during organogenesis. eLife Sciences 6:e29173. https://doi.org/10.7554/eLife.29173

Shang J, Cafaro J, Nehmer R, Stone J (2010) Supporting Cell Division Is Not Required for Regeneration of Auditory Hair Cells After Ototoxic Injury In Vitro. JARO 11:203–222. https://doi.org/10.1007/s10162-009-0206-7

Shi T, Beaulieu MO, Saunders LM, et al (2023) Single-cell transcriptomic profiling of the zebrafish inner ear reveals molecularly distinct hair cell and supporting cell subtypes. eLife 12:e82978. https://doi.org/10.7554/eLife.82978

Slattery EL, Speck JD, Warchol ME (2009) Epigenetic Influences on Sensory Regeneration: Histone Deacetylases Regulate Supporting Cell Proliferation in the Avian Utricle. JARO 10:341–353. https://doi.org/10.1007/s10162-009-0166-y

Smith PJ, Wiltshire M, Davies S, et al (1999) A novel cell permeant and far red-fluorescing DNA probe, DRAQ5, for blood cell discrimination by flow cytometry. J Immunol Methods 229:131–139. https://doi.org/10.1016/s0022-1759(99)00116-7

Sofroniew N, Lambert T, Evans K, et al (2022) napari: a multi-dimensional image viewer for Python. https://doi.org/10.5281/ZENODO.7276432

Song J, Yan HY, Popper AN (1995) Damage and recovery of hair cells in fish canal (but not superficial) neuromasts after gentamicin exposure. Hearing Research 91:63–71. https://doi.org/10.1016/0378-5955(95)00170-0

Steiner AB, Kim T, Cabot V, Hudspeth AJ (2014) Dynamic gene expression by putative hair-cell progenitors during regeneration in the zebrafish lateral line. PNAS 111:E1393–E1401. https://doi.org/10.1073/pnas.1318692111

Stojanova ZP, Kwan T, Segil N (2016) Epigenetic regulation of Atoh1 guides hair cell development in the mammalian cochlea. Development 143:1632–1632. https://doi.org/10.1242/dev.137976

Stone JS, Cotanche DA (2007) Hair cell regeneration in the avian auditory epithelium. Int J Dev Biol 51:633–647. https://doi.org/10.1387/ijdb.072408js

Stone JS, Leaño SG, Baker LP, Rubel EW (1996) Hair Cell Differentiation in Chick Cochlear Epithelium after Aminoglycoside Toxicity: In Vivo and In VitroObservations. J Neurosci 16:6157–6174. https://doi.org/10.1523/JNEUROSCI.16-19-06157.1996

Stone JS, Rubel EW (1999) Delta1 expression during avian hair cell regeneration. Development 126:961–973

Stone JS, Rubel EW (2000) Temporal, spatial, and morphologic features of hair cell regeneration in the avian basilar papilla. Journal of Comparative Neurology 417:1–16. https://doi.org/10.1002/(SICI)1096-9861(20000131)417:1<1::AID-CNE1>3.0.CO;2-E

Stone LS (1937) Further experimental studies of the development of lateral-line sense organs in amphibians observed in living preparations. Journal of Comparative Neurology 68:83–115. https://doi.org/10.1002/cne.900680105

Sugawara K, Çevrim Ç, Averof M (2022) Tracking cell lineages in 3D by incremental deep learning. eLife 11:e69380. https://doi.org/10.7554/eLife.69380

Suli A, Pujol R, Cunningham DE, et al (2016) Innervation regulates synaptic ribbons in lateral line mechanosensory hair cells. J Cell Sci 129:2250–2260. https://doi.org/10.1242/jcs.182592

Suli A, Watson GM, Rubel EW, Raible DW (2012) Rheotaxis in Larval Zebrafish Is Mediated by Lateral Line Mechanosensory Hair Cells. PLOS ONE 7:e29727. https://doi.org/10.1371/journal.pone.0029727

Sun H, Lin C-H, Smith ME (2011) Growth Hormone Promotes Hair Cell Regeneration in the Zebrafish (Danio rerio) Inner Ear following Acoustic Trauma. PLOS ONE 6:e28372. https://doi.org/10.1371/journal.pone.0028372

Sun Z, Amourda C, Shagirov M, et al (2017) Basolateral protrusion and apical contraction cooperatively drive Drosophila germ-band extension. Nat Cell Biol 19:375–383. https://doi.org/10.1038/ncb3497

Thevenaz P, Ruttimann UE, Unser M (1998) A pyramid approach to subpixel registration based on intensity. IEEE Trans on Image Process 7:27–41. https://doi.org/10.1109/83.650848

Thomas ED, Raible DW (2019) Distinct progenitor populations mediate regeneration in the zebrafish lateral line. eLife 8:e43736. https://doi.org/10.7554/eLife.43736

Thompson D (1917) On Growth and Form. https://www.gutenberg.org/files/55264/55264-h/55264-h.htm. Accessed 19 Apr 2023

Traag VA, Waltman L, van Eck NJ (2019) From Louvain to Leiden: guaranteeing well-connected communities. Sci Rep 9:5233. https://doi.org/10.1038/s41598-019-41695-z

van der Walt S, Schönberger JL, Nunez-Iglesias J, et al (2014) scikit-image: image processing in Python. PeerJ 2:e453. https://doi.org/10.7717/peerj.453

Viader-Llargués O, Lupperger V, Pola-Morell L, et al (2018) Live cell-lineage tracing and machine learning reveal patterns of organ regeneration. eLife Sciences 7:e30823. https://doi.org/10.7554/eLife.30823

Viana MP, Chen J, Knijnenburg TA, et al (2023) Integrated intracellular organization and its variations in human iPS cells. Nature 613:345–354. https://doi.org/10.1038/s41586-022-05563-7

Virshup I, Rybakov S, Theis FJ, et al (2021) anndata: Annotated data. BioRxiv (Preprint). https://doi.org/10.1101/2021.12.16.473007

Wada H, Ghysen A, Satou C, et al (2010) Dermal morphogenesis controls lateral line patterning during postembryonic development of teleost fish. Developmental Biology 340:583–594. https://doi.org/10.1016/j.ydbio.2010.02.017

Wakasaki T, Niiro H, Jabbarzadeh-Tabrizi S, et al (2017) Musashi-1 is the candidate of the regulator of hair cell progenitors during inner ear regeneration. BMC Neuroscience 18:64. https://doi.org/10.1186/s12868-017-0382-z

Wan G, Corfas G, Stone JS (2013) Inner ear supporting cells: Rethinking the silent majority. Seminars in Cell & Developmental Biology 24:448–459. https://doi.org/10.1016/j.semcdb.2013.03.009

Wan L, Lovett M, Warchol ME, Stone JS (2020) Vascular endothelial growth factor is required for regeneration of auditory hair cells in the avian inner ear. Hearing Research 385:107839. https://doi.org/10.1016/j.heares.2019.107839

Wang RN, Green J, Wang Z, et al (2014) Bone Morphogenetic Protein (BMP) signaling in development and human diseases. Genes & Diseases 1:87–105. https://doi.org/10.1016/j.gendis.2014.07.005

Warchol ME (2011) Sensory regeneration in the vertebrate inner ear: Differences at the levels of cells and species. Hearing Research 273:72–79. https://doi.org/10.1016/j.heares.2010.05.004

Warchol ME, Schrader A, Sheets L (2021) Macrophages Respond Rapidly to Ototoxic Injury of Lateral Line Hair Cells but Are Not Required for Hair Cell Regeneration. Frontiers in Cellular Neuroscience 14:613246. https://doi.org/10.3389/fncel.2020.613246

Warchol ME, Schwendener RA, Hirose K (2012) Depletion of Resident Macrophages Does Not Alter Sensory Regeneration in the Avian Cochlea. PLOS ONE 7:e51574. https://doi.org/10.1371/journal.pone.0051574

Warchol ME, Stone J, Barton M, et al (2017) ADAM10 and γ-secretase regulate sensory regeneration in the avian vestibular organs. Developmental Biology 428:39–51. https://doi.org/10.1016/j.ydbio.2017.05.014

Watt FM, Jordan PW, O'Neill CH (1988) Cell shape controls terminal differentiation of human epidermal keratinocytes. PNAS 85:5576–5580. https://doi.org/10.1073/pnas.85.15.5576

Weigert M, Schmidt U, Boothe T, et al (2018) Content-aware image restoration: pushing the limits of fluorescence microscopy. Nat Methods 15:1090–1097. https://doi.org/10.1038/s41592-018-0216-7

White PM, Stone JS, Groves AK, Segil N (2012) EGFR signaling is required for regenerative proliferation in the cochlea: Conservation in birds and mammals. Developmental Biology 363:191–200. https://doi.org/10.1016/j.ydbio.2011.12.035

Wibowo I, Pinto-Teixeira F, Satou C, et al (2011) Compartmentalized Notch signaling sustains epithelial mirror symmetry. Development 138:1143–1152. https://doi.org/10.1242/dev.060566

Williams JA, Holder N (2000) Cell turnover in neuromasts of zebrafish larvae. Hearing Research 143:171–181. https://doi.org/10.1016/S0378-5955(00)00039-3

Witte MC, Montcouquiol M, Corwin JT (2001) Regeneration in avian hair cell epithelia: identification of intracellular signals required for S-phase entry. European Journal of Neuroscience 14:829–838. https://doi.org/10.1046/j.0953-816x.2001.01695.x

Wolf FA, Angerer P, Theis FJ (2018) SCANPY: large-scale single-cell gene expression data analysis. Genome Biology 19:15. https://doi.org/10.1186/s13059-017-1382-0

Wolf FA, Hamey FK, Plass M, et al (2019) PAGA: graph abstraction reconciles clustering with trajectory inference through a topology preserving map of single cells. Genome Biol 20:59. https://doi.org/10.1186/s13059-019-1663-x

Woolley SMN, Rubel EW (2002) Vocal Memory and Learning in Adult Bengalese Finches with Regenerated Hair Cells. J Neurosci 22:7774–7787. https://doi.org/10.1523/JNEUROSCI.22-17-07774.2002

Woolley SMN, Wissman AM, Rubel EW (2001) Hair cell regeneration and recovery of auditory thresholds following aminoglycoside ototoxicity in Bengalese finches. Hearing Research 153:181–195. https://doi.org/10.1016/S0378-5955(00)00217-3

Ye Z, Su Z, Xie S, et al (2020) Yap-lin28a axis targets let7-Wnt pathway to restore progenitors for initiating regeneration. eLife 9:e55771. https://doi.org/10.7554/eLife.55771

Yin Z, Sadok A, Sailem H, et al (2013) A screen for morphological complexity identifies regulators of switch-like transitions between discrete cell shapes. Nat Cell Biol 15:860–871. https://doi.org/10.1038/ncb2764

Yizhar-Barnea O, Valensisi C, Jayavelu ND, et al (2018) DNA methylation dynamics during embryonic development and postnatal maturation of the mouse auditory sensory epithelium. Scientific Reports 8:17348. https://doi.org/10.1038/s41598-018-35587-x

Zheng JL, Shou J, Guillemot F, et al (2000) Hes1 is a negative regulator of inner ear hair cell differentiation. Development 127:4551–4560